University of California
Los Angeles

Quasi-static Modeling of Beam-Plasma and Laser-Plasma Interactions

A dissertation submitted in partial satisfaction
of the requirements for the degree
Doctor of Philosophy in Electrical Engineering

by

Chengkun Huang

2005

The dissertation of Chengkun Huang is approved.

Steven Cowley

Tatsuo Itoh

Chandrashekhar J. Joshi

Warren B. Mori, Committee Chair

University of California, Los Angeles

2005

To my parents and friends . . .
who—among so many other things—
gave me courage and hope to overcome
the difficulties in my life.

Table of Contents

1 Introduction 1

1.1 Electron-positron collider 1

1.2 The International Linear Collider(ILC) 3

1.3 Plasma Wakefield Accelerator 6

1.4 Blow-out regime 11

1.5 Afterburner concept 19

1.6 Experiments 23

1.7 Computer simulations 27

2 Particle-In-Cell simulation 32

2.1 Particle-In-Cell simulation 32

2.2 Fully explicit PIC model 34

2.3 Reduced description PIC models 43

2.3.1 Darwin model 43

2.3.2 Quasi-static PIC model 46

2.3.3 Numerical Instability 64

2.4 Summary 66

3 Implementation of QuickPIC 67

3.1 Algorithm 67

3.1.1 Moving window 68

3.1.2 Plasma and beam update 69

3.1.3 Charge and current depositions 73
3.1.4 Iteration and Diffusion damping 74
3.1.5 Boundary conditions 80
3.1.6 Initialization and Quiet start 82
3.1.7 Laser module 85
3.2 PIC framework 94
3.3 Parallelization 96
3.4 Performance 102
3.5 Summary 104

4 Benchmarking QuickPIC 106
4.1 Benchmark for an electron beam driver 106
4.2 Benchmark for a positron beam driver 111
4.3 Benchmark for a laser driver 116

5 Hosing instability 119
5.1 Hosing Instability 119
5.2 Hosing theory and verification 129
5.2.1 Hosing theory based on particle model 129
5.2.2 Verification of the model 136
5.3 Summary 147

6 Simulation of Afterburner 148
6.1 Choosing parameters 148

6.2 Simulation results 151

6.3 Summary 161

7 Summary 163

A Conserved Quantity of Particle Motion 166

B An Analytical Model For ψ 168

References 170

List of Figures

1.1 History of the universe. The abbreviations shown at the bottom of figure are existing machines or machines under construction or planned for the future. LHC: Large Hadron Collider at CERN; LC: International Linear Collider; RHIC: Relativistic Heavy Ion Collider at BNL; HERA: a proton-electron collider at DESY. . . . 5

1.2 A cartoon showing the beam and the blow-out trajectories on top of the density of the plasma electron. 12

1.3 The three regions of the plasma response to a ultra-relativistic electron beam in the blow-out regime. The yellow or green color in the color map represents high density and red region is the ion channel where election density is 0. The drive beam in white color is superimposed on this picture to show the relative positions of the three regions. $\xi = ct - z$ is the longitudinal position relative to the beam. 17

1.4 The profile of the source term $(\rho - J_z/c)$ used by Lu et al.. In this plot, the width of the electron sheath is denoted by Δ_e; the width of the linear response region is Δ_L. The rectangular profile used in the theoretical model has a width of $\Delta = \Delta_e + \Delta_L$ and a height of $n_\Delta = \frac{r_b^2}{(r_b+\Delta)^2 - r_b^2}$. 18

1.5 A conceptual 100GeV-on-100GeV electron-positron collider based on a plasma afterburner. 21

2.1 Schematic of a uniform mesh($\Delta x = \Delta y$) used in 2D PIC simulation. Particles are shown as red dots. Grid points are shown as blue diamonds. 37

2.2 Illustration of the area weighting coefficient used for the charge and current deposition schemes in PIC codes. 38

2.3 Schematic of a calculation cycle in PIC codes. 41

2.4 Schematic of the coordinate system used in QuickPIC. 49

2.5 The drive beam and the plasma response. Electromagnetic fields are frozen between successive beam updates. 51

2.6 Physical picture of how the plasma evolves. It also shows the relation between Δs and $\Delta \xi$. 52

2.7 Particle's trajectory in 1D can be plotted as z(t) or t(z). 53

2.8 Trajectories of plasma and beam particles in (s,ξ,x) space. 54

3.1 A moving window with velocity c is used to follow beam's evolution. 69

3.2 Flow chart of the QuickPIC quasi-static algorithm showing a 2D routine embedded in a 3D routine. 71

3.3 A transverse lineout of ψ in the full and basic QuickPIC simulations for the same parameters used in Chapter 4. 83

3.4 Schematic representation of second order accurate split step algorithm for advancing the laser field in s. Also shown is the communication between the laser propagation part of the code and the particle and wake part of the code. 91

3.5 The drive beam can be viewed as a series of slices of width $\Delta \xi$ distributed on different nodes. 97

3.6 The plasma is distributed in y. The communications happen between any two nodes. 98

3.7 Timing of the 2D loop on two different platforms, i.e, NERSC with high speed network and DAWSON with gigabit ethernet. 100

3.8 The relation between the overhead and the number of CPUs in the timing benchmarks on DAWSON cluster. 101

4.1 Longitudinal wakefields in QuickPIC and OSIRIS simulations for an electron drive beam. Both 2 iterations(l=2) and 4 iterations(l=4) are used for the QuickPIC simulations. The driver moves from right to left in this plot. 108

4.2 Radial electric field comparison for electron drive beam. 109

4.3 Azimuthal magnetic field comparison for electron drive beam. . . 110

4.4 The plasma electron charge density (ρ_p/ρ_{ion}) in the $x-z$ plane at the center of the beam is shown for a) an OSIRIS simulation and b) a QuickPIC simulation. In both cases, the driver moves from top to bottom. 112

4.5 Comparison of the longitudinal wakefield for a positron driver. . . 113

4.6 Radial electric field in the positron benchmark simulation. 114

4.7 Azimuthal magnetic field in the positron benchmark simulation. . 115

4.8 Longitudinal electric field comparison for a laser driver. 118

5.1 A plot of the shape of the beam and the ion channel in the nominal "afterburner" simulation. 121

5.2 The absolute value of the centroid position $|x_b|$ in a self-generated channel (blue curve) and the prediction from a linear theory for a equilibrium channel (red curve). The black line is a linear fit for the initial growth in the simulation before the nonlinearity occurs. This initial growth is orders of magnitude smaller than the result for a equilibrium channel. The hosing amplitude begins to saturate for $s > 0.6m$. 124

5.3 A diagram of the linear fluid analysis for hosing instability. a) the tilted beam in a equilibrium channel. b) the cross-sections of the beam and the ion channel which are shifted by an amount of x_b and x_c respectively. 125

5.4 A cartoon for the trajectory perturbation model used in the hosing analysis. $\pm r_0$ are the unperturbed trajectories of the innermost electrons and r_+, $-r_-$ are their perturbed trajectories respectively. 130

5.5 Density plot of the beams (left) and plasma (right) in the simulation for the hosing instability in the adiabatic non-relativistic blow-out regime. The beams move downward in this plot. 138

5.6 Hosing growth of the centroid oscillation as a function of propagation distance s from the simulation and the theory prediction for the adiabatic non-relativistic blow-out regime. 139

5.7 Density plot of the beams (left) and plasma (right) in the simulation for the hosing instability in the adiabatic relativistic blow-out regime. 140

5.8 Hosing growth of the centroid oscillation as a function of propagation distance s from the simulation and the theory prediction for the adiabatic relativistic blow-out regime. 141

5.9 Density plot of the beams (left) and plasma (right) in the simulation for the hosing instability in the non-adiabatic non-relativistic blow-out regime. 143

5.10 Hosing growth of the centroid oscillation as a function of propagation distance s from the simulation and the theory prediction for the non-adiabatic non-relativistic blow-out regime. 144

5.11 Density plot of the beams (left) and plasma (right) in the simulation for the hosing instability in the non-adiabatic relativistic blow-out regime. 145

5.12 Hosing growth of the centroid oscillation as a function of propagation distance s from the simulation and the theory prediction for the non-adiabatic relativistic blow-out regime. 146

6.1 The beam and plasma evolution at different propagation distances from the 100GeV stage simulation. The beams move from right to left. 153

6.2 Longitudinal wakefield evolution in the 100 GeV simulation. . . . 154

6.3 Phase space plot at the end of the 100 GeV stage simulation. . . . 155

6.4 Energy distribution of the drive beam and the trailing beam in a 100 GeV afterburner simulation. 156

6.5 The beam and the plasma channel at different propagation distances in the 1 TeV simulation. 157

6.6 Longitudinal wakefield evolution in the 1 TeV stage simulation. . 158

6.7 Phase space of the beams at different distances in the 1 TeV stage afterburner simulation. 159

6.8 Energy distribution of the trailing beam in the 1TeV simulation. . 160

List of Tables

1.1 E157/E162 parameters 25

1.2 Codes currently used in plasma-based accelerator research and their features. 29

3.1 Quantities and their roles in the 2D cycle and the corresponding 2D time step at which they are defined. 77

5.1 Nominal parameters for the hosing simulation. 122

6.1 Simulation parameters 150

6.2 Numerical simulation parameters 151

Acknowledgments

The work of this dissertation would not be possible without the help from Prof. Warren Mori, Dr. Viktor Decyk, Dr. Chuang Ren and Dr. Shuoqin Wang. They introduced this research topic and clarified the concepts and answered various other questions for me. I am also grateful to Dr. Frank Tsung, Wei Lu and Miaomiao Zhou for the consistent help they provided. Section 3.1.7 of Chapter 3 includes the work from our collaboration, Prof. Thomas Antonsen and Dr. James Cooley of University of Maryland. Their contributions to the development of QuickPIC are greatly appreciated. The Discussions with Prof. Tom Katsouleas, Dr. Patric Muggli, Prof. Chan. Joshi and Dr. Chris Clayton have also been useful and important to this dissertation.

Vita

1975	Born, Guangzhou, GuangDong Province, P.R. China
1994–1998	B.S. (Engineering Physics), Tsinghua University, Beijing, P.R. China
1998–2000	M.S. (Nuclear Science and Engineering), Tsinghua University, Beijing, P.R. China
2000–2003	M.S. (Electrical Engineering), University of California, Los Angeles, California, U.S.A.
2003–present	Ph.D. candidate, Department of Electrical Engineering, University of California, Los Angeles, California, U.S.A.

Publications

Chengkun Huang, V. K. Decyk, C. Ren, M. Zhou, W. Lu, W. B. Mori, J. H. Cooley, T. M. Antonsen Jr., T. Katsouleas, QUICKPIC: A highly efficient particle-in-cell code for modeling wakefield acceleration in plasmas, submitted to Journal of Computational Physics.

C. Huang, C. Clayton, D. Johnson, C. Joshi, W. Lu, W. Mori, M. Zhou, C. Barnes, F.-J. Decker, M. Hogan, R. Iverson, S. Deng, T. Katsouleas, P. Muggli, E. Oz, Modeling TeV Class Plasma Afterburners, Proceedings of the Particle Accelerator Conference, 2005. (in press)

W. Lu, C. Huang, M. M. Zhou, W. B. Mori, and T. Katsouleas, Limits of linear plasma wakefield theory for electron or positron beams, Phys. Plasmas 12, 063101 (2005)

P. Muggli, B. E. Blue, C. E. Clayton, S. Deng, F.-J. Decker, M. J. Hogan, C. Huang, R. Iverson, C. Joshi, T. C. Katsouleas, S. Lee, W. Lu, K. A. Marsh, W. B. Mori, C. L. O'Connell, P. Raimondi, R. Siemann, and D. Walz, Meter-Scale Plasma-Wakefield Accelerator Driven by a Matched Electron Beam, Phys. Rev. Lett. 93, 014802 (2004)

C. Huang, W. Lu, M. M. Zhou, V. K. Decyk, W. B. Mori, E. Oz, C. D. Barnes, C. E. Clayton, F. J. Decker, S. Deng, M. J. Hogan, R. Iverson, D. K. Johnson, C. Joshi, T. Katsouleas, P. Krejcik, K. A. Marsh, P. Muggli, C. O'Connell, and D. Walz, Simulation of a 50GeV PWFA Stage, AIP Conf. Proc. 737, 433 (2004)

B. E. Blue, C. E. Clayton, C. L. O'Connell, F.-J. Decker, M. J. Hogan, C. Huang, R. Iverson, C. Joshi, T. C. Katsouleas, W. Lu, K. A. Marsh, W. B. Mori, P. Muggli, R. Siemann, and D. Walz, Plasma-Wakefield Acceleration of an Intense Positron Beam, Phys. Rev. Lett. 90, 214801 (2003)

E. S. Dodd, R. G. Hemker, C.-K. Huang, S. Wang, C. Ren, W. B. Mori, S. Lee, and T. Katsouleas, Hosing and Sloshing of Short-Pulse GeV-Class Wakefield Drivers, Phys. Rev. Lett. 88, 125001 (2002)

C. Joshi, B. Blue, C. E. Clayton, E. Dodd, C. Huang, K. A. Marsh, W. B. Mori, S. Wang, M. J. Hogan, C. O'Connell, R. Siemann, D. Watz, P. Muggli, T. Kat-

souleas, and S. Lee, High energy density plasma science with an ultrarelativistic electron beam, Phys. Plasmas 9, 1845 (2002)

C. Huang, V. Decyk, S. Wang, E. Dodd, C. Ren, W. Mori, T. Katsouleas, J. Cooley, T. Antonsen, A parallel Particle-In-Cell code for efficiently modeling plasma wakefield acceleration: QuickPIC, Proceedings of ACES 2002, Monterey, CA, March 2002

Chengkun Huang, V. Decyk, Shuoqin Wang, E.S. Dodd, Chuang Ren, W.B. Mori, T. Katsouleas, T. Antonsen Jr., QuickPIC: a parallelized quasi-static PIC code for modeling plasma wakefield acceleration, Proceedings of the Particle Accelerator Conference, 2001. Volume 5

Abstract of the Dissertation

Quasi-static Modeling of Beam-Plasma and Laser-Plasma Interactions

by

Chengkun Huang

Doctor of Philosophy in Electrical Engineering

University of California, Los Angeles, 2005

Professor Warren B. Mori, Chair

Plasma wave wakefields excited by either laser or particle beams can sustain acceleration gradients three orders of magnitude larger than conventional RF accelerators. They are promising for accelerating particles in short distances for applications such as future high-energy colliders, and medical and industrial accelerators. In a Plasma Wakefield Accelerator (PWFA) or a Laser Wakefield Accelerator (LWFA), an intense particle or laser beam drives a plasma wave and generates a strong wakefield which has a phase velocity equal to the velocity of the driver. This wakefield can then be used to accelerate part of the drive beam or a separate trailing beam. The interaction between the plasma and the driver is highly nonlinear and therefore a particle description is required for computer modeling. A highly efficient, fully parallelized, fully relativistic, three-dimensional particle-in-cell code called QuickPIC for simulating plasma and laser wakefield acceleration has been developed. The model is based on the quasi-static or frozen field approximation, which assumes that the drive beam and/or the laser does not evolve during the time it takes for it to pass a plasma particle. The electromagnetic fields of the plasma wake and its associated index of refraction are

then used to evolve the driver using very large time steps. This algorithm reduces the computational time by at least 2 to 3 orders of magnitude. Comparison between the new algorithm and a fully explicit model (OSIRIS) are presented. The agreement is excellent for problems of interest. Direction for future work is also discussed. QuickPIC has been used to study the "afterburner" concept. In this concept a fraction of an existing high-energy beam is separated out and used as a trailing beam with the goal that the trailing beam acquires at least twice the energy of the drive beam. Several critical issues such as the efficient transfer of energy and the stable propagation of both the drive and trailing beams in the plasma are investigated. We have simulated a 100 GeV and a 1 TeV plasma "afterburner" stages for electron beams and the results are presented. QuickPIC also has enabled us to develop a new theory for understanding the hosing instability of the drive and trailing beams. The new theory is based on a perturbation to the ion column boundary which includes relativistic effects, axial motion and the full electromagnetic character of the wake. The new theory is verified by comparing it to the simulation results. In the adiabatic long beam limit it recovers the result of previous work from fluid models.

CHAPTER 1

Introduction

1.1 Electron-positron collider

Particle accelerators are devices in which electric fields are used to accelerate charged particles. They are widely used in basic scientific research, high energy physics, industry, medical diagnosis and treatment, new material research and many other areas. High energy accelerators are also important tools for studying elementary particles and understanding the interactions between them. The energy of particles in high energy linear accelerators has gone up 9 orders of magnitudes to 50GeV since the first electro-static accelerator was invented, however the basic principle of an accelerator has not changed.

Early accelerators used electrodes which are connected to a voltage multiplier or a Van de Graaff Generator, particles are accelerated in the static electric field between two opposite sign electrodes. As the velocity of the charged particle increased, difficulties arose as how to keep particles in the accelerating fields.

The linear accelerator(Linac) introduced the concept of using an oscillating electromagnetic wave which travels at the speed of the particles to keep charged particles in phase with the accelerating gradient. A room-sized linac can accelerate electrons or positrons to energies on the order of 100MeV. To achieve even higher energy one has to extend the linac to greater lengths which increases the difficulty to build and operate such a machine; and hence drives up the cost.

The Stanford Linear Collider is the longest linac which has been built to date. At 2 miles long, SLC can generate 50 GeV electrons and positrons. At the end of the linac, the accelerated beams are transported to the interaction point and focused down to sub-micron sizes for head-to-head collisions. Very high energy electron-positron collisions with center-of-mass energy of 100GeV have been achieved in this collider, where Z bosons are produced and studied from these collisions.

Another type of high energy particle accelerator is the synchrotron accelerator in which magnetic fields are used to turn the particles so that they move in circular orbits. Charged particles are accelerated in each turn around the machine. An example of this type of collider is the Large Electron Positron collider (LEP) at CERN. It has a storage ring of 17 miles in circumference. For synchrotrons, the maximum energy is limited by the loss to synchrotron radiation which is proportional to $(E/m)^4/R$, where E is the energy, m is the mass of the particle and R is the radius of the orbit. Since the loss of energy in this type of accelerator is inversely proportional to R, they are made as large as possible. LEP is capable of producing 50GeV electrons/positrons for collisions. To extrapolate to a 500GeV collider, one has to increase the size of LEP by 1000 times to keep the energy loss ratio (the ratio between energy loss and initial energy) the same. This is a prohibitive size for practical reasons, not to mention the cost.

Both SLC and LEP use RF microwaves as the driving source for particle acceleration. Such RF systems are the major energy-consuming part of a high energy accelerator. A significant step toward a more affordable high energy accelerator is to use superconducting technology to reduce the energy consumption of the RF system during operation. TESLA (TeV-Energy Superconducting Linear Accelerator) is a new linear accelerator design with superconducting niobium resonators

at DESY. This has also been an international collaboration. The TESLA design includes a 33 km long superconducting linac from end to end which accelerates particles to 250 GeV. The center-of-mass energy will be 500GeV for the collider. A TESLA test facility with a 100-meter-long linac was constructed and it has recently been extended to a length of 260 meters for use in a vacuum ultraviolet (VUV) and soft X-ray range free electron laser(FEL). The design acceleration gradient is 25MV/m in the superconducting cavities at a temperature of 2K. In addition, 35MV/m gradient has been demonstrated in the test facility, thus the proposed TESLA design could be upgradeable to around 800 GeV in the future.

However, the superconducting niobium cavity can only operate in electric fields below 50 MV/m, which is lower than the limit for a conventional cavity. This is determined by the properties of niobium, because at high electric fields, the heat generated in a superconducting cavity would cause the material to lose superconductivity. A superconducting collider thus requires a longer linac for the same energy, which correspondingly requires larger engineering cost. On the other hand, although conventional copper accelerating structure can sustain fields of 70 MV/m, studies have shown that material deterioration in such high fields is much faster than expected. For these reasons, neither conventional nor superconducting technology offers a cost-effective way to build and operate the next generation high energy collider.

1.2 The International Linear Collider(ILC)

The International Linear Collider(ILC) [1] is the current vision of the world-wide accelerator community for the next generation linear collider. It has been recognized by particle physicists that finding the Higgs boson and measuring its properties accurately would be a significant scientific advance for understanding

the interactions between elementary particles and for unraveling fundamental questions such as dark matter, dark energy and the neutrino mass. Fig. 1.1 shows the time scales of the evolution of the universe and the energy associated with the interactions on each time scale [2].

It has been estimated that if Higgs bosons exist, their characteristic rest-mass will be between 117 GeV to 251 GeV [3]. Although this energy range is covered by the CERN LHC which is a proton-proton collider set to operate in 2007. The measurement of the spin and parity of the Higgs boson; the determination of the masses and quantum numbers of the supersymmetric particles and the measurement of the number of extra dimensions requires a electron-positron collider in the TeV range [4]. A TeV electron-positron collider provides advantages such as well-defined initial states of collision energy, quantum numbers and polarization, a point particle like collision interaction and a precise understanding of cross-section. It will be a useful complementary machine to the LHC for this purpose and also has the ability for studying other unique problems.

As envisioned, the ILC will operate in the center-of-masses energy range from 0.5 to 1.0 TeV. Until recently, there were two competing designs for the ILC. The first one, so called the "cold" design, was based on TELSA technology which uses 1.3 GHz (L-band) superconducting cavities; the second one, called the "warm" design, was based on the 11.4 GHz (X-band) room temperature copper structures developed at SLAC and KEK. Both technologies are mature enough for consideration in such a large scale application. However, it is a consensus of the accelerator community that only one accelerator will be built even with international collaborations due to its huge cost and technological complexities. In 2004, the International Committee for Future Accelerators (ICFA) chose the superconducting technology for the ILC after extensive investigation of issues such

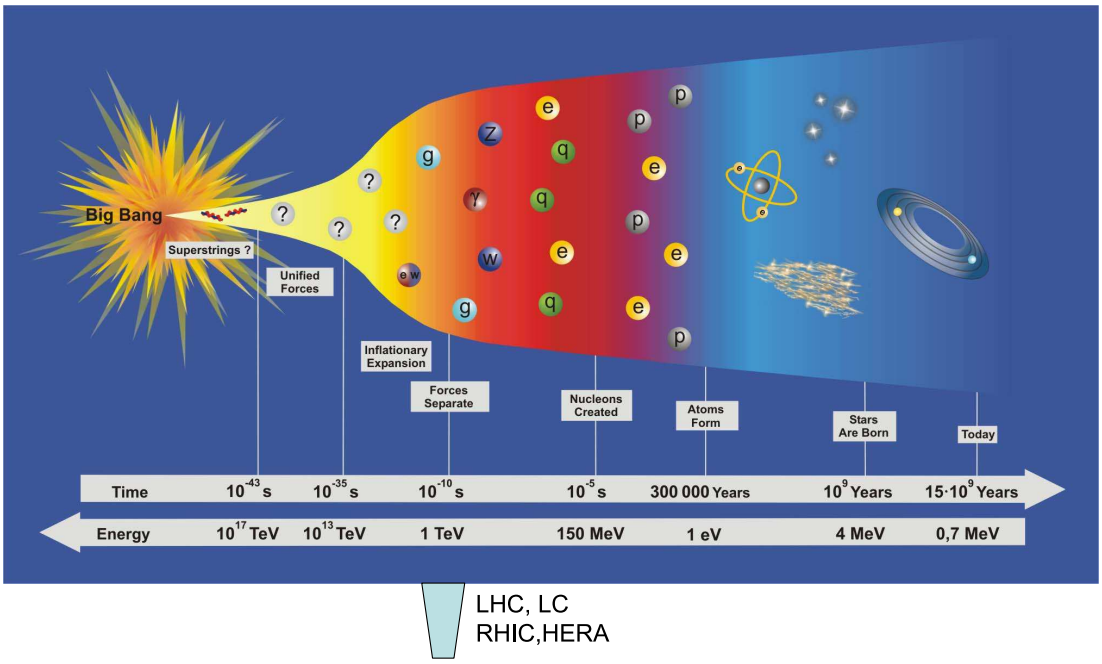

Figure 1.1: History of the universe. The abbreviations shown at the bottom of figure are existing machines or machines under construction or planned for the future. LHC: Large Hadron Collider at CERN; LC: International Linear Collider; RHIC: Relativistic Heavy Ion Collider at BNL; HERA: a proton-electron collider at DESY.

as cost and schedule as well as technical and physics operation issues. Despite the compelling physics reasons for the ILC and the consensus of the accelerator physics community that the "cold" design should be used, it is still not clear that the world wide governments are ready to move forward because of the enormous price tag of $\sim$ ten billion dollars.

1.3 Plasma Wakefield Accelerator

In conventional or superconducting accelerators, the electric fields are supported by the metallic cavities. The breakdown limit of the surrounding material of the accelerating structure is the major constraint for using stronger electric fields in such devices. Other concerns such as field-emission of electrons from the cavity wall and pulsed heating to the structure are also important limiting factors for increasing the acceleration gradient. For example, the average acceleration gradient at the Stanford Linear Accelerator Center(SLAC) is currently 20MeV/m. The "warm" design of ILC could have achieved around 70MV/m while the "cold" design has a upper limit of $\sim$ 50MV/m because the superconductivity of niobium can not survive in such environment.

The concepts of plasma-based accelerators, first developed by Tajima and Dawson in 1979 [5], have attracted tremendous interest. It is well-known that a plasma is already ionized so there is no breakdown limit. This makes plasma a suitable medium for the acceleration structure. In a uniform plasma, electric fields can be excited by disturbing the plasma density. This is easily realized by using a charged particle beam or a laser beam. A charged particle beam expels or attracts plasma particles by the Coloumb force(usually the velocity of a plasma particle is small thus one can neglect the magnetic force, however, the full Lorentz force has to be taken into consideration in the non-linear regime

discussed in the following chapters); a laser beam can also push plasma particles away through the ponderomotive force. Therefore a plasma oscillation can be set up in a plasma whenever a laser or particle beam passes through it. The plasma oscillations and the associated field structures follow the drive beam and this picture resembles the wakefield of a motor boat. The phase velocity of the wave, v_p, is the same as the velocity of the drive beam and the wavelength is determined by the phase velocity and the plasma frequency, $\lambda_p = 2\pi v_p/\omega_p$. It is possible to use the longitudinal electric field generated in the plasma waves to accelerate electron or positron beams just as using the fields in the metallic waveguide of a linac. In the linear fluid regime, the amplitude of the plasma wave as well as the longitudinal electric field increases with the strength of the drive beam. For a particle beam case, this is determined by the peak beam density and for a laser beam this is determined by the normalized ponderomotive potential. When the driver strength is increased, eventually the trajectories of individual plasma particles cross each other. The simple fluid analysis breaks down and the longitudinal field reaches a limit. The so-called "wave-breaking" limit is the the peak accelerating field a plasma can sustain in the fluid analysis, it is given by $E_{max} \sim \sqrt{n_0(cm^{-3})}V/cm$ [5], where n_0 is the plasma density. Therefore a $10^{14}cm^{-3}$ plasma can support an electric field of $\sim 1GV/m$, which is about two orders of magnitude higher than those of conventional acceleration structures. This estimate of the accelerating gradient shows that plasma has great potential as an accelerating structure. Using a linac made of a plasma wakefield structure could dramatically reduce the size of a TeV class electron-positron collider to 100-1000 meters.

As discussed, there are several schemes to excite a plasma wave in a wakefield accelerator. Ref [5] proposed using a high power short laser pulse or the beat-wave of two laser pulses with frequency difference $\Delta\omega \approx \omega_p$, where ω_p is the

plasma frequency, to resonantly drive a plasma wakefield. The first method is often referred to as Laser Wakefield Accelerator(LWFA) and the second one is referred to as Plasma Beat-wave Accelerator(PBWA) [6]. A third method in which a long laser pulse undergoes the forward Raman instability and decays into a plasma wave and a forward propagating light wave [7, 8, 9, 10] is called the Self-Modulated Laser Wakefield Accelerator (SMLWFA).

A fourth scheme which is commonly referred to as the Plasma Wakefield Accelerator (PWFA) is the main topic of this dissertation. Since the first suggestion to use a particle beam as driver in ref. [11] by Chen, this scheme has been under extensive and systematic investigations and there has been tremendous progress. To understand the research in this dissertation, it is necessary to review this progress. In this section, we shall focus on the progress in theory. Advances in experiment and simulation are covered in sections 1.6 and 1.7. This review is not meant to be complete due to the rich physical phenomena involved, rather it is meant as a means to introduce basic concepts and to motivate the research described in the following chapters. Due to the different nature of electron beam-plasma and positron beam-plasma interactions, we also confined the review to the electron driver case. The positron beam-plasma interaction in the PWFA scenario still requires significant advances in theory and experiments. In chapter 3, a computer model for PWFA and the implementation of it which is called QuickPIC are described. Using QuickPIC, complex and fully non-linear positron beam-plasma interaction can be successfully modeled.

The progress in PWFA research was first enabled by theoretical understanding of the beam-plasma interaction in this scheme. In [11] the linear fluid theory for PWFA was developed, and it was found that an accelerating gradient exceeding 1GeV/m is possible. The energy loss of the drive beam of a beam train and

the energy gain of the trailing beam were analyzed using the linearized fluid description of the plasma. Under this linear fluid framework, Katsouleas in ref. [12] further developed the concept of an "ideal" door-step beam shape in 1D geometry first proposed by Chen and discussed the wakefield of a "non-ideal" shape beam by solving the Green's function of the plasma fluid response to a delta function charge. The result was applied to a Gaussian-shape beam with sharp cut-off and it was found that the transformer ratio R, which is the ratio of maximum energy gain of accelerated particles to the maximum energy loss of the decelerated particles, is between $\sqrt{\pi/2}k_p\sigma_{rise}$ and $\sqrt{2\pi}k_p\sigma_{rise}$ where σ_{rise} is the rise width of the beam, i.e., the density of the beam $n_b = n_{b0}e^{-z^2/2\sigma_{rise}^2}$ for $z > 0$. The transformer ratio is enhanced with this beam shape above the maximum transformer ratio of 2 for a symmetric beam shape. The two-stream instability and dephasing between the wake and the trapped particles were found not to be issues for a highly-relativistic PWFA.

Beam-loading is the physics of efficiently transferring energy from a drive beam to a trailing beam. This was first addressed in [13]. A linear superposition approach based on the wakefields from the driver and trailing beam was used in [13]. This is reasonable for small perturbations when the fluid theory remains valid. It was realized that efficient beam-loading requires a tradeoff between the efficiency or equivalently the total number of accelerated particles versus the accelerating gradient. The energy spread of the accelerated particles was found to be improved with a reverse triangle shape beam. Within the validity of the linear fluid theory, transverse beam-loading issues were also studied in [13] for cases where the trailing beam had a width much less than a collisionless skin depth. Recently, a clarification of the expression for the linear wakefield of a narrow beam with a Gaussian profile in both the longitudinal and transverse directions was carried out by Lu et al. [14]. By narrow, we mean $k_p\sigma_r << 1$

and an aspect ratio $\sigma_r/\sigma_z << 1$, where σ_z and σ_r are the RMS dimensions in longitudinal and transverse directions respectively. It turns out that this is the situation of most interest for recent experiments. The maximum axial electric field is found to be,

$$E_{zM} \approx (236MV/m)(\frac{q}{e})(\frac{N}{4\times 10^{10}})(\frac{0.06cm}{\sigma_z})^2 \ln(\sqrt{\frac{10^{16}cm^{-3}}{n_0}}\frac{50\mu m}{\sigma_r}) \qquad (1.1)$$

where q is the particle charge (+e for a positron or proton beam and -e for electron beam), N is the total number of electrons in the beam, σ_r is in unit of μm and σ_z is in unit of cm, n_0 is the plasma density in cm^{-3}. It should be pointed out that in Eq. (1.1), n_0 is not a free parameter, it is an "optimal" density determined by $k_p\sigma_z \approx \sqrt{2}$.

It is illustrative to understand the scaling of the wakefield for various beam parameters. Suppose the charge, N, is kept constant, then one can manipulate the spot-sizes of the beam by focusing or compression techniques. We shall tune the plasma density to satisfy the "optimal" density condition $k_p\sigma_z \approx \sqrt{2}$ so that the maximum wakefield in Eq. (1.1) is always achieved for given beam parameters. Under such assumptions, Eq. (1.1) indicates the $1/\sigma_z^2$ scaling of the wakefield amplitude on the bunch length provided that the logarithmic term does not change. This is only true when the aspect ratio σ_r/σ_z is kept fixed, so the logarithmic term is also constant. However, due to the slowly varying nature of a logarithmic function, the $1/\sigma_z^2$ scaling is still a useful guide for choosing experimental parameters. The $1/\sigma_z^2$ scaling implies that if one could compress the bunch length by a factor of 10, the maximum wakefield could increase by a factor of 100. This estimate motivated some recent wakefield experiments for shorter bunches [15, 16].

1.4 Blow-out regime

The initial theoretical and experimental works of the PWFA concept mainly focused on the linear regime in which the peak beam density n_b is much smaller than the plasma density n_0. In this regime, the transformer ratio is less than or equal to 2 for symmetric beams, the transverse wakefield is non-uniform and varies with both the radius and the longitudinal position inside the beam. These have negative effects on the quality of the accelerated beam. In 1987, Rosenzweig [17] proposed the non-linear regime of PWFA operation as an alternative. He obtained the analytical solutions of one dimensional relativistic fluid equations and showed that large longitudinal electric fields approaching the wave-breaking limit can be generated when the beam density larger than or equal to one-half of the plasma density. This idea was later extended to the two or three dimensional case [18] by the same author with even higher beam density. The major difference between the 1D and 2D situations is such that plasma electrons' transverse motion is now dominant, while in the 1D case they can only move longitudinally. Rosenzweig considered a case where $n_b/n_0 = 4$. The plasma is called "underdense" in this example, the fields from the beam are no longer a small perturbation to the plasma so linear fluid theory breaks down [14]. Plasma electrons are rapidly expelled in the radial direction by the beam's electric field, while the ions are heavier and they do not move during the time it takes for the beam to pass by. This process will continue until all the electrons are expelled from the beam and a pure ion channel is formed, see Fig. 1.2. For this reason, this proposed extremely non-linear regime is often referred to as the "blow-out" regime.

There are several advantages to the blow-out regime. Inside the channel, the ion density is uniform, thus providing a linear focusing field for the beam particles. Therefore inside the channel, particles with the same energy will oscillate

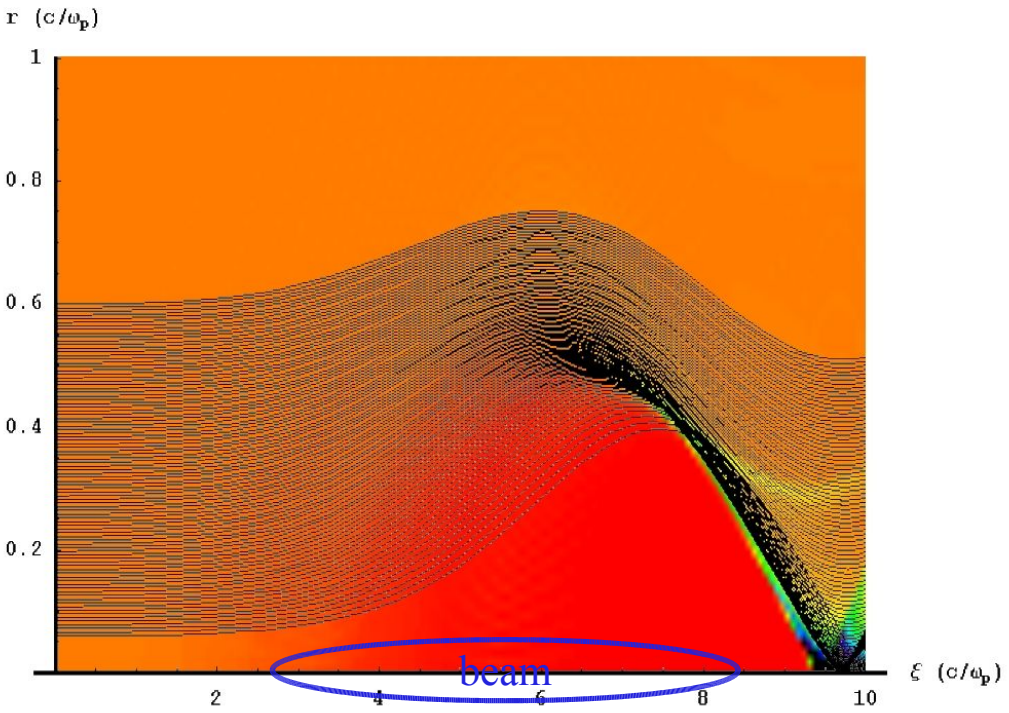

Figure 1.2: A cartoon showing the beam and the blow-out trajectories on top of the density of the plasma electron.

transversely at the same frequency, thereby preserving emittance. Furthermore, the Panofsky-Wenzel theorem [19] indicates another excellent consequence which is that the longitudinal wakefield is constant in the transverse direction. Therefore, there will be no energy spread for the accelerated particles at different radial positions but at the same longitudinal position.

It was further pointed out in [14] that the linear expressions for the wakefields give useful estimates even when the fluid analysis breaks down for the non-linear regime $n_b/n_0 > 1$. It was found that in the narrow beam limit of the blow-out regime, the non-linear beam-plasma interaction is characterized by the normalized charge per unit length of the beam,

$$\Lambda \equiv \frac{n_b}{n_p} k_p^2 \sigma_r^2. \tag{1.2}$$

For beams with moderate charge and spot-sizes, i.e., $\Lambda < 1$ and $(\Lambda/10)^{1/2} < k_p\sigma_r < 1$, fluid theory captures the essential dynamics of the blow-out by assuming electrons' trajectories do not cross even when n_b/n_0 approaches or is larger than unity. If n_b/n_0 is further increased while keeping Λ fixed by reducing the normalized spot-size $k_p\sigma_r$, eventually electrons' trajectories will cross and the fluid theory breaks down. This can be seen clearly from Eq. (1.1) by the divergence of the logarithmic term as $k_p\sigma_r$ approaches 0. Such an unphysical result will not happen in reality because the trajectory crossing occurs at the head of the beam which makes fluid analysis invalid. The wakefield indeed saturates for sufficiently small spot-size. Ref. [14] provides an empirical estimate of the saturation amplitude of the wakefield. In normalized unit, this is written as,

$$\epsilon \equiv eE/mc\omega_p = 1.3\Lambda ln[(10/\Lambda)^{1/2}] \tag{1.3}$$

Lu et al. showed in Ref. [14] that this estimate agrees with particle-in-cell simulations for $\Lambda < 1$. Thus, one can use Eq. (1.3) as a useful guide for the mildly non-linear blow-out regime. For the extremely non-linear regime, $\Lambda > 1$, the plasma electrons become highly relativistic which causes the wavelength to increase and the full electromagnetic character of the wake fields are important. Using Eq. (1.3) will overestimate the wakefield by a large amount. For such a situation, a particle description is more adequate than the fluid description.

The extraordinary properties of the blow-out regime have attracted lots of interest since it was proposed [20, 21, 22, 23, 24, 25, 26, 27]. Different issues such as wakefield amplitudes and structures, energy gain and loss of the electron beam, transverse dynamics in this regime were discussed in these papers. Other applications of the blow-out regime, such as the plasma lens [28] and the ion channel laser(ICL) [29] can also lead to novel plasma devices.

However, to understand the physics involved in the blow-out regime, one still needs a complete and self-consistent theory. Lotov described in Ref. [30] a theory based on particle's motion for an "infinitely long" beam. An analysis using fluid theory for the similar situation was done by Whittum [31]. An "infinitely long" beam implies that the ion channel is adiabatically formed. The radial velocity of the plasma electrons $v_r \approx 0$ and the plasma electrons' motion at the blow-out boundary is only in the longitudinal direction. Therefore only the beam's and plasma's charge densities and their longitudinal currents are taken into account in the field equations. Under this adiabatic blow-out assumption, it is found that the most descriptive parameter is n_b/n_0. This can be easily understood because the blow-out radius of plasma electrons for this case is simply determined by the equilibrium between an electron beam and an electron return current sheath due to their charge and parallel current densities. This equilibrium is local for each

longitudinal position, i.e., the local blow-out radius is determined by the local density ratio n_b/n_0 because the underlying differential equation [30] only involved transverse derivatives.

$$\frac{1}{\gamma^2 r}\frac{\partial}{\partial r}r\frac{\partial}{\partial r}\gamma v_z - \frac{v_z}{c^2}\frac{\partial v_z}{\partial r}\frac{\gamma\partial v_z}{\partial r} - \frac{4\pi e^2}{mc^2}v_z(n_i - n_b) = \frac{4\pi e^2}{mc^2}n_b \tag{1.4}$$

In Eq. (1.4), v_z is the longitudinal velocity of the plasma electron, r is the radial position, $\gamma = 1/\sqrt{1 - v_z^2/c^2}$ is the Lorentz factor, $n_i = n_0$ is the ion density, m is electron mass, c is speed of light.

The results from Lotov's theory and Whittum's fluid analysis are essentially the same because the adiabatic blow-out is basically an equilibrium problem which can be modeled using fluid theory.

In a recent paper [32], Lotov removed the above restriction on adiabatic blow-out and studied the dependence of blow-out properties on the beam length and current. Three qualitatively different regimes of the plasma response were found through particle-in-cell simulations. The first one is the regime described above. The second one is the so-called "strong beam" regime in which the blow-out radius is very large ($> 4c/\omega_p$), similar physics also appears in the "bubble" or "broken-wave" regime [33, 34] of LWFA. The third one is the "short beam" regime in which the beam resembles a point charge, this is also studied in Ref. [35] theoretically for the energy loss of the beam and in Ref. [36] by simulations. However, the theoretical analysis in [32] for the "strong beam" regime has flaws. The approximations for the narrow electron sheath layer used in deriving the blow-out radius is somewhat unjustified and the results are unphysical.

Recently, a fully nonlinear kinetic theory has been developed by Lu et al. [37]. In this theory, three interaction regions in the radial coordinate for the blow-out regime are identified. They are:

1) an ion channel region, where electrons are completely removed;

2) a narrow electron sheath region, where the electrons originally in the channel are densely packed into a thin layer, this region carries a large amount of charge and current densities. Strong electric and magnetic fields are generated by the sheath and the fields from the beam are strongly shielded;

3) a linear response region which extends from the sheath to a few plasma skin depth outwards. The fields penetrate into this region due to the incomplete shielding from the sheath. However the leakage fields are small and the plasma responds linearly to these fields, the interaction in this region can mostly be understood by linear fluid theory.

An illustration of these three regions is shown in Fig. 1.3 on top of the picture of the plasma electron density from a particle simulation.

Lu et al. pointed out that the exact forms of the charge and current profiles of the electron sheath and the linear response region have only a weak effect on the wake. One can assume the profiles are flat in each region and use rectangular shapes to model the rapid rise and fall, see Fig. 1.4.

Starting from the quasi-static Maxwell equations in the Lorentz gauge and the equation of motion for a plasma electron(more detail about the quasi-static approximation can be found in chapter 2), it is shown in [37] that the blow-out trajectory r_b of an electron satisfies a second order ordinary differential equation of the form,

$$A\frac{d^2 r_b}{d\xi^2} + Br_b(\frac{dr_b}{d\xi})^2 + Cr_b = \frac{\lambda(\xi)}{r_b} \tag{1.5}$$

where $\xi = ct - z$ is the longitudinal position relative to the beam, A, B and C are weakly dependent functions of Δ/r_b, and the source term $\lambda(\xi) = \int_0^{r>>\sigma_r} rn_b dr$

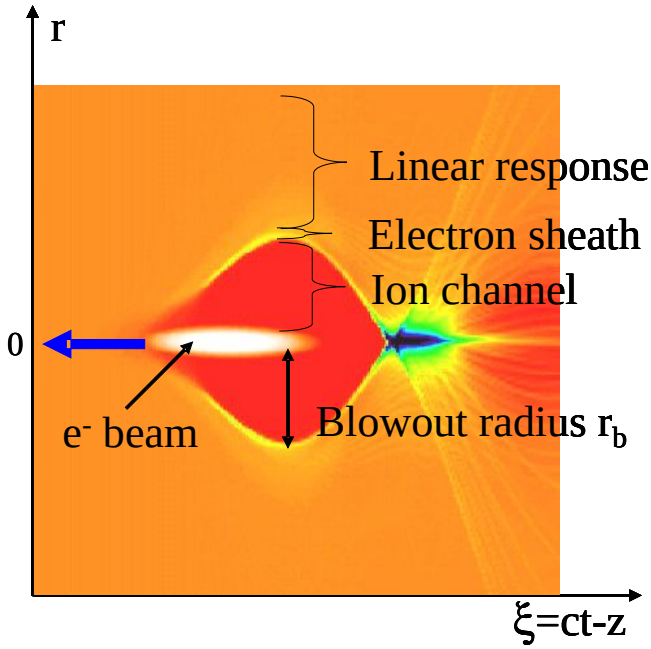

Figure 1.3: The three regions of the plasma response to a ultra-relativistic electron beam in the blow-out regime. The yellow or green color in the color map represents high density and red region is the ion channel where election density is 0. The drive beam in white color is superimposed on this picture to show the relative positions of the three regions. $\xi = ct - z$ is the longitudinal position relative to the beam.

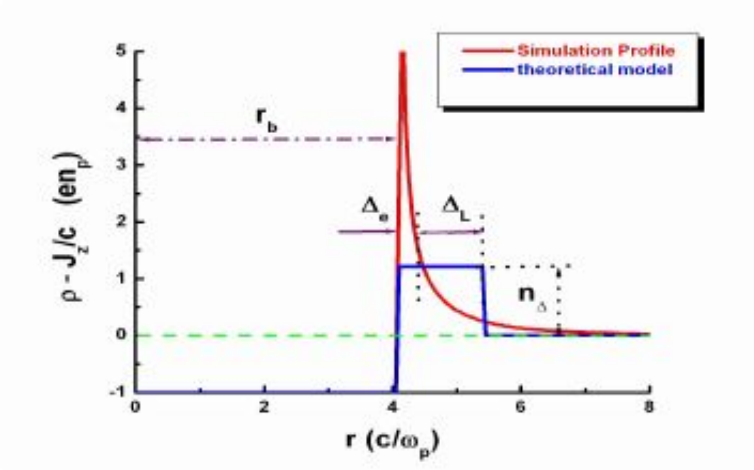

Figure 1.4: The profile of the source term $(\rho - J_z/c)$ used by Lu et al.. In this plot, the width of the electron sheath is denoted by Δ_e; the width of the linear response region is Δ_L. The rectangular profile used in the theoretical model has a width of $\Delta = \Delta_e + \Delta_L$ and a height of $n_\Delta = \frac{r_b^2}{(r_b+\Delta)^2 - r_b^2}$.

is the charge per unit length of the beam. In certain limits, i.e., specific beam parameters, one can approximate A, B and C with constants and solve for the blow-out trajectory numerically.

For the adiabatic blow-out limit which is the case studied in [30] and [31], $r_m \equiv MAX(r_b) << \sigma_z$, $\frac{dr_b}{d\xi} \sim 0$ and $\frac{d^2r_b}{d\xi^2} \sim 0$. Under these assumptions, one can obtain,

$$r_b(\xi) = \sqrt{2(1 - v_z)\lambda(\xi)} \tag{1.6}$$

For the non-relativistic blow-out regime ($r_m << 1$), Eq. (1.5) reduces to

$$\frac{d^2r_b}{d\xi^2} + \frac{1}{2}r_b = \frac{c(\xi)}{r_b} \tag{1.7}$$

For the ultra-relativistic blow-out regime ($r_m >> 1$), Eq. (1.5) reduces to

$$r_b\frac{d^2r_b}{d\xi^2} + 2(\frac{dr_b}{d\xi})^2 + 1 = \frac{4c(\xi)}{r_b^2} \tag{1.8}$$

Using Eq. (1.5) or Eqs. (1.6)- (1.7), it is therefore possible to calculate the shape of the ion-channel and hence the electric fields inside the channel as described in Appendix B. It is shown in Ref. [37] that the above equations give very accurate results for both the blow-out trajectories and electric fields when compared with the full PIC simulations except for the region at the tail of the channel.

1.5 Afterburner concept

It has been demonstrated that an accelerating structure with gradients on the order of GeV/m is possible based on the blow-out regime of PWFA. Several

years ago a typical beam used in SLAC had $N \approx 2 \times 10^{10}$ electrons with the dimensions of $\sigma_r \approx 25\mu m$ and $\sigma_z \approx 630\mu m$. In these experiments [38, 39] the plasma density was in the range of $10^{14} cm^{-3}$ and wakefields in the GeV/m range were demonstrated.

To make an even more compact PWFA, it is necessary to increase the acceleration gradient. There are several ways to increase the acceleration gradient. One could increase the beam charge or increase the plasma density or compress the beam. The $1/\sigma_z^2$ scaling of the wakefield amplitude indicates that it is very efficient to make a larger wakefield by compressing the longitudinal dimension of the beam.

Therefore if one could compress the SLAC beam by a factor of 10, the resulting wakefield would be in the range of tens of GeV/m. It would then be possible to double the energy of a 50GeV SLAC beam in just a few meters using the blow-out regime of PWFA. This energy doubling concept is called a plasma "afterburner" and a 200GeV center-of-mass collider based on such a design is illustrated in Fig. 1.5.

In Ref. [40], an afterburner is defined as "a specifically designed plasma that accelerates as well as focuses each beam from a linear collider in a single, short, final stage". There are two major functionalities of an afterburner. They are to accelerate electron/positron beams and to focus them down to the size for collision. These are both accomplished in plasmas. Shown in Fig. 1.5 is the proposed afterburner staged at the end of the SLAC linac. The 50GeV electron and positron beams from the linac are sent into two aligned plasma sections, one for electron acceleration, the other for positron acceleration. An electron beam drives a non-linear plasma wave and the trailing beam which rides the wave is boosted to 100GeV in about 10 meters, the drive beam loses energy to the plasma

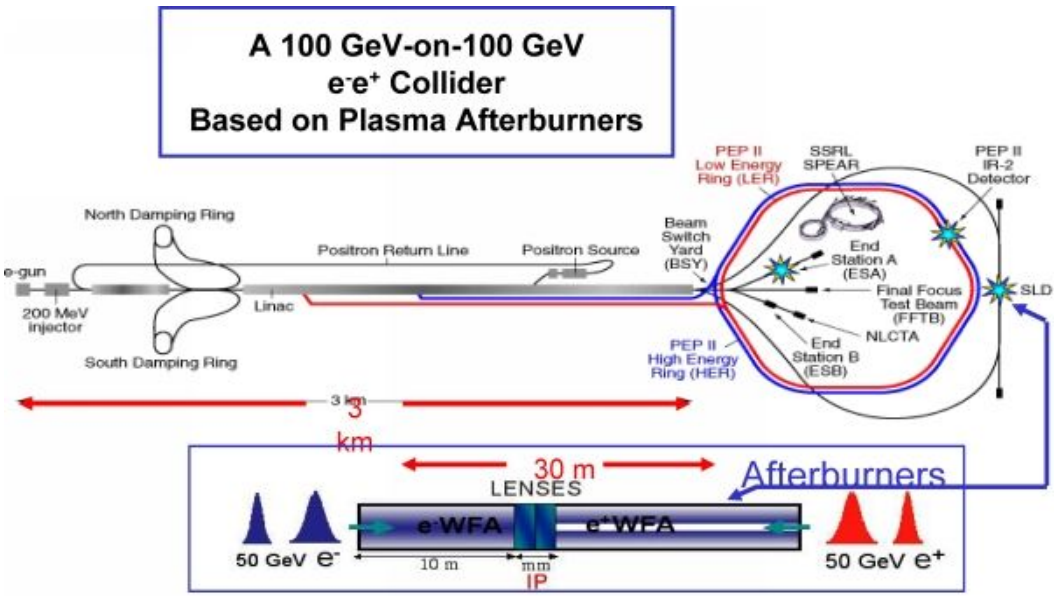

Figure 1.5: A conceptual 100GeV-on-100GeV electron-positron collider based on a plasma afterburner.

wave and almost stops in the plasma. Accelerating positron beams would require a longer acceleration distance due to the smaller wakefield excited by the positron beam [41]. At the exit of the plasma sections, two thin plasma lens will focus the electron and positron beams and let them collide at the interaction point.

Beam loading and transverse beam dynamics are of importance for an afterburner. So far, the beam loading problem in the blow-out regime has not been studied thoroughly. To get an energy-doubled trailing beam with good quality, such as small energy spread and emittance, it is necessary to probe the parameter space for optimal beam shapes, beam charge ratio and spacing between the drive beam and the trailing beam. The blow-out theory [37] would provide useful guidance in selecting the right parameters in term of the initial wake. However, the drive beam and the trailing beam both evolve during the propagation, so the beam loading condition has to be modified by taking the beam evolution into account. Such a study will only be possible by using full scale computer simulations for an afterburner. We will present such a study in chapter 6.

The transverse beam dynamics was initially studied by Buchanan in the blow-out regime [42] and by Whittum [43] in the context of ion channel laser. The ultra-relativistic electron beam propagating in the underdense plasma exhibits a transverse instability due to the coupling of the beam centroid to plasma electrons at the edge of the "ion-channel". This is a collective instability with similar character to the transverse two stream instability in the overdense plasma [22]. It is referred to as the "electron-hose" or hosing instability in [43]. The spatial temporal growth of the hosing instability was studied analytically and numerically for the adiabatic blow-out regime in [43, 44]. It was found to be a severe instability with fast growth that could destroy the drive or trailing beam in an afterburner. However, this analysis was carried out in the adiabatic blow-out regime or the

so called "preformed channel" case. Dodd et al. [24] showed through simulation that in the case where the ion channel is created by the beam itself, the hosing growth rate is significantly reduced. Since understanding the hosing instability will be critical for an afterburner, a self-consistent study of the hosing instability will be discussed in chapter 5. The initial hosing growth rate of the beam in the self-consistent fields is solved numerically and verified by fully non-linear PIC simulations.

1.6 Experiments

The progress of PWFA in the past 20 years has been tremendous. This is largely due to advances in technology on generating, manipulating, monitoring and diagnosing high current particle beams. In 1988, Rosenzweig et al. performed the first experiment to test the PWFA mechanism [45]. In this experiment, a $2.4mm$ long and $2.4mm$ wide drive beam with $2 \sim 3nC$ charge was used to excite a plasma wake. The plasma density was $10^{13}cm^{-3}$ so $n_b/n_0 \approx 0.0086$, which indicated that the experiment was in the linear fluid regime. A trailing electron beam of similar size but with low charge was used to sample the wakefield of the drive beam. An adjustable delay of the trailing (witness) beam with respect to the drive beam was used to map out the wakefield left behind the drive beam. The observed maximum energy gain was around 50 KeV for a plasma length of $L = 20 \sim 35cm$. The energy gain and the measured wavelength are in good agreement with the linear wakefield theory.

Soon after that, the first experiment of PWFA was repeated [46, 47] with higher beam density and lower plasma density so small nonlinearities began to show up, although for these experimental conditions most of the physics involved was still governed by the linear fluid theory.

Around the same period, experiments conducted by other groups worldwide [48, 49, 50] had reported acceleration gradients on the order of 10 MeV/m. These experiments further validated the linear fluid theory while some new techniques such as electron bunch trains were implemented.

Recently, the PWFA experiments entered the blow-out regime where the beam density is equal to or higher than the plasma density and $k_p\sigma_r < 1$. Ref. [51] reported a PWFA experiment with $n_b \sim 2.5n_p$ at the ANL wakefield facility. This experiment again used a drive and a witness beam, the average acceleration gradients were increased to 25 MeV/m over 12 cm of $10^{13}cm^{-3}$ plasma. The wave breaking field is 60MeV/m for this density.

All the experiments mentioned above used low-energy electron beams, which are subject to erosion and distortion during the non-linear beam-plasma interaction. Beam erosion is an effect which is associated with the finite response time of the plasma. The head of the beam expels plasma electrons but it takes time on the order of $1/\omega_p$ for the electrons to fly out and an ion channel to form. Hence the head of the beam will not experience the complete linear focusing force as the rest of the beam would. It will expand as it would in vacuum. The head erosion will make the wake generation less efficient and the whole beam will be eroded eventually if the propagation distance is long enough. Beam distortion is triggered by the instability such as hosing which results from the beam plasma interaction.

Both beam erosion and distortion are more pronounced for a high-charge low energy beam than a high energy beam. The magnetic force nearly cancels the space charge force for a beam moving at the speed of light, so a high energy beam can keep its shape when there is no additional focusing force. In recent years, important experiments in the blow-out regime were carried out us-

ing ultra-relativistic beams from SLAC linac. These experiments were done by a collaboration between SLAC, UCLA and USC, and they are called E157 [38] (LBNL participated in E157 experiment), E162 [52], E164 and E164X [15, 16].

These experiments were conducted at the Final Focus Test Beam (FFTB) facility located at the end of the 2-mile-long SLAC linac. The typical beam and plasma parameters used in the E157 and E162 experiments are summarized in Table 1.1,

Parameters	Values
Number of electrons(positrons)	$N = 1.8 \sim 2 \times 10^{10}$
Beam energy	$E = 28.5GeV$
Longitudinal spot size	$\sigma_z = 650\mu m$
Transverse spot size	$\sigma_r = 50 - 100\mu m$
Normalized emittance	$\epsilon_x = 50mm \cdot mrad$
	$\epsilon_y = 5mm \cdot mrad$
Peak beam density	$n_b \sim 10^{15} cm^{-3}$
Plasma density	$n_0 < 2 \times 10^{14} cm^{-3}$
Plasma length	$L = 1.4m$

Table 1.1: E157/E162 parameters

In the E157/E162 experiments, the beam density was about $1-10$ times higher than the plasma density and $k_p\sigma_r << 1$, thus ensuring that the interaction is in the blow-out regime. No trailing beam was used but the bunch length was on the order of the plasma skin depth c/ω_p, which is $1/2\pi$ of the non-relativistic wavelength of the plasma wave. The length of the ion channel was also on the order of c/ω_p, so the tail of the beam sampled the accelerating part of the wakefield. The energy of the beam was analyzed in a spectrometer but in regards to the

electron energy gain the results were not definitive. However, there was evidence that the core of the beam lost 170MeV and the tail gained about 350MeV.

The transverse dynamics of the ultra-relativistic beam was diagnosed by monitoring the spot size and displacement of the beam at the exit and at a distance downstream of the plasma. These diagnostics agreed well with the envelope model of the beam in a linear focusing field [53], thus confirming that the core of the beam was indeed immersed in the ion channel formed by the beam itself. A beam electron will execute betatron motion under the linear focusing force and it will radiate in the forward direction. Such phenomenon is well known as discussed in [53, 54], and it was proposed as a plasma wiggler for free-electron lasers [29, 55]. The wiggler strength, which is defined as $K = \gamma_b \omega_\beta r_0 / c$ (γ_b is the Lorentz factor of the beam, $\omega_\beta = \omega_p / \sqrt{2\gamma_b}$ is the betatron frequency and r_0 is the initial radial position of the electron) is much larger than 1, thus beam electrons radiate a broadband high harmonic spectrum. The characteristic frequency of the radiation is in the X-ray range and the angular divergence is extremely narrow for an ultra-relativistic beam. The E157/E162 team successfully measured the betatron radiation [56], which shows that a simple and inexpensive PWFA device could be used as a high brightness X-ray light source.

In another series of experiments, positron beams were used to study the plasma wake excitation in the underdense regime. Under the linear theory, there is no qualitative difference in wakefield generation between a positron beam and an electron beam. But when the beam density is approaching or larger than the plasma density, positron wakefield generation is very different from electron wakefield generation and the amplitude is much smaller than the electron wakefield for the same n_b/n_0. In the E157/E162 experiments, plasma wakefields excited by a positron beam was studied for the first time. It was observed that the core of

the beam lost $68 \pm 8MeV$ and the tail gained $79 \pm 15MeV$ [52] which is in good agreement with fully explicit PIC simulations.

Based on the experiences learned from the initial experiments and new compression techniques for the beam at SLAC, a new set of experiments, E164/E164X, were recently accomplished to test the $1/\sigma_z^2$ scaling of the electron wakefields. The Sub Picosecond Pulse Source (SPPS) at SLAC was used to generate electron beams as short as $20\mu m$. The $1/\sigma_z^2$ scaling would predict wakefields on the order of $100GeV$ for this type of short beam. It was also realized that the transverse self-electric fields of such short beams are large enough to field ionize the gas [26], thus there is no need to use a pre-ionizing laser pulse to generate the plasma. The self-ionization scheme would remove the complexity of synchronizing an ionizing laser pulse and the electron beam thereby providing a simpler design for the future experiments. In [15], it was reported that the E164/E164X experiments achieved energy loss and gain in the 2-4 GeV range in a 10 cm long plasma. The accelerating gradient was about 20-40GeV/m which is a tremendous improvement over the previous experiments in which the gradients were all less than 1GeV/m. Therefore using short beams offers great potential for making a meter-scale afterburner.

1.7 Computer simulations

Since the invention of the first digital computer half a century ago, computer simulation has emerged as a third method to understand complex physical phenomena which naturally complements theoretical analysis and experimental discovery. Computer simulation is now an invaluable tool for both understanding experimental results and for guiding the development of theory. In the past 20 years, there have been a tremendous amount of increase of the computing power

available. Just as other areas in science, plasma-based accelerator research has benefited from this increase of computing power and the advance of computer modeling.

To model the full scale of a plasma-based accelerator, one needs a code (or codes) that can model the evolution of the driver, the generation and evolution of the wake, and the acceleration of the trailing bunch of particles. It turns out, perhaps not surprisingly, that in most cases to do this properly one needs particle based models. That is, one needs to follow the trajectories of particles in their self-consistent fields. The reasons for this are that in many cases the wake excitation process is highly nonlinear and results in nonlaminar particle trajectories, and that any reasonable beam loading scenario will require very tight spot sizes. These situations cannot be modeled using fluid descriptions.

The most straightforward particle based model is the fully explicit PIC algorithm [57], which will be discussed in Chapter 2. In this algorithm, particles are loaded onto a spatially gridded simulation domain. The charge and current densities at the grid points can then be calculated by assigning the charge and current of nearby particles to the grid. These charge and current densities are used to advance the fields (also defined on the grid) via Maxwell's equations. The updated fields are used to advance the particles to new positions and velocities via the relativistic equation of motion,

Although simple in concept, there are many subtle issues related to how these equations are solved on a computer including the way in which charge and current are deposited on the grid and the way in which the equations of motion are integrated. Furthermore, because the algorithm makes the fewest physics approximations it is also very CPU intensive. The Courant condition for the stability of the explicit finite difference scheme requires that the time step must not exceed

the smallest spatial resolution of the simulation. This is a severe requirement for the total amount of computation.

An incredible amount of progress has been made during the past 20 years using the full PIC algorithm. The simulation models have been extended from 1D to 3D, and from serial to parallel. A collection of full PIC codes have appeared in the literature of plasma wakefield accelerator research. A few are summarized in Table 1.2. They are XOOPIC [58], OSIRIS [59], VLPL (Virtual Laser Plasma Lab) [60], VORPAL [61] and turboWAVE [62].

Code	Capability	Model	Geometry	S(erial)/ P(arallel)
XOOPIC	Laser/Particle	Fully EM, PIC	2D	P
OSIRIS	Laser/Particle	Fully EM, PIC	2D(slab/cy-, lindrical), 3D	P
VLPL	Laser/Particle	Fully EM, PIC	2D, 3D	P
VORPAL	Laser/Particle	Fully EM, PIC/ fluid	2D, 3D	P
turboWAVE	Laser	Fully EM + ponderomotive guiding center, PIC	2D, 3D	P
WAKE	Laser	Quasi-static, PIC	2D	S
LCODE	Particle	Quasi-static, PIC	2D	S
"Whittum"	Particle	Reduced quasi-static, PIC	3D	S
QuickPIC	Laser/Particle	Quasi-static, PIC	3D	P

Table 1.2: Codes currently used in plasma-based accelerator research and their features.

The first four of these five full PIC codes are general purpose codes and can model both laser and particle drivers. In principle they give the most exact results. The other codes in table 1.2 are reduced description codes which make approximations to the physical model and remove the fast time scales in the system in order to improve the speed.

TurboWAVE [62] is a 2D or 3D parallel code that has the option to use a fully explicit model for the plasma and a envelope model for the laser field solver. This option is algorithmically close to a full PIC model but the spatial and temporal resolutions are not required to resolve the laser oscillation. It is sometimes referred to as the ponderomotive guiding center model.

Another collection of codes are WAKE, LCODE, "Whittum" which is a code with no name and written by D.H. Whittum and the code QuickPIC which is described in detail in this dissertation. In these codes, the quasi-static approximation or frozen field approximation is used to reduce the computational requirement. In a PWFA or LWFA, there is a disparate difference of the time scales of the drive beam evolution and the plasma response. The quasi-static approximation takes advantage of this disparity of scales and separates the evolution of the driver from the plasma wake generation. Essentially, this approximation makes use of the fact that individual plasma electrons are passed over by the driver and its wake in a short time compared with the time over which the shape of the driver and wake evolve. Developing plasma based accelerator PIC codes using the quasi-static approximation was done independently by Mora and Antonsen [63] for laser drivers and by Whittum [64] for particle beam drivers. Mora and Antonsen's code, called WAKE, was confined to two dimensions and did not include the ability to model wake excitation from particle beams or to model beam loading. Whittum's code is three-dimensional but it does not include the evolu-

tion of a laser field and it solves an approximated set of the quasi-static wake field equations. These approximations are only appropriate for narrow driver beam bunches with moderate amounts of charge. Very recently, Lotov [27] reported on a 2D quasi-static code, LCODE, which is essentially identical to WAKE except that it can model PWFA but not LWFA.

In this dissertation, we describe in detail a new code, called QuickPIC, which makes the quasi-static approximation, but is fully three dimensional, is fully parallelized, puts no restrictions on the amount of beam charge, and can model both LWFA, PWFA, and beam loading. We will also show that QuickPIC can completely reproduce the results from a full PIC code such as OSIRIS with at least a savings of 100 in CPU time for extremely nonlinear conditions. (Furthermore, the quasi-static approximation does not suffer from unphysical Cerenkov radiation [57] that occurs in full PIC codes). The development of QuickPIC is not a straightforward extension of the 2D algorithms of Mora and Antonsen and of Lotov or the approximate 3D model of Whittum. Major complexities arise when the full quasi-static equations are solved in 3D instead of 2D, and when parallel routines are written with two types of distinct data structures, i.e., the driver (3D) and plasma particles (2D). In chapter 2, the quasi-static algorithm for efficiently modeling the plasma wakefield will be explained. The numerical implementation and the structure of QuickPIC will be presented in Chapter 3 and a few applications will be described in detail in Chapter 5 and 6.

CHAPTER 2

Particle-In-Cell simulation

In this chapter, we review the Particle-In-Cell (PIC) algorithm for plasma simulation. A general introduction to PIC codes is discussed in section 2.1. Next we describe the algorithm of a fully electromagnetic explicit PIC code and point out the reasons that they are computationally challenging for PWFA simulations. Then two simplified PIC models are introduced in section 2.3, they are the Darwin model for the magneto-static system and the quasi-static model for PWFA. Full quasi-static equations are also derived in this section which will be the foundation of QuickPIC.

2.1 Particle-In-Cell simulation

When experiments are impractical or too expensive to carry out to test a new idea in science and engineering, computer simulation can be an attractive alternative. In computer simulation, various strategies with different levels of approximations have been developed. When modeling plasma physics, there exist three different levels of description for the plasma and there are also three levels of approximation in implementing a "virtual" plasma environment using computer simulations. Among them are Particle-In-Cell(PIC) [65] codes, Vlasov codes and MHD fluid codes. In PIC codes, the plasma is described as a collection of superparticles, where each simulation particle can be regarded as a collection of

real electrons. While in Vlasov or MHD codes, the plasma is treated as phase space or configuration space fluid elements. The PIC method captures the particle nature of a plasma and makes the fewest approximations among these three methods. However, PIC codes are also the most computational demanding among the three methods.

The PIC method is composed of four computation steps. In the beginning of a computation cycle, a collection of particles are initialized, each representing a fixed or variable amount of real charged particles in the plasma. The charge and current densities are accumulated on a computational mesh dividing the simulation domain. The value of the electric and magnetic fields on the mesh are solved according to the governing field equations in a discrete space representation by finite difference or discrete Fourier series. The particles' positions and velocities are then updated using the fields just calculated. The whole simulation loops through these four steps(initialization, charge and current deposition, field advance, particle push) as time advances.

The field equations can be derived from the electro-static, magneto-static or electromagnetic model depending on their applicability to the problem of interest. In a full PIC code, the electromagnetic model of the fields is used. It describes the complete physics including radiation and finite speed of light effects. In section 2.2, the fully explicit PIC algorithm is introduced along with some examples. For other problems where such effects are not of significance, the field equations can be simplified. If the fields are slowly varying, the electro-static or magneto-static (Darwin) model can be used in a reduced description code. A reduced description is also suitable for the beam-plasma interaction using the quasi-static model, which removes the weak dependence of the fields on the propagation distance and separates the evolution of the drive beam particles and the plasma particles.

The Darwin and quasi-static model have some characteristics in common so they are discussed in detail in section 2.3.

2.2 Fully explicit PIC model

A fully explicit PIC code solves the dynamics of multiple species of charged particles in their self-consistent electromagnetic fields and any prescribed external field. The equation of motion for a charged particle is determined by the relativistic version of Newton's law,

$$\frac{d\mathbf{p}}{dt} = q(\mathbf{E} + \frac{\mathbf{v} \times \mathbf{B}}{c}). \tag{2.1}$$

where $\mathbf{p}$ is the momentum of the plasma particle, q is the charge of the particle and $\mathbf{E}$ and $\mathbf{B}$ are the total electric and magnetic fields. The displacement of each particle can then be determined by integrating the following equation in real space:

$$\frac{d\mathbf{r}}{dt} = \mathbf{v}. \tag{2.2}$$

In a real plasma, the trajectories of these particles determines field quantities like charge density ρ and current density $\mathbf{J}$ through the summation over all the particles,

$$\rho(\mathbf{r}) = \sum_{i=1}^{N} q\delta(\mathbf{r} - \mathbf{r}_i), \tag{2.3}$$

$$\mathbf{J}(\mathbf{r}) = \sum_{i=1}^{N} q\mathbf{v}_i\delta(\mathbf{r} - \mathbf{r}_i). \tag{2.4}$$

where N denote the total number of plasma particles and δ is Dirac delta function.

The charge and current densities are the source terms for the evolution of the electric and magnetic field through the Maxwell equations,

$$\nabla \cdot \mathbf{E} = 4\pi\rho, \tag{2.5}$$

$$\nabla \cdot \mathbf{B} = 0, \tag{2.6}$$

$$\nabla \times \mathbf{E} = -\frac{1}{c}\frac{\partial \mathbf{B}}{\partial t}, \tag{2.7}$$

$$\nabla \times \mathbf{B} = \frac{1}{c}\frac{\partial \mathbf{E}}{\partial t} + \frac{4\pi}{c}\mathbf{J}, \tag{2.8}$$

After taking the divergence of Eq. (2.8) and then using Eq. (2.5), it is trivial to find the following relation,

$$\frac{\partial \rho}{\partial t} + \nabla \cdot \mathbf{J} = 0, \tag{2.9}$$

This is the continuity equation which simply states that the number of charged particles is conserved in the system. For the simulation to be self-consistent, this condition has to be satisfied.

Similarly, taking the divergence of Eq. (2.7) recovers Eq. (2.6) as long as the the divergence of the magnetic field is zero initially.

Although the equations appear quite simple, the plasma dynamics can be extremely complicated because each individual trajectory matters. Therefore, for many problems a fluid description is not accurate.

In a PIC simulation each charged "superparticle" resides in the computer memory and represents a large number of real plasma particles. Each charged "superparticle" will have its velocity and position stored in the computer, as well as its charge and mass. The "superparticles" have much larger charge and greater mass than a real particle does. But since the equation of motion only involves the charge-to-mass ratio(q/m) of a particle, the "superparticle" in the simulation system will have the same trajectory as a real particle does as long as the charge-to-mass ratio is the same, thus assuring the simulation system would have a similar behavior as the real system.

The simulation system is not meant to be a exact replica of the real system. It approximates the reality in certain aspects. For example, the collisional effects would be different from a real plasma. A simulation system will exhibit more pronounced collision effects if "superparticles" are considered to be point charges (delta functions) in space. One approach to solve this problem is to stretch out the "superparticle" and assign a shape to the charge distribution. By doing this, one can effectively reduce the possibility of large angle scattering that would dominate because of the fewer number of particles in the simulation. However, small angle scattering still occurs and the system will relax to thermal equilibrium in a well understood manner. Furthermore, by using enough simulation particles, one can reduce the collision frequency to be less than the important frequencies in the problem under study.

Unlike the real world which has continuously varying physical quantities defined on continuous space-time variables, the simulation variables for space and time are discretized. This is done in order to solve the differential equations on a digital computer. The volume in which the plasma resides is divided into cells. Each cell is usually the same shape (usually a rectangular box), but the cell sizes in different directions can be different. Similarly, the temporal variable is also discretized, the advance in time then becomes the advance in timestep, usually with a constant time interval Δt.

On the other hand, the coordinates of a particle are still continuous, particles can move freely between cells. They are shown as red dots in Fig. 2.1. The electromagnetic fields are defined only at the grids, which are shown as blue diamonds in the same plot. When pushing the particles, the electric and magnetic fields at the grids near a particle's exact position need to be interpolated to define the fields at the location of the particle.

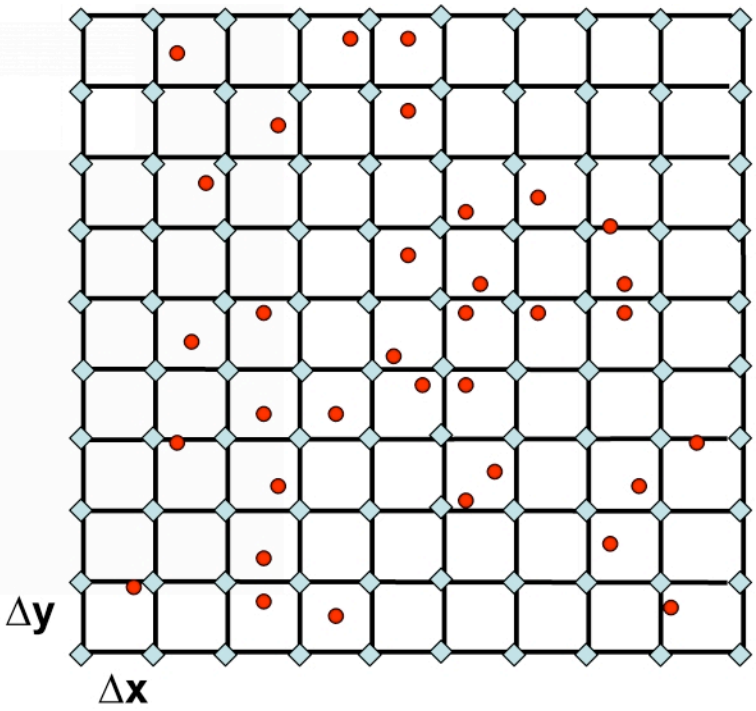

Figure 2.1: Schematic of a uniform mesh($\Delta x = \Delta y$) used in 2D PIC simulation. Particles are shown as red dots. Grid points are shown as blue diamonds.

The charge and current densities are also defined on the grids by weighting (depositing) the charge and current for each particle onto the grids. This is referred to as the charge or current deposition, and it is shown in Fig. 2.2. The weighting coefficient for each grid point is determined by the shape factor of the superparticle. For a linear shape factor, the weighting coefficient can be calculated using the relative area between the particle's position and the neighboring grid points as defined below.

$$w_1 = b \times d, \tag{2.10}$$

$$w_2 = a \times d, \tag{2.11}$$

$$w_3 = b \times c, \tag{2.12}$$

$$w_4 = a \times c. \tag{2.13}$$

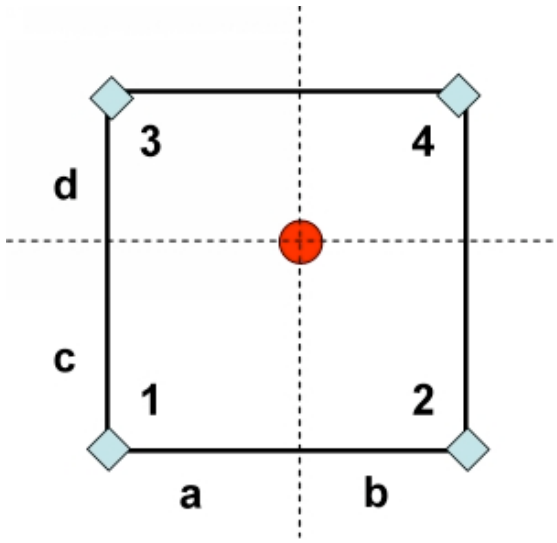

Figure 2.2: Illustration of the area weighting coefficient used for the charge and current deposition schemes in PIC codes.

The Maxwell equations need to be discretized to obtain a set of finite differential equations which correspond to Eq.(2.7) and Eq.(2.8),

$$B_{x,i,j}^{n+\frac{1}{2}} = B_{x,i,j}^{n} - c\frac{\Delta t}{2} \times \frac{E_{z,i,j+1}^{n} - E_{z,i,j}^{n}}{\Delta y}, \tag{2.14}$$

$$B_{y,i,j}^{n+\frac{1}{2}} = B_{y,i,j}^{n} + c\frac{\Delta t}{2} \times \frac{E_{z,i+1,j}^{n} - E_{z,i,j}^{n}}{\Delta x}, \tag{2.15}$$

$$B_{z,i,j}^{n+\frac{1}{2}} = B_{z,i,j}^{n} - c\frac{\Delta t}{2} \times \frac{E_{y,i+1,j}^{n} - E_{y,i,j}^{n}}{\Delta x} + c\frac{\Delta t}{2} \times \frac{E_{x,i,j+1}^{n} - E_{x,i,j}^{n}}{\Delta y}, \tag{2.16}$$

$$E_{x,i,j}^{n+1} = E_{x,i,j}^{n} - 4\pi\Delta t \times J_{x,i,j}^{n+\frac{1}{2}} + c\Delta t \times \frac{B_{z,i,j}^{n+\frac{1}{2}} - B_{z,i,j-1}^{n+\frac{1}{2}}}{\Delta y}, \tag{2.17}$$

$$E_{y,i,j}^{n+1} = E_{y,i,j}^{n} - 4\pi\Delta t \times J_{y,i,j}^{n+\frac{1}{2}} - c\Delta t \times \frac{B_{z,i,j}^{n+\frac{1}{2}} - B_{z,i-1,j}^{n+\frac{1}{2}}}{\Delta x}, \tag{2.18}$$

$$E_{z,i,j}^{n+1} = E_{z,i,j}^{n} - 4\pi\Delta t \times J_{x,i,j}^{n+\frac{1}{2}} + c\Delta t \times \frac{B_{y,i,j}^{n+\frac{1}{2}} - B_{y,i-1,j}^{n+\frac{1}{2}}}{\Delta x} - c\Delta t \times \frac{B_{x,i,j}^{n+\frac{1}{2}} - B_{x,i,j-1}^{n+\frac{1}{2}}}{\Delta y}. \tag{2.19}$$

Here, for simplicity we assume the simulation is done in a 2D-Cartesian coordinate system. The superscripts n denotes the time index, and subscripts x, y and z denote the field components and i and j denote grid indices in x and y directions respectively.

The fact that the particle have continuous variables and the fields have discrete variables leads to subtle numerical instabilities caused by the particle quantities aliasing onto the grid. These can be suppressed by using smoothing or filtering on the current and charge density once they have been deposited. In the code QuickPIC which will be described in the next chapter, we use a Gaussian filter in k space which can also be viewed as an additional Gaussian particle shape factor for smoothing.

Eq. (2.5) and Eq. (2.6) are typically dropped in the simulation because they are guaranteed if Eq. (2.7) and Eq. (2.8) are solved for the simulation and the following two conditions are met. The first condition is that initially the **B** field should be divergence free and that $\nabla \cdot \mathbf{E} = 4\pi\rho$ is satisfied; the second one is that the charge and current deposition schemes used in the simulation must satisfy the continuity equation or the longitudinal part of **E** needs to be corrected every time step. Although the first condition is trivial to satisfy, the second one usually requires careful consideration.

One should also notice that in the above implementation of the field solver, the electric field is defined on integer time indices and the magnetic field is defined on half integer time indices. Thus the discretized Maxwell equations are properly time-centered and this is consistent with the discretization of the particle push. Time-centering the field solver and particle pusher is desirable because it produces less error and also eliminates the need for an iteration loop.

Once **E** and **B** are updated using Eq.(2.14) - Eq. (2.19), the particle push is repeated and the new values of **E** and **B** are used to update the particles' positions and velocities as described before. This entire process can be repeated until the specified time is reached. The schematic flow chart in Fig. 2.3 illustrates the calculation cycle in a typical PIC code.

In a PIC simulation, however, the grid size sets a lower limit to the spatial resolution of particle-particle and field-particle interactions. It is obvious that smaller grid sizes will improve accuracy in the calculation, but the total number of grids is limited by the available memory. For many plasma simulations, a requirement that the result be meaningful is that the grid size should resolve the Debye length. This is because Debye length is the scale length of variation in the potential produced by a "dressed" charge in the plasma. The Debye length

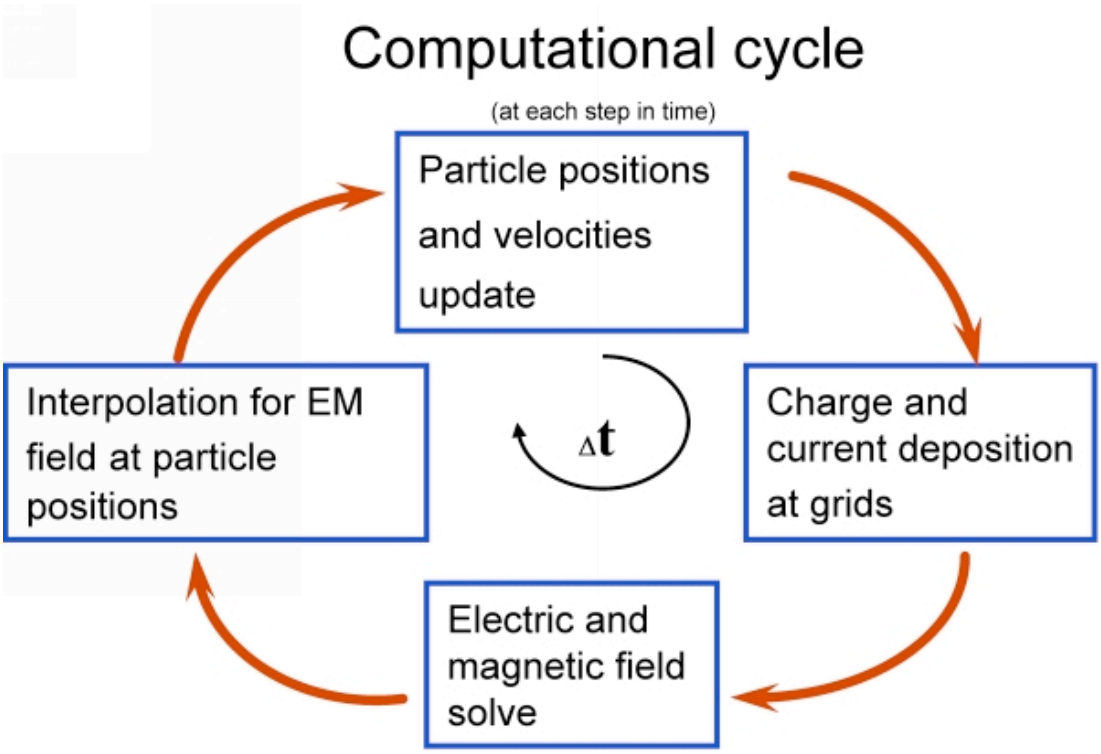

Figure 2.3: Schematic of a calculation cycle in PIC codes.

is defined as $\sqrt{kT/4\pi e^2 n_0}$, where k is Boltzman's constant, T is the electron temperature, e is the electron charge and n_0 is the plasma density. The collective behavior of the plasma particles are preserved when the grid size is sufficiently small as compared to the Debye length (In some cases, such as that of a PWFA, a cold plasma is assumed, then it is the collisionless skin depth c/ω_p that needs to be resolved).

The time interval Δt for successive updates is also subject to some requirements. Δt should resolve the characteristic time scale of plasma oscillation. Furthermore, in an electromagnetic algorithm, Δt must be smaller than $\Delta x/c$ (in 1D) to avoid a numerical instability. This is called the Courant condition. This can also be understood by the fact that Δx determines the shortest wavelength. Using the dispersion relation for light, one can then find the highest frequency and Δt much be chosen to resolve it.

From a statistics point of view, the field on the grid will fluctuate due to the randomness of particle motion. To reduce the effect of this fluctuation or "noise", a sufficient amount of particles are needed in the simulation.

The requirements for grid size Δx, time interval Δt and the number of particles are the major limitations for the PIC code. Furthermore, knowing what they must be for properly modeling a problem comes from experience. An incredible amount of progress has been made during the past 20 years using the full PIC algorithm [66], however, because the algorithm makes few physics approximations it is also very CPU intensive. Full scale 3D simulations for PWFA using codes based on this type of algorithm, such as OSIRIS, often resort to massively parallel computing techniques. Using a full PIC code it takes $\sim 10^{13}$ particle pushes to model a single GeV PWFA stage (and $\sim 10^{14}$ to model a GeV LWFA stage). On today's fastest computers, such a simulation takes $\sim 10,000$ ($100,000$

for LWFA) CPU hours; thus it is very expensive to run. Clearly, it is not possible to model 50 GeV or greater stages using the full PIC method. In the following section, an alternative approach is discussed and the quasi-static PIC algorithm is developed.

2.3 Reduced description PIC models

The fully electromagnetic PIC method introduced in section 2.2 is very mature. In principle the result from a full PIC simulation contains all the physics as long as the wavelength and frequency of the plasma behavior are properly resolved. However many real plasma behaviors span an enormous range of time and spatial scales. It is sometimes not possible or not necessary to use full dynamics models. Reduced description PIC codes take advantage of the vastly different time or spatial scales and make approximations to the field equations in order to relax the requirements of temporal or spatial resolution that arises in a full PIC code due to numerical instabilities. The most widely used reduced PIC code is the electro-static PIC code in which Poisson's equation is used to solve for the electric field, and the magnetic field is dropped. The physical meaning of the electro-static model is obvious and the implementation is simple, however, the Darwin model and the quasi-static model discussed next require careful investigation.

2.3.1 Darwin model

The purely electromagnetic modes are the most difficult to resolve in a full PIC model. In particular, electromagnetic modes with phase velocity v_ϕ substantially less than the speed of light can exist in a plasma. However in a full PIC

code, if the cell size is chosen to resolve the relevant wavelengths, the time step has to be chosen to resolve modes with phase velocities at c. There are many techniques that eliminate electromagnetic modes when they are not important in the problem. It was known by Darwin [67] that one proper way to retain the most physics in the low but non-zero phase velocity limit is to use a magneto-inductive version of the Maxwell equations. The approach of Darwin is to make the next lowest order terms beyond the electrostatic model. The electrostatic model is the $v/c \to 0$ limit of Maxwell equations, while the Darwin model is an expression of the fluid-particle Lagrangian to $O((v/c)^2)$. Therefore, it can model electromagnetic modes with $0 < v_\phi/c < 1$.

From the Helmholtz's theorem, a vector can always be decomposed into two parts, one is the solenoidal part which can be written as the curl of a vector potential and the other one is the irrotational part which can be obtained from the gradient of a scalar potential. In the Darwin model [68, 69, 70, 71], the electric field is decomposed into $\mathbf{E}_{sol}$ and $\mathbf{E}_{irr}$, which satisfy,

$$\nabla \cdot \mathbf{E}_{sol} = 0, \tag{2.20}$$

$$\nabla \times \mathbf{E}_{irr} = 0. \tag{2.21}$$

It is convenient to express the solenoidal component as,

$$\mathbf{E}_{sol} = \mathbf{E} + \nabla\phi = -\frac{1}{c}\frac{\partial \mathbf{A}}{\partial t}, \tag{2.22}$$

where the scalar potential ϕ is determined from,

$$\nabla^2\phi = -4\pi\rho, \tag{2.23}$$

as results from the use of the radiation or Coulomb gauge.

The irrotational part of $\mathbf{E}$ is calculated from,

$$\mathbf{E}_{irr} = \mathbf{E} - \mathbf{E}_{sol} = -\nabla\phi. \tag{2.24}$$

The Darwin limit of the Maxwell equation arises when the solenoidal part of the displacement current is small and dropped from the Ampere's law, i.e., Eq. (2.8), the new equation has a similar form,

$$\nabla \times \mathbf{B} = \frac{1}{c}\frac{\partial \mathbf{E}_{irr}}{\partial t} + \frac{4\pi}{c}\mathbf{J}. \tag{2.25}$$

Taking the curl of Eq. (2.25), and using Eq. (2.6), the equation for the magnetic field can be written as,

$$-\nabla^2\mathbf{B} = \frac{4\pi}{c}(\nabla \times \mathbf{J}). \tag{2.26}$$

Eqs. (2.23), (2.24) and (2.26) are solved in a Darwin code for the fields. In addition, $\mathbf{E}_{sol}$ is determined from the Faraday's law,

$$\nabla \times \mathbf{E}_{sol} = -\frac{1}{c}\frac{\partial \mathbf{B}}{\partial t}. \tag{2.27}$$

This equation needs to be evaluated with proper boudary condition to ensure Eq. (2.20).

The right hand side of Eq. (2.25) can be defined as,

$$-\frac{1}{c}\frac{\partial \nabla\phi}{\partial t} + \frac{4\pi}{c}\mathbf{J} \equiv \mathbf{J}_{sol}, \tag{2.28}$$

where the irrotational parts of the displacement current and of the real current must cancel(within the accuracy of a constant), so that only the solenoidal

component $\mathbf{J}_{sol}$ is left. Eq. (2.28) and hence the Darwin model is completely consistent with the continuity equation,

$$\frac{\partial \rho}{\partial t} + \nabla \cdot \mathbf{J} = 0, \tag{2.29}$$

because $-\nabla^2 \psi = 4\pi\rho$ from Eq. (2.23).

Eq. (2.29) is the same equation as Eq. (2.9), hence normal charge and current deposition schemes in the PIC code can be used to guarantee the self-consistency of the simulation. It is an advantage of the Darwin code that much of a full PIC code can be reused while the requirement to resolve the highest frequency component of the fields is removed. It does however require a predictor-corrector loop because the particle and field equations are no longer time centered. As we will see in the later section, the reduced description model sometimes requires that special charge and current deposition schemes be used. The Darwin system is the lowest order correction to an electrostatic model because it comes from an expansion in powers of v/c of the Hamiltonian that includes the interaction between particle and fields. The Darwin model has been around for many years. A model with similar looking equations but completely different physics is the quasi-static model in the next section.

2.3.2 Quasi-static PIC model

The physics of plasma based acceleration allows one to make approximations that can, in principle, reduce the computational needs significantly and that are extremely accurate. In a plasma accelerator stage a short drive beam (either a laser pulse or particle beam) propagates through long regions of plasma and a trailing beam of electrons or positrons gets accelerated by the resulting wake. The

driver and trailing beam evolve on a very different length scale than the plasma wake wavelength or the driver length. In a fully explicit code, one needs to choose a cell size that resolves the shortest length scale (either the laser wavelength or the plasma wavelength) and the time step is constrained by the Courant condition. For typical plasma accelerator parameters, the drive beam might not evolve for over 1000's of time steps. For example, for a PWFA the drive beam evolves on the scale of the betatron wavelength which is $(2\gamma)^{1/2}$ times longer than the plasma wavelength. For a 50 GeV beam this is a factor of $\sim$ 500 times longer. For a LWFA the driver evolves on the Rayleigh length which is also orders of magnitude longer than the wavelength of the wake (for LWFA the shortest spatial scale is the laser wavelength so the potential CPU savings of reduced models over the fully explicit method can be considerably higher).

In this section we describe the physical model that forms the basis of QuickPIC and the quasi-static approximation that QuickPIC employs. We begin by describing the model equations without a laser driver, then we will add the laser driver to the model in the later chapter. Without any other approximations, a full set of quasi-static equations for PWFA simulations can be derived from the Maxwell's equations. In the mildly non-linear case, one could also exploit more approximations for both the beam and plasma dynamics, resulting in a simplified version of the quasi-static equations. The full quasi-static equations will be reviewed next and then the simplified version will be introduced later. The structure of the code will be described in the next chapter.

We start from the Maxwell's equations in the Lorentz gauge,

$$(\frac{1}{c^2}\frac{\partial^2}{\partial t^2} - \nabla^2)\phi = 4\pi\rho, \tag{2.30}$$

$$(\frac{1}{c^2}\frac{\partial^2}{\partial t^2} - \nabla^2)\mathbf{A} = \frac{4\pi}{c}\mathbf{J}, \tag{2.31}$$

where the Lorentz gauge is defined as,

$$\nabla \cdot \mathbf{A} = -\frac{1}{c}\frac{\partial \phi}{\partial t}. \tag{2.32}$$

An individual particle's trajectory is governed by Eq.(2.1), and $\mathbf{E}$ and $\mathbf{B}$ can be obtained from the following equations,

$$\mathbf{E} = -\nabla\phi - \frac{1}{c}\frac{\partial \mathbf{A}}{\partial t}. \tag{2.33}$$

$$\mathbf{B} = \nabla \times \mathbf{A}. \tag{2.34}$$

The coordinate system is chosen to be three dimensional Cartesian, i.e., (x,y,z), with z being the direction in which the beam is propagating. We use the lab frame as our reference frame. The scalar potential ϕ and vector potential $\mathbf{A}$ are functions of spatial and temporal variables (x, y, z, t). Since we are only interested in the region where there is beam-plasma interaction, a moving observation window can then be applied to the problem. This window will move at the speed of light c which is slightly faster than the drive beam, and snapshots of this window are taken as the beam is propagating in the plasma. If there is no beam-plasma interaction, the beam will appear stationary in the snapshot taken through our observation window. We define this mathematical transformation from z, t to two new variables s, ξ,

$$s = z, \tag{2.35}$$

$$\xi = ct - z. \tag{2.36}$$

The center of the moving window can be described by $s_w = ct, \xi_w = 0$. The variable s can be regarded as the propagation distance into the plasma, and ξ as the position with respect to the moving window's center(in our notation, the beam is moving in the +z direction, which means the value of ξ will be smaller at the head of the beam than that at the tail and this is shown in Fig. 2.4).

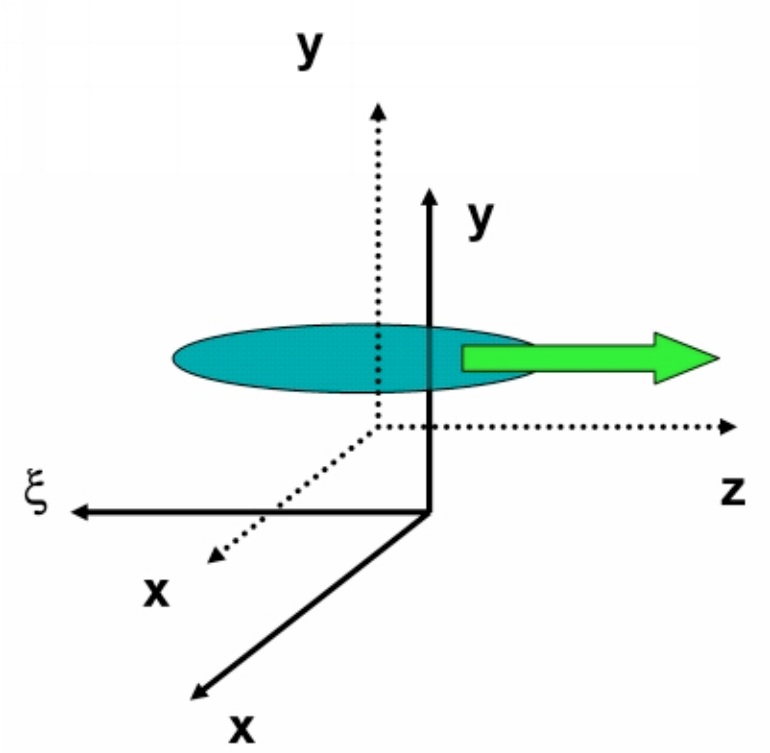

Figure 2.4: Schematic of the coordinate system used in QuickPIC.

With the definitions of these two new variables, the derivatives of field quantities with respect to z and t can be written in terms of derivatives with respect to s and ξ,

$$\frac{\partial}{\partial z} = \frac{\partial}{\partial s} - \frac{\partial}{\partial \xi}, \tag{2.37}$$

$$\frac{1}{c}\frac{\partial}{\partial t} = \frac{\partial}{\partial \xi}. \tag{2.38}$$

The coordinates s and ξ now represent two disparate scales of the particles' motion and their associated fields. This leads to the quasi-static approximation which will be discussed in detail soon. Before the quasi-static approximation is introduced, we shall discuss the motion of the particles first.

The particles in the drive beam are moving at a speed very close to c, e.g., for a 30 GeV beam, $1 - v/c \approx 1.4 \times 10^{-10}$. Due to their higher inertia (mass), they respond much more slowly to the plasma collective fields than do the plasma electrons and ions. The higher the beam energy, the slower its evolution will be, in other words, the "stiffer" the beam appears to be. In addition, the space charge expansion and the magnetic pinching from the self-fields of the beam nearly cancel out to order $1/\gamma^2$ because of the relativistic velocity in z, although these self-fields are both large respectively. Therefore, only the plasma fields can lead to the transverse motion of the beam particles. Furthermore, due to the slow evolution of the beam shape, the plasma electrons and the field structure around the beam will be "frozen" during the typical time scale of the beam evolution. In the moving window variables, this time scale is represented by s which is a spatial variable suitable for integrating the equation of motion of a beam particle. This is illustrated in Fig. 2.5.

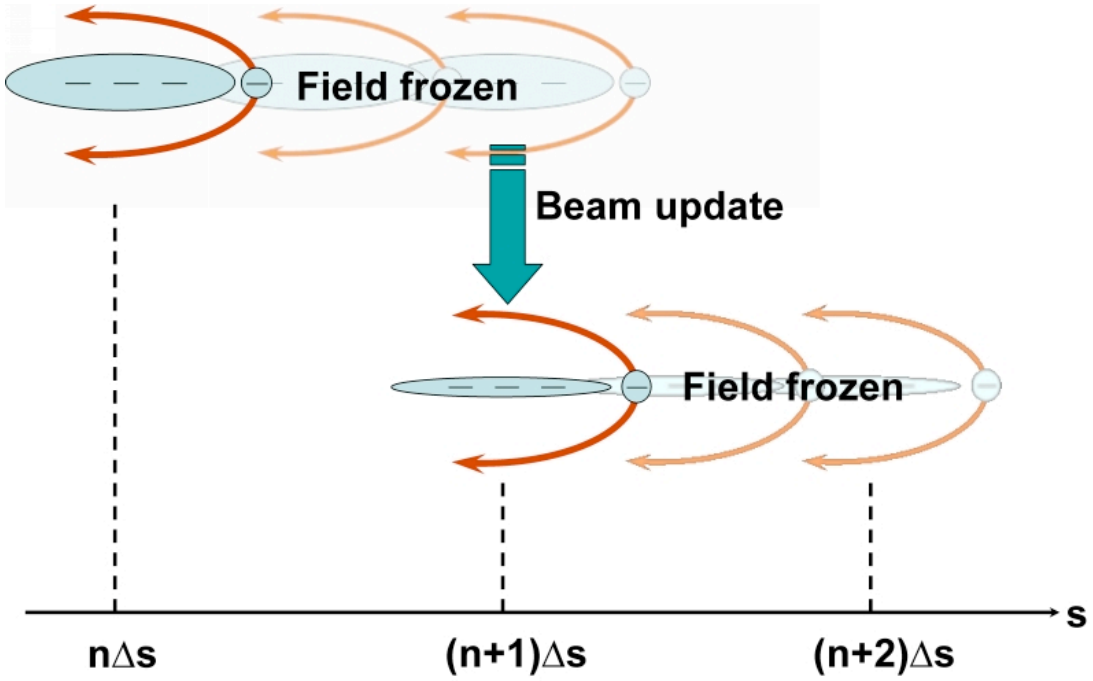

Figure 2.5: The drive beam and the plasma response. Electromagnetic fields are frozen between successive beam updates.

To understand how the plasma evolves, consider the cartoon in Fig. 2.6. Following the beam, an observer sees plasma electrons moving to the left. The relative distance of a plasma electron to the head of the beam can be measured by the variable ξ. To properly evolve a plasma electron's trajectory, the longitudinal distance $\Delta\xi$ a plasma electron moves through must be small compared to both the bunch length and the resulting plasma wavelength. The plasma electrons sweep through the beam and generate the fields which act on the beam. For example, a hollow ion channel is formed if the drive beam is an electron beam because the plasma electrons are expelled outward by the beam space charge and the ions which are more massive do not respond in the time it takes the electron to move past the beam.

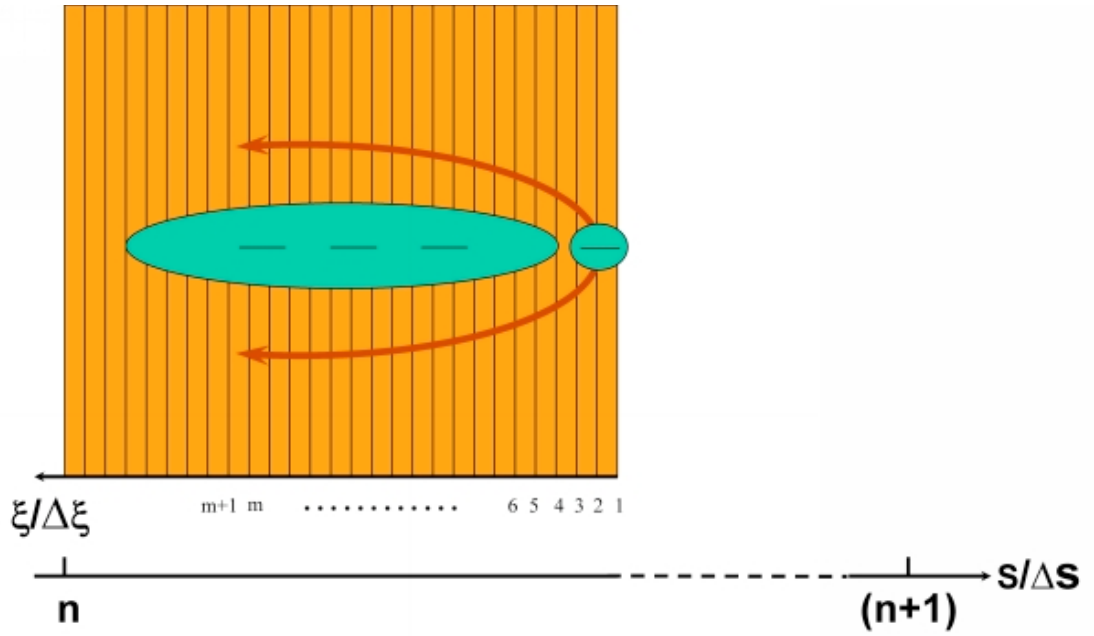

Figure 2.6: Physical picture of how the plasma evolves. It also shows the relation between Δs and $\Delta\xi$.

As stated above, the variables s and ξ can be used to measure the slow time scale of the beam evolution and the fast time scale of the plasma oscillation. For a better understanding of these two disparate time scales, a general discussion of a particle's trajectory as a function of time will be helpful. A general trajectory for a particle's position $z(t)$ is plotted in Fig. 2.7(a). Also plotted in Fig. 2.7(b) is the inverse function $t(z)$. Note that function $z(t)$ has a single well-defined value for any t, but the inverse function $t(z)$ does not necessarily have this property. A particle can come back to its old position at any time, thus for a known position z, one may find multiple values of t from Fig. 2.7(b). This tells us that the temporal variable has a unique feature that spatial variables do not have. However, other than this distinct feature, there is no difference between a temporal variable and a spatial variable regarding the particle's motion.

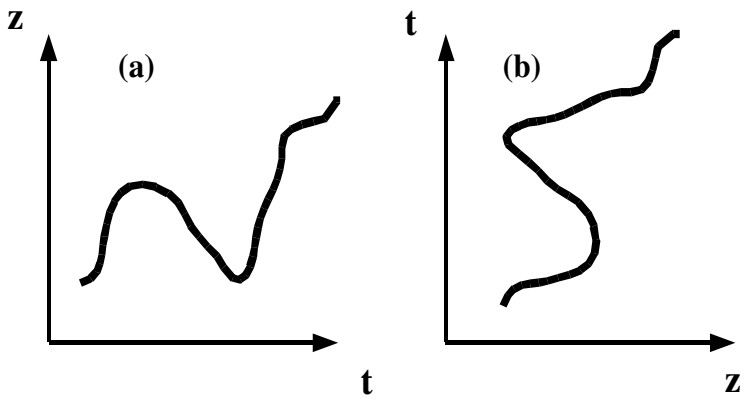

Figure 2.7: Particle's trajectory in 1D can be plotted as z(t) or t(z).

This leads to a simple but unusual way to integrate particle's trajectory using the inverse of the equation of motion,

$$\frac{dt}{dz} = \frac{1}{v}. \tag{2.39}$$

This is equivalent to viewing z as the time-like variable and t as space-like variable. If a particle's motion varies rapidly in one coordinate compared to the other then it may be advantageous to view the variable with the slow dependence to be time-like.

In the beam-plasma interaction problem we would like to investigate, there are two distinct groups of particles of interest, i.e., beam particles which almost move at the speed of light, and plasma particles whose longitudinal and transverse motions are local in the lab frame unless they are trapped in the wakefield and move with the driver. Using the moving window coordinates (s,ξ), their trajectories are completely different. These are shown in Fig. 2.8.

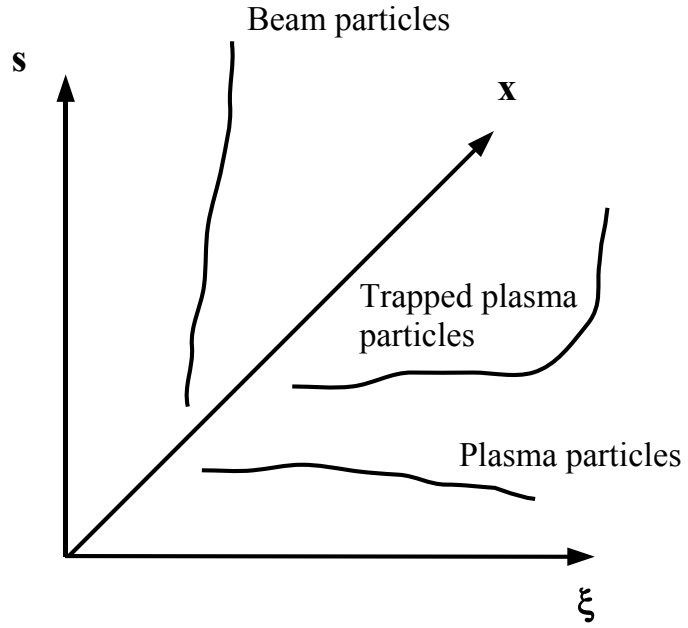

Figure 2.8: Trajectories of plasma and beam particles in (s,ξ,x) space.

In the s - ξ plane shown in Fig. 2.8, beam particles move almost vertically due to their large longitudinal velocities which are close to c. For most of the

plasma particles, the longitudinal momenta they obtain are finite during the short time for the beam to pass by, therefore their total displacements in s are very small. They move predominantly to the right in Fig. 2.8. However, some plasma particles' longitudinal velocities may be larger enough to keep up with the beam, their trajectories are also shown in Fig. 2.8. For most of parameters of interest in PWFA, trapped particles are uncommon, so we do not need to consider them here. Then it is natural that one would treat plasma particles and beam particles differently due to their distinct trajectories. In fact, one can integrate the equation of motion in different forms for these two kinds of particles. It means that the choice of integration variable should reflect the characteristics of their motion.

For a beam particle, we use the variable $s_w(t) = ct$ to advance its trajectory $(x_b(s_w(t)), y_b(s_w(t)), \xi_b(s_w(t)))$ since it is a slow-varying function of $s_w(t)$. The equations used are,

$$\frac{d\mathbf{P}_b}{ds_w} = \frac{q_b}{c}(\mathbf{E} + \frac{\mathbf{V}_b}{c} \times \mathbf{B}), \tag{2.40}$$

$$\frac{d\mathbf{x}_{b\perp}}{ds_w} = \frac{\mathbf{P}_{b\perp}}{\gamma_b m_e c}, \tag{2.41}$$

$$\frac{d\xi_b}{ds_w} = 1 - \frac{P_{bz}}{\gamma_b m_e c}, \tag{2.42}$$

where $\mathbf{E} = \mathbf{E}(x(s), y(s), \xi(s); s)$ and $\mathbf{B} = \mathbf{B}(x(s), y(s), \xi(s); s)$.

Under the linear focusing force from the ion channel, the beam particle executes betatron motion [28]. Therefore the corresponding "timestep" Δs_w should resolves the betatron wavelength λ_β.

For a plasma particle, the trajectory $(x_p(\xi_p(t)), y_p(\xi_p(t)), s_p(\xi_p(t)))$ can be integrated using $\xi_p(t)$ as the time variable for the equations of motion,

$$\frac{d\mathbf{P}_p}{d\xi_p} = \frac{q_p}{c - V_{pz}}(\mathbf{E} + \frac{\mathbf{V}_p}{c} \times \mathbf{B}), \tag{2.43}$$

$$\frac{d\mathbf{x}_{p\perp}}{d\xi_p} = \frac{\mathbf{P}_{p\perp}}{\gamma_p m_e (c - V_{pz})}, \tag{2.44}$$

$$\frac{ds_p}{d\xi_p} = \frac{P_{pz}}{\gamma_p m_e (c - V_{pz})}, \tag{2.45}$$

where $\mathbf{E} = \mathbf{E}(x(\xi), y(\xi), s(\xi); \xi)$, $\mathbf{B} = \mathbf{B}(x(\xi), y(\xi), s(\xi); \xi)$ and the relationship $d\xi_p = (1 - V_{pz}/c)cdt$ was used.

Since most plasma particles do not move far away from their original positions s_{p0} when the beam pass through, Eq. (2.45) is not integrated. This is reasonable as long as the fields, $\mathbf{E}$ and $\mathbf{B}$, depend weakly on s_p which is precisely the quasi-static condition that will be discussed soon, i.e., $\partial\mathbf{E}/\partial s \approx 0$ and $\partial\mathbf{B}/\partial s \approx 0$. However, the moving window is moving at the speed of light, thus the following relation

$$\frac{ds_w}{d\xi_p} = \frac{1}{1 - V_{pz}/c}, \tag{2.46}$$

needs to be taken into account since there are particle leaving and entering the window. Eq. (2.46) indicates that for a plasma particle with a larger parallel velocity, the distance the moving window travels or the time it takes a particle to move a distance $\Delta\xi$ is longer. It is necessary to consider this factor when weighting the particle's charge and current in the moving window.

As the driver sweeps over the plasma, plasma particles continuously follow the trajectories determined by Eqs. (2.43) and (2.44). Thus, to calculate the plasma contribution to the local charge and current density on a grid in (x, y, ξ) space depending on V_{pz} it is necessary to account for the different amount of time a particle will spend in region $\Delta\xi$. The plasma particle charge and current density

are therefore accumulated on a grid by using the following deposition schemes for charge density and current,

$$\rho_p = \frac{1}{Volume} \sum_i \frac{q_{pi}}{1 - V_{pzi}/c}, \tag{2.47}$$

and

$$\mathbf{J}_p = \frac{1}{Volume} \sum_i \frac{q_{pi}\mathbf{V}_{pi}}{1 - V_{pzi}/c}. \tag{2.48}$$

Here the sum is over particles contributing to the charge and current densities at a given grid point. This sum must include weighting factors to distribute the particle charge to neighboring grid points.

Since the beam evolves on the time scale of betatron period, its charge and current density can be written as $\rho_b(x, y, \xi, s)$ and $\mathbf{J}_b(x, y, \xi, s)$ which depend weakly on the variable s. Therefore, the plasma response $\rho_p(x, y, \xi, s)$ and $\mathbf{J}_p(x, y, \xi, s)$ also depend weakly on s, unless the plasma particle interacts with the beam continuously, e.g., when trapping happens and the plasma particle moves along with the beam. For an ultra-relativistic beam whose speed is very close to c and $\gamma_b >> 1$, the plasma particle cannot gain enough energy during the interaction with the beam for trapping to happen so such a situation is not common in our problem. Therefore, the source terms in Eqs. (2.30) and (2.31) also exhibit weak dependence on s. Thus, the so-called "frozen-field" or "quasi-static" approximation, i.e.,

$$\frac{\partial}{\partial s} \ll \frac{\partial}{\partial \xi}, \tag{2.49}$$

can then be taken when the Lorentz factor γ_b of the beam is large.

Eq.(2.37) then becomes,

$$\frac{\partial}{\partial z} \approx -\frac{\partial}{\partial \xi}, \tag{2.50}$$

and Eq.(2.30) and Eq.(2.31) are reduced to simpler forms,

$$\nabla_\perp^2 \phi = -4\pi\rho, \tag{2.51}$$

$$\nabla_\perp^2 \mathbf{A} = -\frac{4\pi}{c}\mathbf{J}, \tag{2.52}$$

where we define the operator $\nabla_\perp^2 \equiv \partial^2/\partial x^2 + \partial^2/\partial y^2$. The derivatives in this operator are only in the transverse direction, which means that the fields in one transverse slice at position ξ depend only on the charge and current density in the same slice. Thus Eq.(2.51) and Eq. (2.52) can be solved using a 2D Poisson solver.

The modified field equations under the quasi-static approximation remove the strictest requirement to resolve the shortest wavelength in the system. Unlike the parabolic Maxwell's equations, Eqs. (2.51) and (2.52) are elliptical. There is no explicit time derivative in these equations. Therefore there is no Courant condition and hence no numerical limit to the maximum time step that one can use. Instead, the only requirement of the time step comes from the equation of motion. As described before, the time step only needs to resolve the plasma oscillation.

Here the field equations are written for potentials ϕ and $\mathbf{A}$ in the Lorentz gauge. In fact the quasi-static approximation can be applied to the equations of the $\mathbf{E}$ and $\mathbf{B}$ directly. Once ϕ and $\mathbf{A}$ are obtained for a particular transverse slice, it is trivial to calculate $\mathbf{E}$ and $\mathbf{B}$ in Eq. (2.33) and Eq. (2.34) from the potentials. Eq. (2.33) can be rewritten in new variables,

$$\mathbf{E} = -\nabla\phi - \frac{\partial \mathbf{A}}{\partial \xi}, \tag{2.53}$$

while the expression for the longitudinal component of $\mathbf{E}$ can be further simplified,

$$E_z = \frac{\partial \psi}{\partial \xi}. \tag{2.54}$$

Here a new scalar potential ψ is introduced,

$$\psi = \phi - A_z, \tag{2.55}$$

where A_z is the longitudinal component of the vector potential $\mathbf{A}$. ψ is also referred to as the "pinch potential" [64], because it determines the focusing field acting on the beam particle moving with $\mathbf{V}_b = \hat{z}c$ through

$$\mathbf{E}_{focusing} = \mathbf{E}_\perp + \hat{z} \times \mathbf{B} = -\nabla_\perp \psi. \tag{2.56}$$

The expression for the Lorentz gauge is now,

$$\nabla_\perp \cdot \mathbf{A}_\perp = -\frac{\partial \psi}{\partial \xi}, \tag{2.57}$$

which can be used to update the potential ψ for each transverse slice.

Under the quasi-static approximation, the axial momentum of plasma particles can be obtained via the constant of the motion [63] (also see Appendix A),

$$\gamma_p - \tilde{P}_{pz} = 1 - \tilde{q}_p \tilde{\psi}, \tag{2.58}$$

where $\tilde{P}_{pz} = P_{pz}/mc$, $\tilde{q}_p = q_p/e$ and $\tilde{\psi} = \psi e/(mc^2)$. This relation also gives,

$$\tilde{P}_{pz} = \frac{1 + \tilde{P}_{p\perp}^2 - (1 - \tilde{q}_e \tilde{\psi})^2}{2(1 - \tilde{q}_e \tilde{\psi})}, \tag{2.59}$$

and

$$\gamma_p = \frac{1 + \tilde{P}_{p\perp}^2 + (1 - \tilde{q}_e \tilde{\psi})^2}{2(1 - \tilde{q}_e \tilde{\psi})}. \tag{2.60}$$

Therefore, once $\tilde{\psi}$ and $\tilde{P}_{p\perp}$ are known one can also calculate $V_{pz} = P_{pz}/\gamma_p$. Furthermore, Eq. (2.45) is not integrated so there is no need to update V_{pz} through the normal PIC algorithm. Since we do not need to integrate the s_p trajectory, nor update V_{pz}, it becomes possible and convenient to use a 2D PIC

algorithm to model the plasma particles with Eqs. (2.59) and (2.60) for the longitudinal momentum and the relativistic Lorentz factor which normally require information of the third dimension. This algorithm will bring substantial time savings to the quasi-static model in addition to the removal of the Courant condition.

2.3.2.1 Full quasi-static PIC algorithm

We have derived the equations for the quasi-static approximation in the above section. Based on these equations, the quasi-static PIC algorithm can be designed. In this section, we will summarize the equations for the quasi-static PIC algorithm. The implementation will be described in detail in the next chapter. Under certain situations, a simplified algorithm based on further assumptions to the simulation parameters can be derived. The implementation of this simplified algorithm is easier and the efficiency is higher. This simpler algorithm is not accurate enough for typical PWFA experiments, e.g., those at SLAC; however it is useful for modeling the e-cloud interaction in circular accelerators [72]. This algorithm will be reviewed in the next section and some discussion on its validity will be given.

The full quasi-static PIC algorithm consists of the following equations,

1. Field equations, Eqs. (2.51), (2.52), (2.53)), (2.53), (2.54), (2.55), (2.57);
2. Equations of motion, Eqs. (2.40), (2.41), (2.42), (2.43), (2.44), (2.59);
3. Charge and current deposition, Eqs. (2.47), (2.48).

In deriving the field equations, the only approximation made is Eq. (2.49). This approximation is valid as long as the beam driver's Lorentz factor $\gamma_b >> 1$.

Since this condition is well satisfied for PWFA, the full quasi-static equations are a very accurate description for the ultra-relativistic beam-plasma interactions. A PIC model based on these equations is fully kinetic and nonlinear but will be significantly faster than the fully explicit PIC simulation for PWFA.

Advancing the beam particles can be quite challenging if one needs to include the self-forces. This is because the self-forces cancel to one part in 10 billion for a ultra-relativistic beam with $\gamma_b = 10^5$. Since it can be shown that the plasma forces dominate, we typically modify the equation of motion by assuming that $V_{bz} = c$ in the Lorentz force for a beam particle. Therefore, Eq. (2.40) can be written as,

$$\frac{d\mathbf{P}_{b\perp}}{ds_w} \approx \frac{q_b}{c}\mathbf{E}_{focusing} = -\frac{q_b}{c}\nabla_\perp \psi, \tag{2.61}$$

$$\frac{d\mathbf{P}_{bz}}{ds_w} \approx \frac{q_b}{c}\mathbf{E}_z = -\frac{q_b}{c}\frac{\partial \psi}{\partial \xi}. \tag{2.62}$$

Eqs. (2.61) and (2.62) replace Eq. (2.40). These two equations together with other equations described in this section form a set of underlying full quasi-static equations used in QuickPIC.

Finally, we comment on the self-consistency of the full quasi-static model. This is done by checking the charge continuity equation. From Eq. (2.51) and the $\hat{z}$ component of Eq. (2.52), one can obtain the Poisson equation for ψ,

$$\nabla_\perp^2 \psi = -4\pi(\rho - J_z/c). \tag{2.63}$$

Furthermore, if one takes the Laplacian of Eq. (2.57) and substitutes Eq. (2.63), one obtains the continuity equation implied by the quasi-static model,

$$\frac{\partial(c\rho - J_z)}{\partial \xi} + \nabla_\perp \cdot \mathbf{J}_\perp = 0. \tag{2.64}$$

Since $\rho = \rho_b + \rho_p$, $\mathbf{J}_\perp = \mathbf{J}_{b\perp} + \mathbf{J}_{p\perp}$ and $J_z = J_{bz} + J_{pz}$, the beam and the plasma charge and current density both need to satisfy Eq. (2.64). The charge and current deposition schemes introduced in Eqs. (2.47) and (2.48) allow the plasma charge and current densities to satisfy the quasi-static continuity equation Eq. (2.64). However, the beam charge and current densities obtained through standard PIC deposition scheme satisfy Eq. (2.9), not Eq. (2.64). Therefore, solving the quasi-static field equations with the calculated $\mathbf{J}_b$ and ρ_b is not self-consistent. Since $|J_{bz}| >> |\mathbf{J}_{b\perp}|$ and $J_{bz} \approx c\rho_b\hat{z}$, one can avoid this problem by simply dropping the term $\mathbf{J}_{b\perp}$ and assuming $J_{bz} \equiv c\rho_b\hat{z}$. This is completely consistent with our use of Eq. (2.61) and (2.62) rather than the full Lorentz force.

2.3.2.2 Basic Quasi-static PIC code

Under some conditions, e.g., low current drivers, the plasma electron trajectories are mostly in the radial direction and their velocities are non-relativistic. If these conditions are met, the equations for the fields and the equations of motion can be reduced to very simple forms. With the above assumptions,

$$\mathbf{J} = \mathbf{J}_p + \mathbf{J}_b \approx J_{bz}\hat{z} \approx \rho_b c\hat{z}. \tag{2.65}$$

Thus $\mathbf{A}_\perp = 0$, and only the longitudinal component A_z is non-zero. The field equations are then cast into two scalar Poisson equations,

$$\nabla_\perp^2 \phi = -4\pi\rho = -4\pi(\rho_b + \rho_p + \rho_{ion}), \tag{2.66}$$

$$\nabla_\perp^2 \psi = -4\pi(\rho_p + \rho_{ion}), \tag{2.67}$$

where ρ_b, ρ_p, ρ_{ion} are charge density for the beam, the plasma electron and the ion respectively. These two equations can be easily solved in 2D space with

established computation techniques.

Finally, we assume that $\gamma_b \approx \gamma_0$ and $\gamma_p \approx 1$, which implies that the energy gain we consider here for the beam would be small and there is no relativistic plasma electrons generated. As noted above, these are true only for the case in which "blow-out" is not very nonlinear. The equations of motion of the beam particle take the same form as Eqs. (2.61) and (2.62), while the equations of motion for the plasma electrons can be approximated by ignoring the longitudinal motion, i.e., $V_{pz} = 0$. Furthermore, since $\mathbf{A}_\perp = 0$, B_z also vanishes. Combining all these approximations results in,

$$\frac{d\mathbf{P}_{p\perp}}{d\xi_p} = -\frac{q_p}{c}\nabla_\perp \phi, \tag{2.68}$$

$$\frac{d\mathbf{x}_{p\perp}}{d\xi_p} = -\frac{\mathbf{V}_{\mathbf{p}\perp}}{c}. \tag{2.69}$$

This set of equations can be implemented using 2D Poisson solver and a 2D non-relativistic pusher with ξ being the time-like variable. The plasma particles move on a 2D grid of the transverse coordinates and are advanced forward in the variable ξ while s is kept fixed. The beam particles are advanced forward in the s coordinate using the fields calculated from the plasma evolution. This algorithm was implemented in the first phase of QuickPIC code, which we referred to as Basic QuickPIC [73]. This algorithm is identical to that by Whittum [64]. The above approximations pose severe limits to the nonlinear beam-plasma interaction one can simulate. As shown in [73], with $\Lambda \equiv \frac{n_b}{n_0} k_p^2 \sigma_r^2 \sim 0.06$ (Λ, the normalized beam charge per unit length, determines how nonlinear the interaction is), results from Basic QuickPIC deviate slightly from the OSIRIS result. While for the benchmarks in chapter 4, where $\Lambda = 0.9$, the results have large deviations. The basic QuickPIC approximations lead to larger energy gain/lost and larger hosing

growth of the beam.

2.3.3 Numerical Instability

The Darwin model and the quasi-static model both make assumptions to the hyperbolic Maxwell's equations. The modified field equations are both elliptical equations which represent the instantaneous nature of signal propagation. It turns out that on one hand these modifications remove the fastest time scales in the system, making the simulation easier; on the other hand, there is a numerical instability associated with the use of elliptical field equations and the PIC algorithm. This has been reported in [68, 71, 74] and it has been the major obstacle in developing a simulation code based on the Darwin model. The root of this numerical instability has been discussed in detail in the literature. It has been shown that neglecting the solenoidal part of the displacement current in the Ampere's law Eq. (2.8) is equivalent to omitting the time derivative in the Maxwell's equations Eqs. (2.30) and (2.31). Thus retardation is removed from the solution to the Maxwell's equations. The effect is analyzed in ref. [68] using Lagrangian variables and the numerical instability is found to be absolute. To proceed with a stable algorithm with the Lagrangian variables, Nielson [68] obtained an expression of $\mathbf{E}_{sol}$ using higher moments of the distribution function instead of the time derivative of the current $\partial\mathbf{J}/\partial t$. However, the additional calculations needed to accumulate the higher order moments and solve the new equation for $\mathbf{E}_{sol}$ are cumbersome and they affect the total efficiency greatly.

Another way to to resolve the instability problem is to use the Hamiltonian and its associated variables [68, 75]. The equations are rewritten in the canonical momentum, $\mathbf{P}_c = \mathbf{P} + q\mathbf{A}/c$, instead of the mechanical momentum. This eliminates the need to evaluate the $\partial\mathbf{J}/\partial t$ term required in the Lagrangian formulas.

However the formulas in [68] still contain the time derivative $\partial\phi/\partial t$, therefore a predictor-corrector loop is needed to properly time-center the equations. A code based on this algorithm was found to be stable. In ref. [75], a Vlasov equation which uses Hamiltonian variables was solved for, but a similar problem of $\partial\phi/\partial t$ is handled using the Vlasov equation under the Darwin approximation.

As noted before, the quasi-static model shares a lot of common characteristics with the Darwin model. The quasi-static approximation, i.e. Eq. (2.49), makes the Maxwell's equations elliptical and hence allows instantaneous interactions between particles in one transverse slice. This is clearly seen in Eq. (2.51) and (2.52), where the vector potential $\mathbf{A}$ is determined by $\mathbf{J}$ without retardation. Furthermore, to calculate the electric field by Eq. (2.53), one has to know the vector potential $\mathbf{A}$ at a future time, which in turn requires the particle's motion to be determined for the future time. Therefore, a stable algorithm is needed for self-consistency and for avoiding positive feedbacks in the calculation. In the numerical implementation this is done by iteration and diffusion damping. This situation does not arise in normal PIC codes where the particle equations and field equations can be advanced sequentially because they are time centered. The problem can be traced to the cancellation of time and space derivatives in the field equations that occur in the drive beam frame, which makes the electromagnetic interaction local in ξ. However, the reason of numerical instability only exists in the full quasi-static algorithm. For a basic quasi-static algorithm such as the basic QuickPIC and Whittum's code, since $\mathbf{A}_\perp$ is dropped from the calculation, the algorithm is always stable. Nonetheless, the neglect of $\mathbf{A}_\perp$ is not valid for many cases of interest.

From the experience of the Darwin model, a predictor-corrector iteration loop can be used for properly time-centering the full quasi-static algorithm. But this

does not resolve the numerical instability. The solution we adopt is to rewrite the quasi-static Maxwell's equations into diffusion equations that allow local errors to diffuse across the simulation box in a desirable amount of iteration. The diffusion equations are parabolic so that the propagation speed of the signal is finite and adjustable through the diffusion coefficients. The details of the implementation are discussed in Chapter 3.

2.4 Summary

In this chapter, we started from Maxwell equations and described the conventional PIC algorithm. The Darwin and quasi-static reduced description models were introduced. We derived a set of full quasi-static equations for modeling PWFA. This set of equations was further simplified by making assumptions that are valid for some PWFA parameters. The full quasi-static equations were then summarized in a form which can be implemented into the PIC framework. The numerical instabilities encountered with the Darwin and the quasi-static model were explained and two general methods to remove the instability were briefly introduced. In the next chapter, we will focus on the implementation of the quasi-static model into a PIC algorithm, i.e., the code QuickPIC.

CHAPTER 3

Implementation of QuickPIC

In this chapter, we describe how the set of full quasi-static equations are solved numerically and the software design strategy for QuickPIC including details on the structure of the code. For simplicity, we begin by assuming there is only a particle beam driver and leave the discussion of how to include the laser's ponderomotive force until the end. Other topics such as the PIC Framework used in QuickPIC, the parallelization method and the performance are also discussed in this chapter.

3.1 Algorithm

We use the particle-in-cell (PIC) technique [57, 65], which is introduced in Chapter 2, combined with the full quasi-static equations summarized in section 2.3.2.1. Many pieces of the field solvers, the current and charge deposition routines and the particle push routines can be found in legacy codes. These legacy codes are usually well optimized, tested and documented. In QuickPIC, we use a PIC simulation framework as the foundation which is built upon a large collection of legacy PIC code components. This Framework is discussed in section 3.2, it consists of standard 3D and 2D PIC simulation codes. We reuse the components provided by the Framework and design our algorithm to fit into the 3D and 2D PIC code structures. This allowed for the rapid development of the QuickPIC

code. In this section, many issues such as the moving window, plasma update, beam update, iteration and initialization etc. are discussed. And the parallelization structure of QuickPIC will be presented in sections 3.2 and 3.3 with a brief discussion of the code performance in section 3.4.

3.1.1 Moving window

The idea of a moving window algorithm is widely used in plasma accelerator simulation codes, e.g. in OSIRIS [76], VORPAL [61], VLPL [60] and turboWAVE [62]. The moving window follows the interaction region which is typically very short compared with the propagation length. The moving window is usually moving at the speed of light and new particles are initialized at the front of the window at rest and particles that lag behind the interaction region are abandoned. The field and their derivatives are initialized to zero at the front of the window.

In the full electromagnetic codes mentioned above, lab frame variables, i.e. (x, y, z, t), are used. To implement a moving window using the full PIC algorithm requires that the fields (particles) on the grids should be shifted in the moving direction (the counter-moving direction) at each time step. In QuickPIC, the moving window algorithm is implemented by adopting two new variables defined by Eqs. (2.35) and (2.36), where the variable s can be regarded as the propagation distance into the plasma, and ξ as the position relative to the moving window center. The center of the moving window is defined as $(x_w = 0, y_w = 0, s_w = ct, \xi_w = 0)$. Since the quasi-static model assumes that the plasma response evolves on a time scale slower compared to the inverse plasma frequency $1/\omega_p$, the plasma in the moving window is refreshed during the interval of the beam update and one does not need to shift the particles or fields as is required in a full PIC code.

Fig. 3.1 is a cartoon showing the moving window which follows the drive

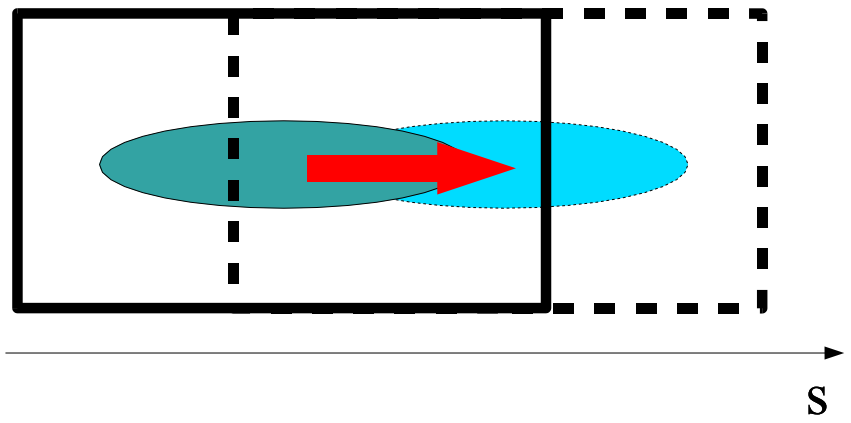

Figure 3.1: A moving window with velocity c is used to follow beam's evolution.

beam.

3.1.2 Plasma and beam update

Developing an efficient code based on the full quasi-static equations is not straightforward. While the system described is fully three dimensional, only the two transverse coordinates (x, y) always remain space-like. For the beam particles ξ is also space-like and s is time-like; while for plasma particles s is space-like and ξ is time-like. At a given value of s the beam particles are distributed throughout a three-dimensional (x, y, ξ) grid. The charge and current densities of the beam are deposited using standard area weighting (or higher order spline) methods. At each value of s, we then initialize a collection of plasma particles at an initial value of ξ sufficiently ahead of the driver. The x and y coordinates of each plasma particle are advanced forward in ξ (backward through the beam) using Eqs. (2.43), (2.44) with electric and magnetic fields arising from the charges

and currents from both the plasma and the beam. The key assumption is that the variable s_p is assumed to be the same for every plasma particle during the advance in ξ, i.e., we do not integrate s_p in ξ and we ignore the weak dependence of the forces on s_p.

At a given ξ the fields are calculated using Eqs. (2.51), (2.52) and (2.57) where ρ and $\mathbf{J}$ from the plasma are calculated in Eqs. (2.47) and (2.48) using area weighting (or higher order splines) methods, and where ρ and $\mathbf{J}$ from the beam have already been calculated (we do not use the transverse current $\mathbf{J}_{b\perp}$ from the beam since it is small compared with the longitudinal beam current and it is not needed to satisfy the continuity equation under the quasi-static approximation). The value of V_z for each plasma particle is determined from Eqs. (2.59) and (2.60). Once the trajectories of the particles $(x(\xi), y(\xi))$ have been advanced forward in ξ by a desired amount such that the beam has passed them, then the beam particles are advanced in s. This cycle can be repeated a desired number of "time" steps in s. This flow is illustrated in Fig. 3.2. The structure of the algorithm therefore is that of a two dimensional (x, y) PIC code with the ξ being a time-like variable, embedded in a three-dimensional (x, y, ξ) PIC code with s being the time-like variable.

We now describe the details of the numerics in the two dimensional part. At a point in the two-dimensional loop where the electric and magnetic fields are known, plasma particles are updated with the Lorentz force. Although the equations of motion are fully relativistic, they can be cast into the form of a non-relativistic Boris pusher [77] with a modified electric field and an effective charge q_{eff} to simplify calculation.

$$\frac{d\mathbf{u}_{p\perp}}{d\xi} = \frac{q_{eff}}{m_e}\left[\gamma_p \mathbf{E}_\perp + \left(\frac{\mathbf{u}_p}{c} \times \mathbf{B}\right)_\perp\right] \tag{3.1}$$

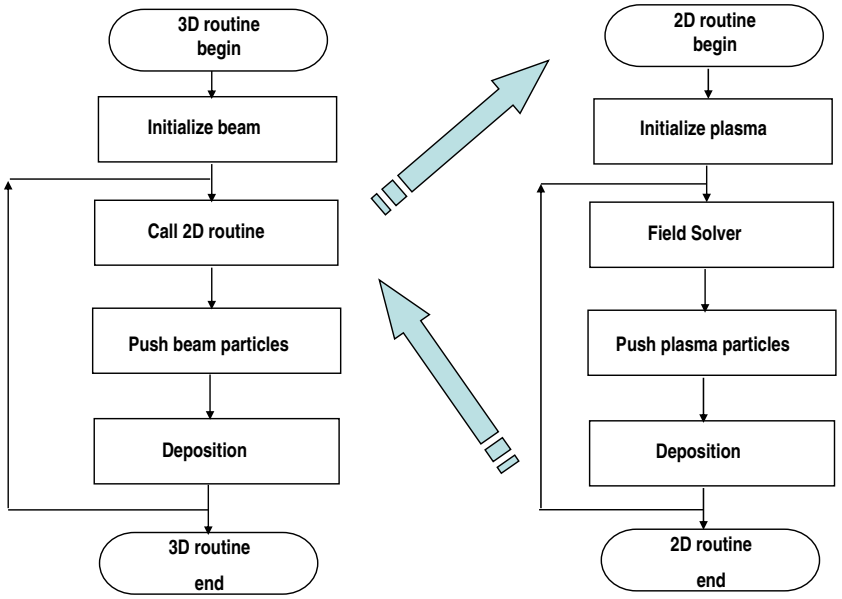

Figure 3.2: Flow chart of the QuickPIC quasi-static algorithm showing a 2D routine embedded in a 3D routine.

and

$$\frac{d\mathbf{x}_{p\perp}}{d\xi} = \frac{\mathbf{u}_{p\perp}}{1 - q_p\psi/m_e c^2}. \tag{3.2}$$

where the definition of the effective charge is

$$q_{eff} \equiv \frac{q_p}{1 - q_p\psi/m_e c^2}. \tag{3.3}$$

In deriving Eqs. (3.1)-(3.2), Eq. (2.58) is used to express the relativistic factor and we use the proper velocity $\mathbf{u} = \gamma\mathbf{V}$.

For the discrete version of Eqs. (3.1)-(3.2), quantities are either known at half or full integer grid values of ξ, i.e., $\xi = (m + 1/2)\Delta\xi$ or $\xi = m\Delta\xi$, where m is an integer labeling the grid values. We chose that at an integer grid value the proper velocities are known. Then it is natural to presume that the particle positions will be known on half integer grid values. To second order in $\Delta\xi$ the particle positions can be computed for the $(m + 1/2)$ step by using Eq. (3.2) for a half time step $\Delta\xi/2$.

As ξ is incremented from the front to the end of the moving window, the plasma response and all the fields are solved for and stored at each transverse 2D slice using the above numerical algorithm. Then the drive beam, which exists in 3D space, should be pushed using these fields for a large time step Δs. The beam momenta are known at half integer steps in s and the beam positions are known at full integer steps. When the 2D loop is finished it returns the necessary fields to the 3D loop to update the beam at a full integer value of s. This update uses the standard leap-frog algorithm and is therefore time-centered with second order accuracy in Δs. The step Δs only needs to resolve the betatron motion of the beam particles. The equations used are Eqs. (2.61), (2.62), (2.41) and

(2.42) with proper normalization. Then the charge density is deposited and the 2D cycle is started again for the updated beam driver. The 3D beam update and the charge deposition were taken directly from the UPIC Framework to be described in section 3.2 shortly. The 3D loop does not require any field-solves so it typically uses a small fraction of the total computation time.

3.1.3 Charge and current depositions

The charge and current depositions of plasma particles are not standard. With the definition of q_{eff}, the depositions become,

$$\rho_p = \frac{1}{Volume} \sum_i \frac{q_{pi}}{1 - V_{pzi}/c} = \frac{1}{Volume} \sum_i \gamma_{pi} q_{eff}, \tag{3.4}$$

and

$$\mathbf{J}_p = \frac{1}{Volume} \sum_i \frac{q_{pi}}{1 - V_{pzi}/c} \mathbf{V}_{pi} = \frac{1}{Volume} \sum_i q_{eff} \mathbf{u}_{pi}, \tag{3.5}$$

where

$$\gamma_{pi} = \frac{1 + \mathbf{u}_{pi\perp}^2/c^2 + (1 - q_{pi}\psi/m_e c^2)^2}{2(1 - q_{pi}\psi/m_e c^2)}, \tag{3.6}$$

and

$$u_{piz} = \frac{1 + \mathbf{u}_{pi\perp}^2/c^2 - (1 - q_{pi}\psi/m_e c^2)^2}{2(1 - q_{pi}\psi/m_e c^2)}. \tag{3.7}$$

Therefore the deposition routines only require minor changes. The fact that a given simulation particle does not represent a fixed amount of charge can be viewed another way. The continuity equation for a collection of discrete particles each with charge Q_i is

$$0 = \frac{\partial}{\partial t} \sum_i Q_i \delta(\mathbf{x} - \mathbf{x}_i(t)) + \nabla \cdot \left[\sum_i Q_i V_i(t) \delta(\mathbf{x} - \mathbf{x}_i(t)) \right]. \tag{3.8}$$

Under the quasi-static approximation this reduces to

$$0 = \frac{\partial}{\partial \xi} \sum_i Q_i \left[1 - \frac{V_{zi}(\xi)}{c} \right] \delta(\mathbf{x}_\perp - \mathbf{x}_{\perp i}(\xi)) + \nabla_\perp \cdot \left[\sum_i Q_i \frac{V_{\perp i}(\xi)}{c} \delta(\mathbf{x}_\perp - \mathbf{x}_{\perp i}(\xi)) \right]. \tag{3.9}$$

Therefore, at any value of ξ we can integrate along x and y to obtain

$$0 = \frac{d}{d\xi} \sum_i Q_i \left[1 - V_{zi}(\xi)/c \right]. \tag{3.10}$$

So, when advancing plasma electrons forward in ξ, the quantity $Q_i(1 - V_{zi}/c) = q_i$, not Q_i, of each particle is constant. From which it follows that the charge on each particle is $Q_i = q_i/(1 - V_{zi}/c)$, where q_i is a constant.

3.1.4 Iteration and Diffusion damping

The equation of motion Eq. (3.1) requires the evaluation of the wake electric and magnetic fields. These are given in terms of the scalar and vector potentials. The axial component of vector potential is determined by taking the difference between ϕ and ψ,

$$A_z = \phi - \psi. \tag{3.11}$$

The electric field and magnetic field can then be found using the following equations,

$$\mathbf{E}_\perp = -\nabla_\perp \phi - \mathbf{A}_{\perp \xi}, \tag{3.12}$$

$$E_z = \frac{\partial}{\partial \xi}\psi, \tag{3.13}$$

$$\mathbf{B}_\perp = (\mathbf{A}_{\perp\xi} + \nabla_\perp A_z) \times \hat{z}, \tag{3.14}$$

$$B_z = [\nabla_\perp \cdot (\mathbf{A}_\perp \times \hat{z})]\hat{z}, \tag{3.15}$$

where we define $\mathbf{A}_{\perp\xi}$ as

$$\mathbf{A}_{\perp\xi} \equiv \frac{\partial \mathbf{A}_\perp}{\partial \xi}. \tag{3.16}$$

The quantity $\mathbf{A}_{\perp\xi}$ satisfies a 2D Poisson equation

$$-\nabla_\perp^2 \mathbf{A}_{\perp\xi} = 4\pi \mathbf{J}_{\perp\xi}/c, \tag{3.17}$$

with a source term $\mathbf{J}_{\perp\xi} \equiv \partial \mathbf{J}_\perp / \partial \xi$.

The equation of motion Eq. (3.1) and Eq. (3.17) need to be solved consistently. For the field equations Eq. (3.17) which relates $\mathbf{A}_{\perp\xi}$ to $\mathbf{J}_{\perp\xi}$, the relation is clear; while for the particle equation of motion one needs to consider that a portion of $\mathbf{E}_\perp$ is proportional to $\mathbf{A}_{\perp\xi}$. If one were to sum over particles in a box, the equation of motion would relate $\mathbf{J}_{\perp\xi}$ to $\mathbf{A}_{\perp\xi}$. Furthermore, this set of equations is not time centered. For both of these reasons, an iteration loop will be required when these equations are discretized in ξ.

It is assumed that the particle positions will be known on half integer grid values, and the particle proper velocities are known at an integer grid value. However, the only fields that can be computed straightforwardly are $\mathbf{A}_\perp$ and

hence $\nabla_\perp \cdot \mathbf{A}_\perp$ at index m by using Eq. (2.51) and (2.52), and ψ which can be computed at the $(m+1)$ step by using the gauge condition Eq. (2.57).

Therefore, the need for some type of iteration method is clear. In order to compute the new proper velocity at $(m+1)$ the fields at the $(m+1/2)$ step are needed; but in order to compute the fields at the $(m+1/2)$ step the currents and charge density at $(m+1/2)$ and hence the proper velocity at $(m+1/2)$ are needed.

The iteration starts by predicting $\mathbf{J}_\perp^{m+1/2}$, $\mathbf{J}_{\perp\xi}^{m+1/2}$ and $\rho^{m+1/2}$, it continues by using these predictions to compute all of the fields at $(m+1/2)$, which are then used to advance the particles, and then the proper velocity at index $(m+1)$ is used to correct the prediction for $\mathbf{J}_\perp^{m+1/2}$, $\mathbf{J}_{\perp\xi}^{m+1/2}$ and $\rho^{m+1/2}$. This is summarized in Table 3.1 and the details are given next.

We assume that the derivative of a quantity in ξ is zero if no information about the derivative is known. The predictions for $\mathbf{J}_\perp^{m+1/2}$, $\mathbf{J}_{\perp\xi}^{m+1/2}$ are therefore,

$$\mathbf{J}_{\perp,l=0}^{m+1/2} = \mathbf{J}_\perp^m + (\Delta\xi/2)\cdot \mathbf{J}_{\perp\xi}^{m-1/2}, \tag{3.18}$$

$$\mathbf{J}_{\perp\xi,l=0}^{m+1/2} = \mathbf{J}_{\perp\xi}^{m-1/2}, \tag{3.19}$$

where l is an iteration index.

The prediction of $\rho^{m+1/2}$ is done as follows,

$$\rho^{m+1/2} = \rho_b^{m+1/2} + \rho_p^{m+1/2} \approx (\rho_b^m + \rho_b^{m+1})/2 + \frac{1}{Volume}\sum_i \frac{\gamma_{pi}^{m+1/2}\cdot q_{pi}}{1 - q_{pi}\cdot \psi^{m+1/2}/m_e c^2} \tag{3.20}$$

	$m-1/2$	m	$m+1/2$	$m+1$	$m+3/2$
Presumed quantities	ψ, $\mathbf{J}_{\perp\xi}$	$\mathbf{u}_{p\perp}$, $\mathbf{J}_{\perp}$	$\mathbf{x}_{p\perp}$		
Quantities calculated before iteration		$\mathbf{A}_{\perp}$, $\nabla_{\perp} \cdot \mathbf{A}_{\perp}$	ψ		
Predicted quantities			$\mathbf{J}_{\perp}$, $\mathbf{J}_{\perp\xi}$, γ, ρ		
Quantities known after iteration			ϕ, A_z, $\mathbf{A}_{\perp}$, $\mathbf{A}_{\perp\xi}$, $\nabla_{\perp} \cdot \mathbf{A}_{\perp}$, $\mathbf{B}_{\perp}$, B_z, $\mathbf{E}_{\perp}$	ψ, u_{pz}, $\mathbf{u}_{p\perp}$, $\mathbf{J}_{\perp}$	$\mathbf{x}_{p\perp}$

Table 3.1: Quantities and their roles in the 2D cycle and the corresponding 2D time step at which they are defined.

Note that for each value of s the beam quantities are known at all integer values of m so that to compute ρ_b at a half integer index we take the average. In Eq. (3.20), only $\gamma^{m+1/2}$ is unknown and needs to be predicted. The prediction is done using Eq. (3.6) and the previous value of $\mathbf{u}_{p\perp}$,

$$\gamma_{pi,l=0}^{m+1/2} = \frac{1 + (\mathbf{u}_{p\perp}^{m}/c)^2 + (1 - q_{pi}\psi^{m+1/2}/m_e c^2)^2}{2(1 - q_{pi}\psi^{m+1/2}/m_e c^2)}. \tag{3.21}$$

The other field-related quantities such as ϕ, A_z, $\mathbf{A}_\perp$, $\mathbf{A}_{\perp\xi}$, $\nabla_\perp \cdot \mathbf{A}_\perp$, $\mathbf{B}_\perp$, B_z and $\mathbf{E}_\perp$ can now be solved using Eqs. (2.51) and (3.11)-(3.16) at index $(m+1/2)$ and ϕ^{m+1} can also be obtained through the gauge condition Eq. (2.57). Using the predicted forces, we advance the particles proper velocity and positions to their next time index, with $\mathbf{x}_{p\perp}$ at $(m+3/2)$, $\mathbf{u}_{p\perp}$ and $\mathbf{J}_\perp$ at $(m+1)$. The results $\mathbf{u}_{p\perp}^{m+1}$ and $\mathbf{J}_\perp^{m+1}$ are then used to make a correction to the previous prediction,

$$\mathbf{J}_{\perp\xi,l}^{m+1/2} = (\mathbf{J}_{\perp,l-1}^{m+1} - \mathbf{J}_\perp^{m})/\Delta\xi, \tag{3.22}$$

$$\mathbf{J}_{\perp,l}^{m+1/2} = (\mathbf{J}_\perp^{m} + \mathbf{J}_{\perp,l-1}^{m+1})/2, \tag{3.23}$$

$$\gamma_{pi,l}^{m+1/2} = \frac{1 + [(\mathbf{u}_{pi\perp}^{m} + \mathbf{u}_{pi\perp,l-1}^{m+1})/2c]^2 + (1 - q_{pi}\psi^{m+1/2}/m_e c^2)^2}{2(1 - q_{pi}\psi^{m+1/2}/m_e c^2)}. \tag{3.24}$$

The predictor-corrector loop can be repeated an arbitrary number of times. One way to terminate the loop is to wait until a desired accuracy is reached. However, as discussed in section 2.3.3, the algorithm presented above suffers from one kind of numerical instability similar to one that occurs in Darwin codes. The low $\mathbf{k}$ modes of $\mathbf{A}_{\perp\xi}$ are the most unstable, they grow rapidly and soon dominate the whole electric and magnetic fields in a few iterations. The problem actually exists in the field solver. If one views the iteration number as a pseudo-time variable, the numerical instability arises from the instantaneous nature of the solution to the elliptical field equation in the pseudo-time. As we notice earlier in section 2.3.3, several methods including the moment method and the

canonical momentum method were proposed in the literature to remedy this. However, incorporating these methods into QuickPIC would involve significant modifications and they are sometimes impractical. Instead, in QuickPIC we modified the Poisson solver in the iteration loop so that it resembles a diffusion equation. Eqs. (3.16) and (2.51) are modified as follows respectively,

$$D_J \frac{\partial}{\partial T} \mathbf{A}_{\perp\xi} = \nabla_\perp^2 \mathbf{A}_{\perp\xi} + 4\pi \mathbf{J}_{\perp\xi}/c, \tag{3.25}$$

$$D_\rho \frac{\partial \phi}{\partial T} = \nabla_\perp^2 \phi + 4\pi\rho. \tag{3.26}$$

where D_J and D_ρ are the diffusion coefficients. We define the pseudo-time as $T = l\Delta T$, then the above equations can be rewritten in the discrete variable l,

$$(1 - \frac{1}{D_J}\nabla_\perp^2)\mathbf{A}_{\perp\xi,l} = \mathbf{A}_{\perp\xi,l-1} + \frac{1}{D_J}\mathbf{J}_{\perp\xi,l}, \tag{3.27}$$

$$(1 - \frac{1}{D_\rho}\nabla_\perp^2)\phi_l = \phi_{l-1} + \frac{1}{D_\rho}\rho_l. \tag{3.28}$$

In the above equations, ΔT is absorbed into D_J and D_ρ so there is no need to consider it anymore. A diffusion equation is parabolic, thus any local error in the source term $\mathbf{J}_{\perp\xi}$ or ρ cannot propagate across the simulation box instantly in one iteration. Local errors are indeed damped over the pseudo-time and the calculation can converge to the correct solution in a few iterations if D_J and D_ρ are chosen appropriately. Since numerous calculations are involved in an iteration loop, it is desirable to have as few iterations as possible to speed-up the code. For diffusion equations like Eqs. (3.25) and (3.26), the characteristic diffusion length is $L_D = \sqrt{4Dl}$, where we have chosen $D_J = D_\rho = 1/D$ for simplicity. Because normally a particle will not move more than one transverse grid size Δx

during one real time step $\Delta\xi$, the scale length of the changes in $\mathbf{J}_{\perp\xi}$ and ρ during this time will be on the order of Δx. Thus, we should allow diffusion over this distance to happen in the whole iteration process, i.e., $L_{D,max} = \sqrt{4Dl_{max}} = \Delta x$, which gives an estimate for the choice of D, $D = (\Delta x)^2/4l_{max}$. In practice, we use $l_{max} = 2$ and have found through experimentation that $D = (\Delta x)^2$ gives the most rapid convergence and the best accuracy over a wide range of parameters. These choices are used for the QuickPIC runs that are presented in Chapter 4. In the present implementation of QuickPIC, all transverse spatial derivatives are done in Fourier space using fully parallelized FFTs. In principle we could use k-dependent diffusion coefficients but we have not investigated this in detail.

3.1.5 Boundary conditions

Poisson solvers are used in both the basic QuickPIC and the full QuickPIC. To get a unique solution from the Poisson solver, one has to specify a proper boundary condition. For the QuickPIC algorithm, the boundary condition has a more significant importance. This is because the potential ψ is solved for at each 2D slab. Therefore it is necessary to define a common reference point for the potential ψ. For a solution to the Poisson equation, if the area integral of the source term inside a circle is zero for a sufficiently large radius, then the potential drops off rapidly outside the circle. At a point far away from the circle, only the potential from the dipole and other higher order moments of the source inside the circle are left. The remnant fields become ignorable for large r. The potential, which is the integral of the field over r is therefore finite, and one can choose the potential to be zero at $r \to \infty$ as a common reference point for every slab. If the above condition is not satisfied, i.e., the net source term is not zero for ψ, then ψ drops off as $1/r$. An integral for ψ from $r = \infty$ will not converge. So seeking

a consistent definition of ψ is not possible for this case.

We will proceed to show the source terms for ψ in both basic QuickPIC and full QuickPIC are indeed local. This result comes from the continuity equation. For the basic QuickPIC model, plasma particles only have transverse motion. Therefore the continuity equation is

$$\frac{\partial \rho_p}{\partial \xi} + \nabla_\perp \cdot \mathbf{J}_{p\perp} = 0 \tag{3.29}$$

After integration over the transverse dimensions, Eq. (3.29) yields

$$\frac{\partial}{\partial \xi} \int \rho_p d\mathbf{r}^2 = 0, \tag{3.30}$$

where $d\mathbf{r}^2 = dx \times dy$ or $d\mathbf{r}^2 = r d\phi dr$.

There is no perturbation ahead of the beam, so the total charge is neutral,

$$\int \rho_p d\mathbf{r}^2|_{\xi=-\infty} = -\int \rho_{ion} d\mathbf{r}^2|_{\xi=-\infty}. \tag{3.31}$$

Therefore,

$$\int (\rho_p + \rho_{ion}) d\mathbf{r}^2 = 0. \tag{3.32}$$

In basic QuickPIC, $(\rho_p + \rho_{ion})$ is the source term for ψ. Hence ψ falls faster than $1/r$ outside the region of interest and can be set to zero at $r \to \infty$.

For the full QuickPIC model, the return current of plasma is retained. The continuity equation is,

$$\frac{\partial(\rho_p - J_{pz})}{\partial \xi} + \nabla_\perp \cdot \mathbf{J}_{p\perp} = 0. \tag{3.33}$$

Thus it can be shown that

$$\int (\rho_p + \rho_{ion} - J_{pz}) d\mathbf{r}^2 = 0. \tag{3.34}$$

The source term for ψ in the full quasi-static model is $(\rho_p + \rho_{ion} - J_{pz})$, in which the beam density and its longitudinal current cancel. Therefore we can also define $\psi = 0$ at $r \to \infty$ as a reference.

Although other potentials, such as $\phi, \mathbf{A}$, also satisfy the Poisson equation, the area integral of source term for them are not zero. For example, the contribution to ϕ from the charge of the beam cannot be ignored at the boundary. Therefore one can not find a reference point for ϕ and $\mathbf{A}$. However, the $\mathbf{E}$ and $\mathbf{B}$ fields, i.e., the derivative of the potentials ϕ and $\mathbf{A}$ not the potential themselves are of importance in the simulation. It is then possible to solve for ϕ and $\mathbf{A}$ using either periodic or conducting boundary condition since the $\mathbf{E}$ and $\mathbf{B}$ do not penetrate into the plasma beyond a few plasma skin depths due to the existence of the plasma return current and the charge density profile. It is further assumed that the fields outside a radius of a few plasma skin depths are zero, hence one can set $\psi = 0$ at the boundary instead of at $r \to \infty$. This is convenient for the simulation. Since the basic QuickPIC does not include the plasma return current, the drive beam can affect a larger volume of plasma, therefore one obtains a much larger value of ψ when integrating from the boundary. This is illustrated in Fig. 3.3.

3.1.6 Initialization and Quiet start

In the PWFA simulations, the evolution and many characteristics of the plasma wake field depend strongly on the charge distribution of the beam driver. For example, to study the wake excitation and energy transfer from the drive

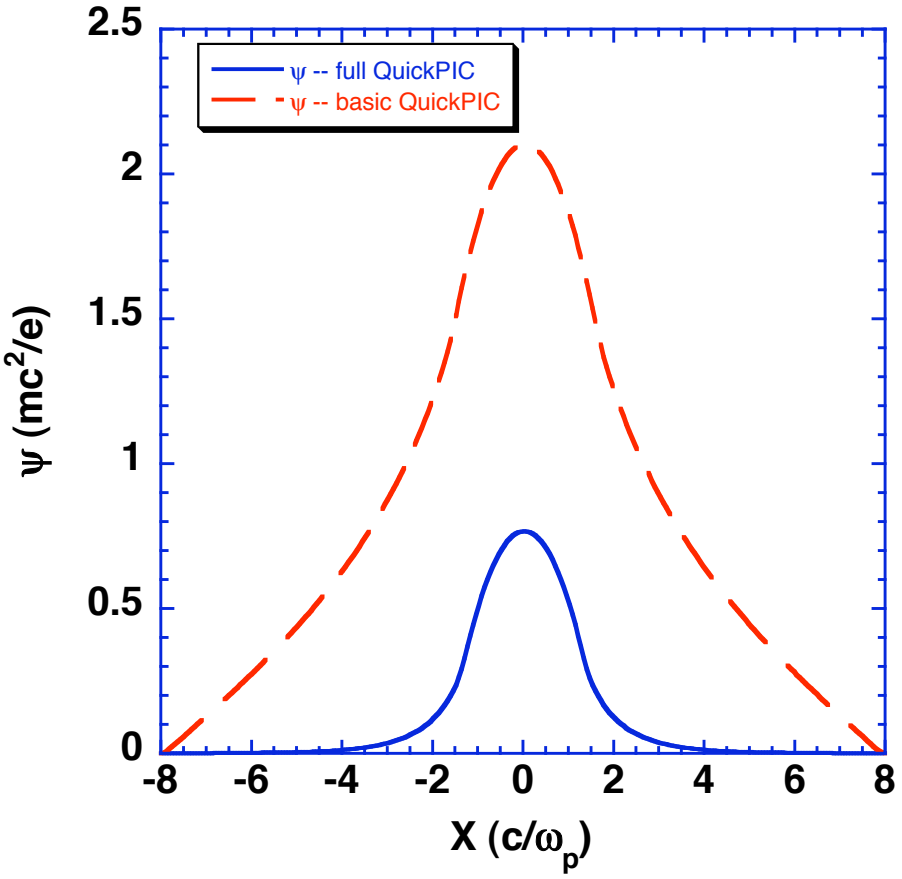

Figure 3.3: A transverse lineout of ψ in the full and basic QuickPIC simulations for the same parameters used in Chapter 4.

beam to the trailing beam in the "afterburner" scenario, both beams need to be properly shaped. Therefore it is desirable to have the ability to generate a beam with arbitrary shape. In some PIC codes such as OSIRIS, simulation particles are initialized with uniform separation, while each particle is assigned a charge which corresponds to the charge density at the position of the particle. Such initialization routines are simple in nature and work very well in the simulation for collisionless phenomena. However, in most PIC codes including QuickPIC, the charge of each simulation particle of a particular species is a fixed number. To initialize a given charge distribution of the beam, one has to place the particles with separations that are inversely proportional to the local charge density. For a density profile which is a separable function of coordinates, i.e., $n(x, y, z) = f(x)g(y)h(z)$, this can be done through the Newton method to find the position of the particle in each direction. This initialization routine is available in the UPIC framework, but it does not generalize to an arbitrary density profile. For nonseparable density profiles, the rejection-acceptance method first proposed by John von Neumann [78] is implemented into QuickPIC. The rejection-acceptance method basically serves as an non-uniform random generator for particle initialization.

The idea of the rejection method is quite simple. Suppose $p(x)$ is the desired probability distribution that we do not know how to generate and $q(x)$ is an auxiliary probability distribution we already know how to generate. Assuming that there exists a constant C that $p(x) < Cq(x)$ for any x, then it is possible to generate a random variable x that has probability distribution $p(x)$ through $q(x)$. The steps are outlined below,

1. Draw a sample x_i from $q(x)$, let $u_i = Cq(x_i)$.

2. Draw a sample y_i from uniform distribution $[0, u_i]$.

3. If $y_i \leq p(x_i)$, then accept x_i as a valid sample and go back to step 1.

4. If $y_i > p(x_i)$, then reject the sample and go back to step 1.

The above algorithm does not put requirements on the property of the desired probability distribution and can be easily generalized to a 3D distribution $p(x, y, z)$. It can be shown that the probability distribution of x_i is $p(x)$ and the efficiency of the method is greatly affected by the constant C. To achieve better efficiency, one has to find the smallest $C = C_{opt}$ that satisfies $p(x) < Cq(x)$. For simplicity, we use the uniform distribution as the auxiliary distribution function, and set $C = 1.2MAX(p(x))$. The non-uniform random number generator from the rejection method does not have a good statistical property, namely, it is noisy for PIC simulation. To study the transverse instability of the non-linear beam-plasma interaction under a controlled simulation, it is desirable to have a initial beam of zero average moment of the transverse position and momentum. This is also called a "quiet start" for PIC simulations. In QuickPIC, a "quiet start" is implemented by initializing simulation particle pairs, which have opposite transverse momentum and are placed symmetrically about the centroid of the beam. Although this method for "quiet start" is simple, we have observed in the simulations that a "quiet start" beam does not trigger the hosing instability up to thousands of timesteps.

3.1.7 Laser module

In this section, we describe the principle of modeling laser-plasma phenomena through the quasi-static approximation. A laser solver based on the quasi-static envelope equation was implemented by J. H. Cooley and T. M. Antonsen at the University of Maryland. The details for the numerics of the laser envelope

solver are described in the dissertation of J. H. Cooley but are summarized here for completeness on pages 88-94. The solver was combined into the QuickPIC framework and used as a separate module.

3.1.7.1 Envelope model

The set of quasi-static equations described earlier do not include the evolution of a laser pulse or its effect on the plasma particles. To include a laser pulse, the following modifications need to be made. First, an additional vector potential that generates the electric and magnetic fields of the laser pulse is added to Eq. (2.31). The laser pulse is described in terms of an envelope and a rapidly varying phase,

$$\frac{e\mathbf{A}}{m_e c^2} = Re\left[\hat{\mathbf{a}}(x, y, \xi, s)\exp\left(-ik_0\xi\right)\right], \tag{3.35}$$

where $k_0 = \omega_0/c$ is the central wave number of the laser pulse corresponding to a frequency ω_0 and the hat denotes normalized quantities. The envelope satisfies an augmented paraxial wave equation that is derived from Eq. (2.31).

$$2\frac{\partial}{\partial s}\left(-ik_0 + \frac{\partial}{\partial \xi}\right)\hat{\mathbf{a}} - \nabla_\perp^2\hat{\mathbf{a}} = \frac{4\pi e}{m_e c^3}\hat{\mathbf{J}} = k_0^2\chi_p\hat{\mathbf{a}} \tag{3.36}$$

The mixed derivative term is needed to describe group velocity reduction due to the plasma, the direct forward Raman scattering and the self-modulational instability [79]. The high frequency current is expressed in terms of a product of a susceptibility χ_p and the laser vector potential. The relative dielectric constant is thus, $\epsilon = 1 + \chi_p$. The plasma contribution to the susceptibility is calculated using the following deposition scheme,

$$\chi_p = -\left\langle \frac{\omega_p^2}{\omega_0^2 \gamma_p} \right\rangle = -\frac{4\pi e^2}{m_e \omega_0^2} \frac{1}{Volume} \sum \frac{1}{\bar{\gamma}_p (1 - V_{pz}/c)} \tag{3.37}$$

As shown by Mora and Antonsen [63] the laser period-averaged relativistic gamma factor is modified when the laser's vector potential is included,

$$\bar{\gamma}_p = \left[1 + P_p^2/(m_e c)^2 + |\hat{\mathbf{a}}|^2/2\right]^{1/2}. \tag{3.38}$$

The plasma particles are now influenced by the ponderomotive force of the laser, which is included in the equation of motion as

$$\frac{d\mathbf{P}_{p\perp}}{d\xi} = \frac{q_p}{c - V_{pz}} \left[\mathbf{E}_\perp + (\frac{\mathbf{V}_p}{c} \times \mathbf{B})_\perp - \frac{m_e c^2}{\bar{\gamma}_p} \nabla_\perp \frac{|\hat{\mathbf{a}}|^2}{4} \right]. \tag{3.39}$$

3.1.7.2 Implementation

If there is a laser driver, the QuickPIC algorithm introduced previously only needs to be modified in three places. In the momentum advance, the ponderomotive force needs to be included in Eq. (3.1), i.e.,

$$\frac{d\mathbf{u}_{p\perp}}{d\xi} = \frac{q_{eff}}{m_e} [\gamma_p \mathbf{E}_\perp - \frac{m_e c^2}{q_p} \nabla_\perp \frac{|\hat{\mathbf{a}}|^2}{4} + (\frac{\mathbf{u}_p}{c} \times \mathbf{B})_\perp] \tag{3.40}$$

so that the effective electric field in the non-relativistic Boris pusher is now

$$\gamma_p \mathbf{E}_\perp - \frac{m_e c^2}{q_p} \nabla_\perp \frac{|\hat{\mathbf{a}}|^2}{4} \tag{3.41}$$

In addition, the expression for γ_p is now

$$\gamma_p = \frac{1 + \mathbf{u}_{p\perp}^2/c^2 + |\hat{\mathbf{a}}|^2/2 + (1 - q_p \psi/m_e c^2)^2}{2(1 - q_{pi} \psi/m_e c^2)}. \tag{3.42}$$

Values of the ponderomotive potential are needed on the half integer grid $\xi = (m + 1/2)\Delta\xi$ for $\mathbf{x}_\perp$ and are calculated according to

$$\left[|\hat{\mathbf{a}}|^2/2\right]^{m+1/2} = \frac{1}{2}\left\{\left[|\hat{\mathbf{a}}|^2/2\right]^{m+1} + \left[|\hat{\mathbf{a}}|^2/2\right]^{m}\right\}. \tag{3.43}$$

Last, we need to deposit the new quantity χ_p, which is the plasma susceptibility,

$$\begin{aligned} \chi_p &= -\frac{4\pi}{m_e\omega_0^2 \cdot Volume}\sum_i \frac{q_{pi}^2}{(1 - V_{pzi}/c)\gamma_{pi}} \\ &= -\frac{4\pi}{m_e\omega_0^2 \cdot Volume}\sum_i \frac{q_{pi}^2}{1 - q_{pi}\psi/m_e c^2}. \end{aligned} \tag{3.44}$$

The propagation of the laser pulse is described by Eq. (3.36) for the evolution of the envelope $\hat{\mathbf{a}}$ of the normalized vector potential. This equation applies to the case of pulse propagation in a fully ionized plasma; that is, it is assumed that there is no other matter in the form of neutral or partially ionized gas present that would modify the dispersion relation for the laser light. To make the equations more general we imagine that there is also a tenuous background medium present, characterized by a small correction to the dielectric constant $\delta\epsilon(\omega)$ that modifies the group velocity and adds dispersion. In this case Eq. (3.36) becomes,

$$2\frac{\partial}{\partial s}\left(-ik_0 + \frac{\partial}{\partial\xi}\right)\hat{\mathbf{a}} - ik_0\beta_1\frac{\partial}{\partial\xi}\hat{\mathbf{a}} + \beta_2\frac{\partial^2}{\partial\xi^2}\hat{\mathbf{a}} - \nabla_\perp^2\hat{\mathbf{a}} = k_0^2\chi_T\hat{\mathbf{a}}, \tag{3.45}$$

where $\beta_1 = 2(v_f - v_g)/c$, v_f is the frame velocity $\xi = v_f t - z$, (now assumed to be different from the speed of light) and

$$v_g \cong c\left[1 - \frac{1}{2}\frac{d(\omega\delta\varepsilon)}{d\omega}\right]_{\omega_0}, \tag{3.46}$$

is the group velocity in the background medium in the limit in which the medium is tenuous. The coefficient of dispersion is given by

$$\beta_2 = \frac{v_f^2 - v_g^2}{c^2} + \omega \frac{d}{d\omega}\left(\frac{v_g}{c}\right)\bigg|_{\omega_0}. \tag{3.47}$$

The quantity $\chi_T = \chi_p + 2n_2 I$ represents the modified susceptibility including the plasma contribution and the nonlinear susceptibility of the background medium. Here I is the local intensity and n_2 the second order coefficient of nonlinearity in the susceptibility of the background medium. The linear portions of the background susceptibility are described by $\delta\epsilon$ and contribute to the coefficients β_1 and β_2. The coefficient β_1 can be set to zero by picking the frame velocity to equal the group velocity of the background medium. If no background medium is present, then the frame velocity should equal the speed of light. The plasma reduction of the group velocity is captured in Eq. (3.45) due to the interplay of the mixed, second order $s-\xi$ derivative and the plasma contribution to the total susceptibility. Likewise, the reduction of the group velocity for waves propagating obliquely to the z-axis is captured by the interplay of the mixed derivative and the transverse Laplacian. Retention of the mixed derivative term also leads to separate conservation laws for wave energy and wave action [63]. This allows for a correct treatment of pulse depletion due to the excitation of plasma waves.

We wish to find a stable numerical approach to solve Eq. (3.45) in a fully three-dimensional simulation. In addition to the computational cost associated with solving a three-dimensional non-linear partial differential equation, we have the added complication of performing this calculation on a parallel computer system. To this end, we include the constraint that our computational algorithms have an efficient parallel implementation. We note that the wave operator involves differentiation with respect to all three space-like coordinates. This will

make finding an s-centered fully implicit numerical implementation of Eq. (3.45) difficult. Instead we will use a split step algorithm [80] in which Eq. (3.45) is separated into two operators each of which can be advanced in an s-centered implicit way. Specifically, we separate Eq. (3.45) into separate equations involving the two operators L_0 and L_1,

$$2\frac{\partial}{\partial s}\left(-ik_0+\frac{\partial}{\partial \xi}\right)\hat{\mathbf{a}}=L_0(\hat{\mathbf{a}})\equiv i\frac{k_0\beta_1}{2}\frac{\partial}{\partial \xi}\hat{\mathbf{a}}-\frac{\beta_2}{2}\frac{\partial^2}{\partial \xi^2}\hat{\mathbf{a}}+k_0^2\chi_T(\mathbf{x}_\perp,\xi,s)\hat{\mathbf{a}}, \quad (3.48)$$

and

$$2\frac{\partial}{\partial s}\left(-ik_0+\frac{\partial}{\partial \xi}\right)\hat{\mathbf{a}}=L_1(\hat{\mathbf{a}})\equiv i\frac{k_0\beta_1}{2}\frac{\partial}{\partial \xi}\hat{\mathbf{a}}-\frac{\beta_2}{2}\frac{\partial^2}{\partial \xi^2}\hat{\mathbf{a}}+\nabla_\perp^2\hat{\mathbf{a}}. \quad (3.49)$$

Here we have assumed that the coefficients β_1 and β_2 are independent of transverse coordinate and we have included half of their effect in each operator. If these coefficients were spatially varying we would include their full effect in Eq. (3.48) and eliminate them from Eq. (3.49). The separation is made so that Eq. (3.48) can be solved in ξ with $\mathbf{x}_\perp$ as a parameter, and Eq. (3.49) can also be solved in ξ by Fourier transforming in $\mathbf{x}_\perp$ and treating $k_\perp$ as a parameter. It is necessary to include the mixed derivative on the left hand side in both steps so that the interplay between the mixed derivative and the susceptibility in the case of Eq. (3.48) and the mixed derivative and the transverse Laplacian in the case of Eq. (3.49) that gives rise to the reduction of the group velocity due to plasma and oblique propagation is recovered.

The sequence in which Eqs. (3.48) and (3.49) are solved is illustrated in Fig. 3.4. The top portion of this figure illustrates the part of the code that solves for the laser field, while the bottom portion illustrates the part that evolves

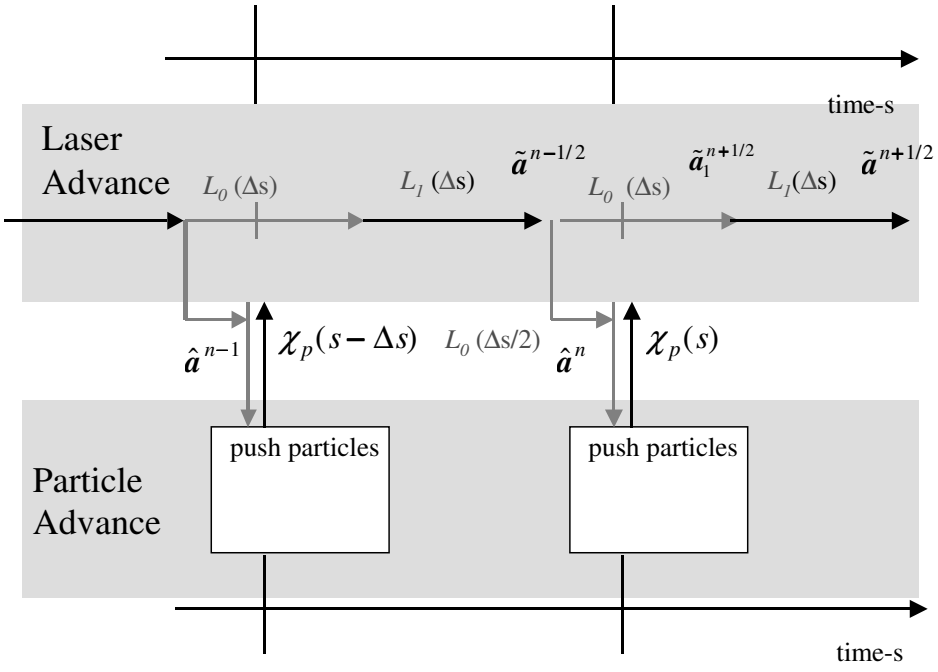

Figure 3.4: Schematic representation of second order accurate split step algorithm for advancing the laser field in s. Also shown is the communication between the laser propagation part of the code and the particle and wake part of the code.

the particles and calculates the plasma wake as described in the previous section. The communication between the two parts of the code is illustrated by the arrows connecting the upper and lower portions of the figure. The laser propagation part of the code must supply the normalized vector potential (actually, its magnitude squared $|\hat{\mathbf{a}}|^2$) evaluated on the s-grid, $s_n = n\Delta s$, to the particle part; while the particle part must supply the susceptibility χ_T on the s-grid to the laser propagation part of the code. Given that the susceptibility χ_T is known on the s-grid, Eq. (3.48) is centered about $s_n = n\Delta s$. The finite difference in s version of Eq. (3.48) is thus written as,

$$2\left(-ik_0 + \frac{\partial}{\partial\xi}\right)\frac{\tilde{\mathbf{a}}_1^{n+1/2} - \tilde{\mathbf{a}}^{n-1/2}}{\Delta s} = \frac{1}{2}L_0(\tilde{\mathbf{a}}_1^{n+1/2} + \tilde{\mathbf{a}}^{n-1/2}). \tag{3.50}$$

where $\tilde{\mathbf{a}}^{n-1/2}$ and $\tilde{\mathbf{a}}_\mathbf{1}^{n+1/2}$ are intermediate values of the normalized vector potential that are illustrated in Fig. 3.4. The operater L_0 contains the time and spatially dependent susceptibility evaluated at s_n. This depends on the vector potential at this same time, and this will have to be determined from $\tilde{\mathbf{a}}^{n-1/2}$. We will discuss this point subsequently. In between applications of operator L_0 we must apply operator L_1, which includes the transverse derivatives. This will connect values of the intermediate quantities $\tilde{\mathbf{a}}^{n+1/2}$ and $\tilde{\mathbf{a}}_\mathbf{1}^{n+1/2}$ as indicated on Fig. 3.4,

$$2\left(-ik_0 + \frac{\partial}{\partial\xi}\right)\frac{\tilde{\mathbf{a}}^{n+1/2} - \tilde{\mathbf{a}}_1^{n+1/2}}{\Delta s} = \frac{1}{2}L_1(\tilde{\mathbf{a}}^{n+1/2} + \tilde{\mathbf{a}}_1^{n+1/2}). \tag{3.51}$$

In the operator L_1 the coefficients are assumed to be independent of $\mathbf{x}_\perp$. Thus Eq. (3.51) is solved in Fourier space, and periodic boundary conditions in the two transverse directions are applied.

Both operators L_0 and L_1 are second order with respect to differentiation by ξ.

These operators are then represented as second order finite difference equations. Both equations are thus equivalent to tridiagonal matrices, which are solved by the dual sweep algorithm [81]. The issue of boundary conditions is complicated by the addition of the dispersion coefficient β_2. Dispersion allows that information can propagate both faster and slower than the frame velocity. Thus, information can propagate to both large and small values of ξ. Rather than attempt to impose an absorbing boundary condition at the minimum and maximum values of ξ, we simply require that the vector potential vanish at these points and further require that the simulation domain be large enough such that no reflection of waves from these points can occur. We note that in the case in which dispersion is absent, then information can only propagate in the direction of increasing ξ. In this case the required boundary condition is that all values of $\hat{\mathbf{a}}(\xi)$ for ξ less then the minimum value in the simulation domain must vanish.

The split step algorithm just described gives a second order in Δs accurate solution for the wave equation provided a second order accurate value of the susceptibility is in the operator L_0 in Eq. (3.50). The required susceptibility is evaluated on the s-grid, while the intermediate quantities determined in (3.50) and (3.51) are known on the half grid. To evaluate the vector potential at the required time we apply a half time step advancement of the operator L_0 to generate $\hat{\mathbf{a}}^n$ on the grid $n\Delta s$ starting from the intermediate value $\tilde{\mathbf{a}}_{n-1/2}$,

$$2\left(-ik_0+\frac{\partial}{\partial\xi}\right)\frac{\hat{\mathbf{a}}^n-\tilde{\mathbf{a}}^{n-1/2}}{\Delta s/2}=\frac{1}{2}L_0(\hat{\mathbf{a}}^n+\tilde{\mathbf{a}}^{n-1/2}). \tag{3.52}$$

Since $\tilde{\mathbf{a}}_{n-1/2}$ is already second order accurate, and we are only advancing s by a fraction of a grid spacing we can use a first order evaluation of the susceptibility in L_0 for this step. Typically, we extrapolate the susceptibility from the two previous s-steps for this estimate. Thus, to advance the laser field, only one call

to the part of the code that advances the particles is needed per s-step.

Equations (3.50) and (3.51) involve only finite differencing in the axial grid, thus each transverse location or wavenumber can be solved independently. This separation motivates the parallel implementation used to solve this system. The normal layout of the field involves each node having all axial data and all the data for one transverse coordinate. The second transverse coordinate is divided among the different processors. This layout allows the evolution of Eqs. (3.50) and (3.51) to be local to a processor. Unfortunately this layout requires two large communications to perform the transverse FFT necessary to evolve Eq. (3.51). We take an FFT in the coordinate that is local to the processors then redistribute the data so the other transverse coordinate is local. We can then perform the second FFT in this direction and then solve Eq. (3.51). Finally we reverse the process leaving the data in the original layout.

3.2 PIC framework

The full QuickPIC code is built from the UCLA Parallel Particle-in-Cell (UPIC) Framework [82] and the laser solver module described in the previous section. The UPIC Framework provides trusted components for the rapid construction of new, parallel Particle-in-Cell codes, using object-oriented ideas. It is designed in layers. The lowest layer consists of highly optimized Fortran77 routines from 25 year legacy of PIC codes. The upper layers are written in Fortran95. The middle layer primarily provides a much safer and simpler interface to the complex Fortran77 legacy subroutines by encapsulating many details, such as data layouts on parallel machines. The upper layer consists of powerful high level classes that enable the reuse of large blocks of code. The Framework also provides several sample main codes.

The QuickPIC code is a fusion of a 3D and a 2D parallel PIC code. The 3D code contains the beam particles and treats the 2D code as a transverse field solver, where it passes the beam density as input, and obtains the electric and magnetic fields as output. The Framework uses the GCPIC algorithm for domain decomposition [83], but with different decompositions. The 3D Framework distributes the ξ coordinate across different processors, while the 2D Framework distributes the y coordinate and treats the ξ coordinate as a time. Therefore the 3D code transposes the beam density which has dimensions (nx, ny, nz) from the form $f(nx, ny, nz/nproc)$ to the form $f(nx, ny/nproc, nz)$, where $nproc$ is the number of processors, before it calls the 2D code, and transposes the potentials back to the original form after the 2D code returns.

The 2D Framework distributes the y coordinate across processors, but the number of grids per processor can vary. This allows one to keep the number of particles per processor approximately constant by adjusting the sizes of the domains, and thus permits load balancing of the calculation. The Framework is spectral and uses FFTs to solve the fields. However, in addition to periodic boundary conditions, conducting boundary conditions are also supported, using various combinations of sine and cosine transforms.

The Framework provides many of the functions that QuickPIC uses, such as solvers for the potentials, management of guard cells, FFTs, and a particle manager which ensures particles are in the correct domain. To make such functions easy and safe to use, classes have been defined to hide the implementation details of complicated data structures. To illustrate the importance of this, the conducting boundary potential solver doubles the size of the grid in each dimension and creates image charges before the FFT is called. The data in Fourier space is transposed and has a different domain decomposition than in real space. All

these details are hidden from the user who uses this solver.

In addition to the components provided by the UPIC Framework, some special functions had to be custom written for QuickPIC, usually using a function provided in the Framework as a starting point. For example, both the particle push and charge deposit subroutines were modified. The new functions were placed in their own modules, but also had available functions in the original modules, so that the relationship was similar to that of inheritance in object-oriented languages. This kind of structure allows QuickPIC to make use of upgrades to the UPIC Framework with relatively little modification.

3.3 Parallelization

QuickPIC is fully parallelized in both 3D and 2D. The parallelization is implemented using the MPI communication library. As mentioned in the previous section, the domain decomposition of the 3D beam part is along z, this is illustrated in Fig. 3.5 for a 4-node configuration. Each node initializes $1/4th$ of the drive beam and stores its information. For every time step, each node will update the portion of drive beam which belongs to it and exchange particles that move out of its domain. Since the domain is moving at the speed of light, particles can only move from right to left, therefore the communication is one-directional although the particle manager in the framework can handle two-directional communication. The particle manager can move particles to the correct domain even if they jump across multiple domains, but in a real simulation this is usually impossible because of the long dephasing length of high energy particles.

The 2D code is localized in the y direction and has a different communication pattern from the 3D code. Fig. 3.6 shows the 2D domain decomposition and

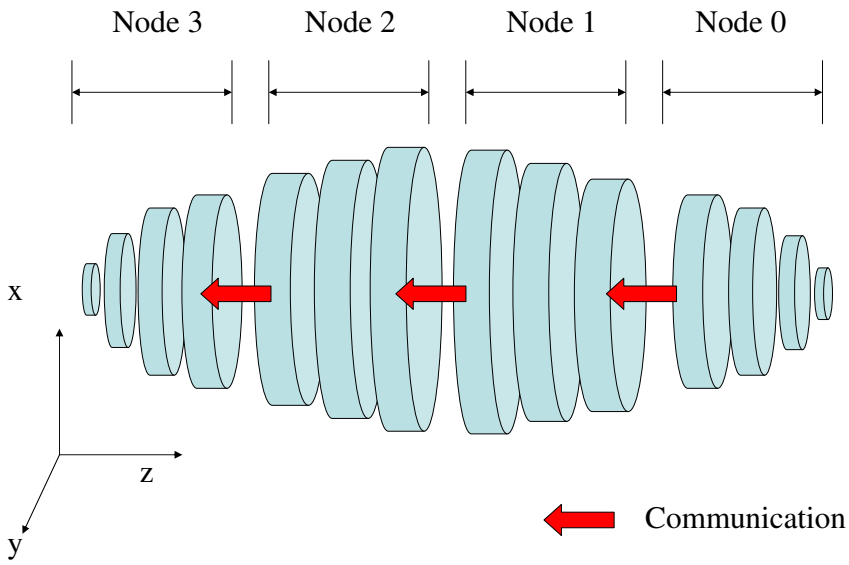

Figure 3.5: The drive beam can be viewed as a series of slices of width $\Delta\xi$ distributed on different nodes.

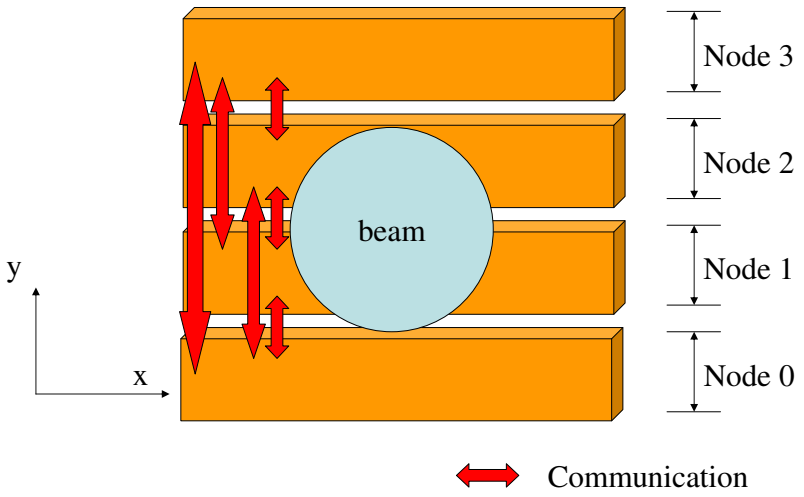

Figure 3.6: The plasma is distributed in y. The communications happen between any two nodes.

communication pattern for the same 4-node configuration. The 2D code solves for the plasma response for each transverse slice in the Fourier space. The multidimensional FFT routine in the framework requires a data transpose for each dimension. The data transpose involves global, one-to-one communications. Due to the large amount of operations in the Fourier space, the transpose routine becomes a bottle neck for parallel simulation.

QuickPIC has been ported to several platforms, including Mac OS X, IBM AIX and Linux. Most simulations are done on two parallel computers, SEABORG at National Energy Research Scientific Computing Center (NERSC) and DAWSON in our plasma simulation group. SEABORG is a 6,656-processor IBM

RS/6000 SP supercomputer with 10 teraflop/s peak performance. There are 380 compute nodes, each node has 16 processors. They are connected by a high-bandwidth, low-latency switching network. DAWSON is a 512-processor Mac G5 cluster with 4.4 teraflop/s peak performance. There are 256 compute nodes and each node has 2 processors. Gigabit ethernet is used which provides a low-cost high performance network for the cluster.

We have run QuickPIC simulations as large as $2048 \times 2048 \times 512$ grids but for our parameter scan we use the "typical" size. For a typical QuickPIC simulation, $256 \times 256 \times 256$ grids are used in 3D and 256×256 grids in 2D. 4 particles per cell is also commonly used for the plasma. Since there is no field solver in the 3D code, the 3D calculation only takes a small fraction of the total time. Most of the time is spent in solving the plasma response for each slice. The execution time for this kind of simulations scales well up to 32 processors on the IBM SP at NERSC. However, it currently scales well to only 8 processors on the DAWSON G5 cluster due to network overhead. The results of the timing benchmarks are shown in Fig. 3.7 to show the performance of the 2D loop on these two platforms. The timing data was taken for different configurations of the nodes. "Same nodes" means we use as many CPUs as possible for each node; for NERSC, each node consists of 16 CPUs; for DAWSON, this number is 2. "Diff nodes" means that we only use one CPU for each node. The different timing for DAWSON for these two configurations shows there is some disadvantage to running the 2 CPUs each node. This may be due to the competition for resources for the 2 CPUs. For DAWSON, the difference caused by resource competition is greater than the difference between inner-node and inter-node communications; therefore running on 2 CPUs on each node is slower than running on 1 CPU for each node. However the situation on NERSC is different. The resource competition is minimal and the simulation on the same node is a little bit faster than on different nodes since

the inner-node communication is more efficient.

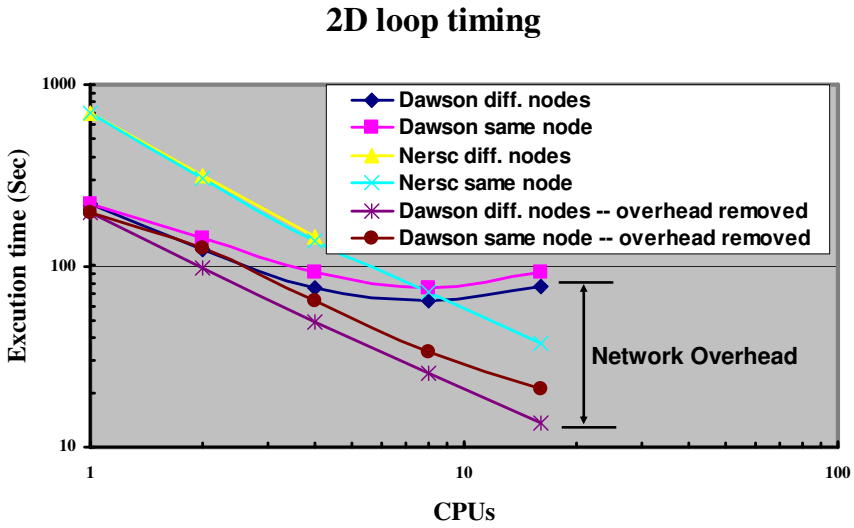

Figure 3.7: Timing of the 2D loop on two different platforms, i.e, NERSC with high speed network and DAWSON with gigabit ethernet.

Another important observation is the network overhead caused by the slower network on DAWSON. As more CPUs are used, we see super-linear acceleration of the performance on NERSC due to its excellent network; while on DAWSON the timing curve rolls over near 8 CPUs which is not surprising because slower network is employed. To understand this better, we use a simple model for PIC code timing,

$$t_{total} = N_p * t_p + N_g * t_g + Overhead \tag{3.53}$$

In Eq. (3.53), N_p is the number of particles and N_g is the number of grids.

And t_p is the time for each particle update and t_g is the time for each field update. These two are nearly constant for different simulations on a given machine. By varying N_p and N_g in the simulation, we are able to deduce the overhead of the 2D loop for the DAWSON platform. The result is shown in Fig. 3.8.

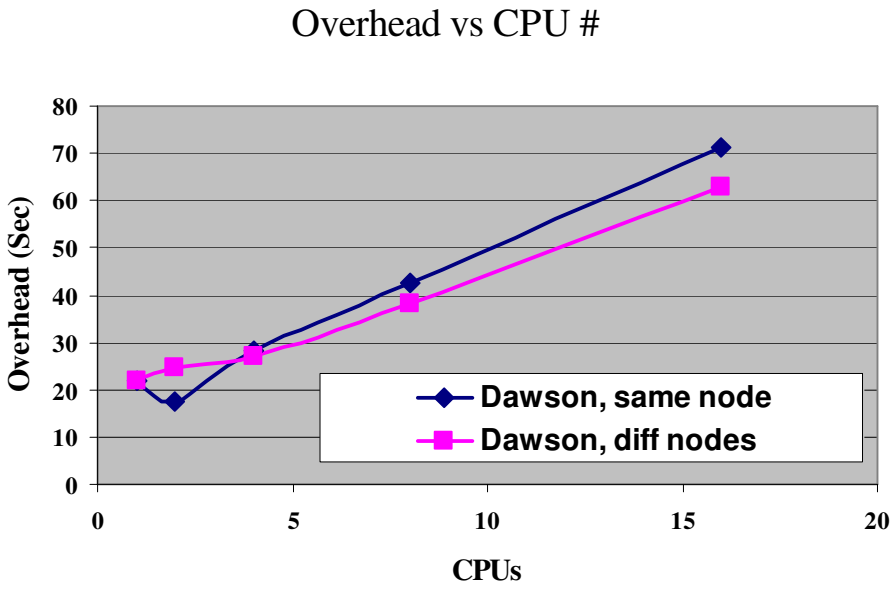

Figure 3.8: The relation between the overhead and the number of CPUs in the timing benchmarks on DAWSON cluster.

The overhead is most possibly caused by the latency of MPI calls on the gigabit ethernet hardware. A estimate of the total latency for all the data transpose calls in QuickPIC gives a number on the order of the overhead observed. Furthermore the overhead is observed to grow linearly with the number of CPUs. This is consistent with the global, one-to-one communication pattern in QuickPIC. Since each CPU needs to communicate with all other CPUs, therefore the overall

latency scales with the number of CPUs.

Figs. 3.7 and 3.8 clearly show that QuickPIC is latency limited on the DAWSON cluster. This makes QuickPIC simulations inefficient on more than 16 CPUs. One possible solution is to restructure the FFT calls and combine transposes for a larger amount of data.

Another technique which we refer to as "software pipelining" is also possible for dramatically improving the parallel efficiency of QuickPIC. This is briefly explained here. In QuickPIC, the 2D code views ξ as a time variable so the calculation is sequential in ξ, and because the speed of the moving window is c, no information is passed backward in ξ in the 3D code where ξ is treated as a spatial variable. This feature allows QuickPIC to use software pipelining to achieve greater parallelism. Using this technique multiple copies of the code can be started simultaneously with each copy working on different parts in ξ of the beam and passing the results to the one working on the adjacent part. This is analogous to the instruction-level pipelining technique used in modern CPU design where speed-up is achieved by adding more execution units to the work flow. If the number of copies used is N, the code speeds up and scales by approximately N times over its current speed. For typical QuickPIC runs, N can be as large as 128. Since the code currently scales to 32 processors, it would be possible with software pipelining to run efficiently on as many as 4096 processors.

3.4 Performance

In this section, we provide an estimate of the CPU savings for the QuickPIC algorithm versus a full PIC algorithm such as OSIRIS. We start with considerations for a beam driver. We assume both types of algorithms use a "moving"

3D window of length L_z composed of $N_x \times N_y \times N_z$ grids and the number of particles per cell, N_p, is the same. It is instructive to calculate the total number of particle pushes. Suppose one wants to calculate the wake from an identical beam. In a full PIC code the beam starts outside the plasma and then must propagate through the box in the z direction. This requires N_z timesteps times a factor of $K_c = \Delta z/(c\Delta t)$ due to the Courant condition ($K_c = 3^{1/2}$ assuming cells are the same size in each direction). So the number of particle pushes is $N_x \times N_y \times N_z \times N_p \times N_z \times \sqrt{3}$ (it is really a factor of ~ 2 less since not all of the box is filled with particles at the beginning). On the other hand, using QuickPIC, we only need to go through the 2D part of the code once. The number of 2D particle pushes is $N_x \times N_y \times N_p \times N_z$ where the N_z factor is the number of 2D time steps. Therefore, assuming N_p is the same there is a savings of $N_z \times \sqrt{3}$ in particle pushes. For example, if $N_z = 256$, this is a factor of ~ 450.

There is additional savings that comes from taking large 3D steps in s after the initial wake is obtained. Suppose one wants to propagate a beam through one betatron oscillation into the plasma, $\lambda_\beta \equiv 2\pi k_\beta^{-1} = 2\pi\sqrt{2\gamma}\frac{c}{\omega_p}$. Using a full PIC code to simulate one betatron wavelength, a total of $(\lambda_\beta/L_z)N_z \times K_c$ updates are required. This gives $N_x \times N_y \times N_z \times N_p \times \lambda_\beta \times (N_z/L_z) \times K_c$ particle pushes. The factor N_z/L_z is the cell size in z. On the other hand, using QuickPIC requires only $N_x \times N_y \times N_p \times N_z \times K_\beta$ particle pushes where K_β is the number of steps needed to resolve one wavelength. We typically use $K_\beta = 20 - 30$. Therefore, when modeling the propagation of a beam through a fixed distance (here one λ_β), there is a savings of $(\lambda_\beta \times N_z \times K_c)/(L_z \times K_\beta)$. For $N_z \sim 256$, $K_c \sim \sqrt{3}$, $L_z \sim 2.5\lambda_p$, $K_\beta \sim 20$ and $\gamma_b \sim 10^5$, $\lambda_\beta N_z K_c/(K_\beta L_z) \sim \sqrt{2\gamma_b} N_z K_c/K_\beta \sim 1000$. However, the number of particle pushes is not the only issue. The QuickPIC loop is less efficient than a full PIC loop because each 2D update has $2 - 4$ iterations and the field solve involves numerous FFTs. We find from detailed timings that

the actual speed-up is between $100 \sim 1000$.

For a laser driver, the cell size in z is typically much smaller in a full PIC simulation, so the savings can be considerably higher. When modeling a beam driver the cell size in z is $\sim .05c/\omega_p$, while when modeling a laser driver the cell size must be $<\approx .25c/\omega_0$. Therefore, the savings is typically $[\omega_0/5\omega_p]^2$ times larger when modeling a laser driver. This factor is proportional to the ratio of the cell size squared because there are $\omega_0/5\omega_p$ times more particles and $\omega_0/5\omega_p$ times more time steps.

The above discussion raises the possibility of running a full PIC code to calculate the wake and then using the wake to advance beam particles a large distance forward in z and then repeating this loop. This super cycling approach where beam and plasma particles are pushed with different time steps has been successfully implemented in OSIRIS [84]. This would be advantageous over a full PIC code when the distance of the beam advance is larger than the window size. This would still be a factor of $N_z K_c$ less efficient than a quasi-static code but it could be useful in some cases.

3.5 Summary

In this chapter, we have described in detail the algorithm and structure of a new fully 3D, fully parallelized quasi-static PIC code called QuickPIC. We described the full quasi-static equations and showed how to implement them into a PIC code structure by combining a 2D plasma PIC code (plasma push, deposition and field solver) and a 3D PIC code (beam push) to advance the beam. Modifications to the charge and current depositions, particle push, and field solve routines were described in detail. Because of the quasi-static approximation, the

field solve and particle push are no longer time centered and an iteration loop is needed. The detail implementation of the iteration loop was also described. Several methods of initialization are available in QuickPIC including one to generate arbitrary beam shapes based on a non-uniform random number generator. QuickPIC is fully parallelized using MPI and is capable of simulating PWFA and LWFA problems with at least a factor of 100 savings in CPU needs as compared to the fully explicit electromagnetic PIC code OSIRIS. Although not described here, dynamic load balancing [82] as well as a field ionization package [85] have also been added. A future improvement, i.e., "software pipelining" was also discussed in section 3.3.

CHAPTER 4

Benchmarking QuickPIC

In this chapter, we present the result of benchmarks of QuickPIC against a 3D fully electromagnetic code OSIRIS. The greatest challenge is correctly computing the wakes for given driver shapes. Once the wake is accurately computed then the accuracy of the advance of the beam particles or laser is not an issue. Therefore, the benchmarks to be presented are on the calculation of the wake for electron, positron, and laser beams. In each case, we assume the beam is azimuthally symmetric and it does not have any head to tail misalignment, i.e., there is no tilt. We have benchmarked QuickPIC against OSIRIS for beams with asymmetric spot sizes and tilts and the agreement is within the same accuracy as those for the symmetric cases.

4.1 Benchmark for an electron beam driver

The first benchmark is done for an electron beam driver, for which we are mostly interested in the focusing force on the beam and the longitudinal wakefield. The electron beam has a bi-Gaussian density profile in both the transverse and longitudinal directions, $n_b = \frac{N}{(2\pi)^{3/2}\sigma_r^2\sigma_z} e^{-(x^2+y^2)/2\sigma_r^2} e^{-\xi^2/2\sigma_z^2}$. The spotsizes are $\sigma_r = 7\mu m$ and $\sigma_z = 45\mu m$, the emittances are $\epsilon_x = \epsilon_y = 15mm \cdot mrad$, and the total number of electrons in the beam is $N = 1.8 \times 10^{10}$. The beam is ultra-relativistic with $\gamma = 55800$. The plasma density is $n_0 = 2.0 \times 10^{16} cm^{-3}$, which

corresponds to a plasma skin depth of $c/\omega_p = 37.5\mu m$. $k_p\sigma_r = 0.19 << 1$, so the beam is considered narrow and the benchmark results should depend weakly on σ_r. The peak beam density is much higher than the background plasma density, $n_b/n_0 = 25.9$, thus the beam-plasma interaction is in the highly non-linear blow-out regime and as we show the assumptions of Whittum fail [18]. The 3D OSIRIS and QuickPIC simulations are carried out in moving windows with a box size $16c/\omega_p \times 16c/\omega_p \times 13.35c/\omega_p$ and conducting boundaries in the transverse directions. The plasma provides strong screening of the driver's fields. So, although the electric and magnetic fields of the beam are huge in its vicinity, they do not penetrate into the plasma beyond a few c/ω_p. The transverse box size is chosen to be large enough so that at the boundaries all fields go to zero, thus the boundaries play little role here. The simulations use $256 \times 256 \times 256$ cells; the spatial resolution is $0.0625c/\omega_p$ for the transverse direction and $0.052c/\omega_p$ for the longitudinal direction. For the OSIRIS simulation, the time step is chosen to be $0.025c/\omega_p$ to satisfy the Courant condition. During the simulation the beam has propagated $20c/\omega_p$ into the plasma. The beam is stiff due to its large Lorentz factor; its shape almost does not evolve in this short distance. So the quasi-static approximation should be well satisfied.

Shown in Fig. 4.1 are the longitudinal wakefields from QuickPIC and OSIRIS simulations. Results from QuickPIC simulations with 2 and 4 iterations are both shown and they differ slightly from each other and from the OSIRIS result only at the back of the wake field structure. The agreement is improved with more iterations. However the simulations with 2 iterations already gives very satisfactory results even in this highly non-linear case. The discrepancy at the positive spike is caused by the fact that the charge and current deposition schemes diverge for plasma particles with $V_{pz} \sim c$, therefore, a smaller 2D step $\Delta\xi$ is required to make the deposition schemes more accurate.

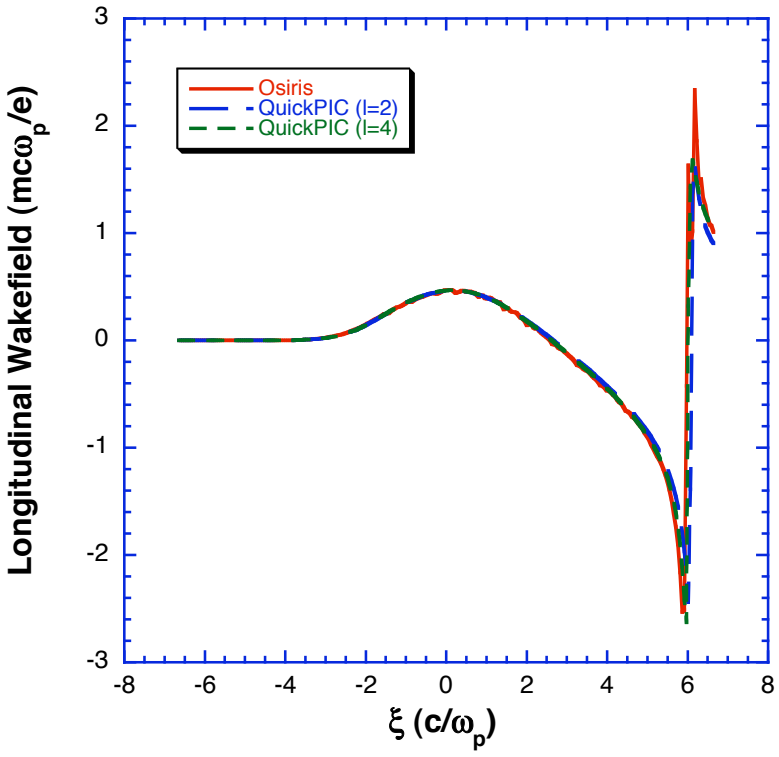

Figure 4.1: Longitudinal wakefields in QuickPIC and OSIRIS simulations for an electron drive beam. Both 2 iterations(l=2) and 4 iterations(l=4) are used for the QuickPIC simulations. The driver moves from right to left in this plot.

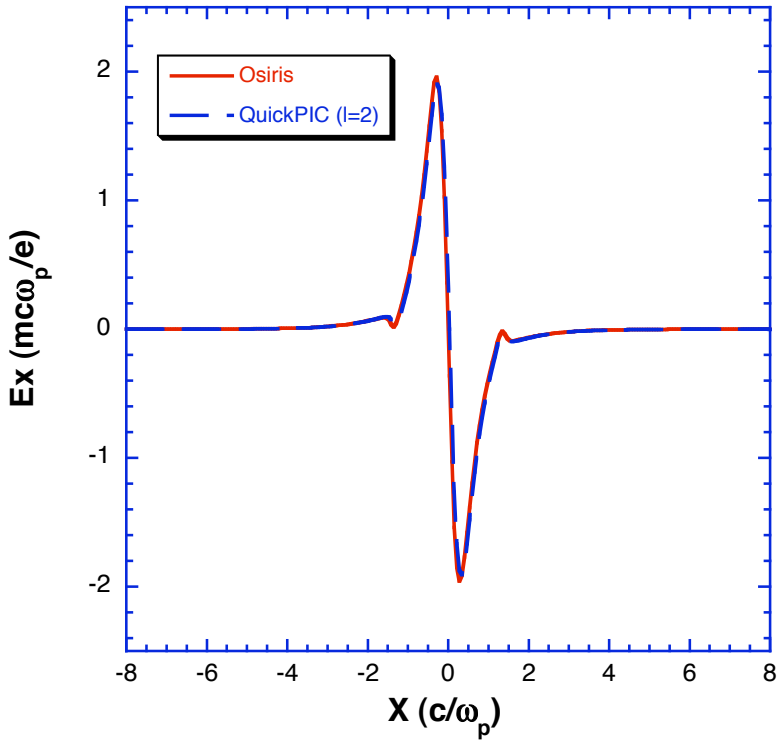

Figure 4.2: Radial electric field comparison for electron drive beam.

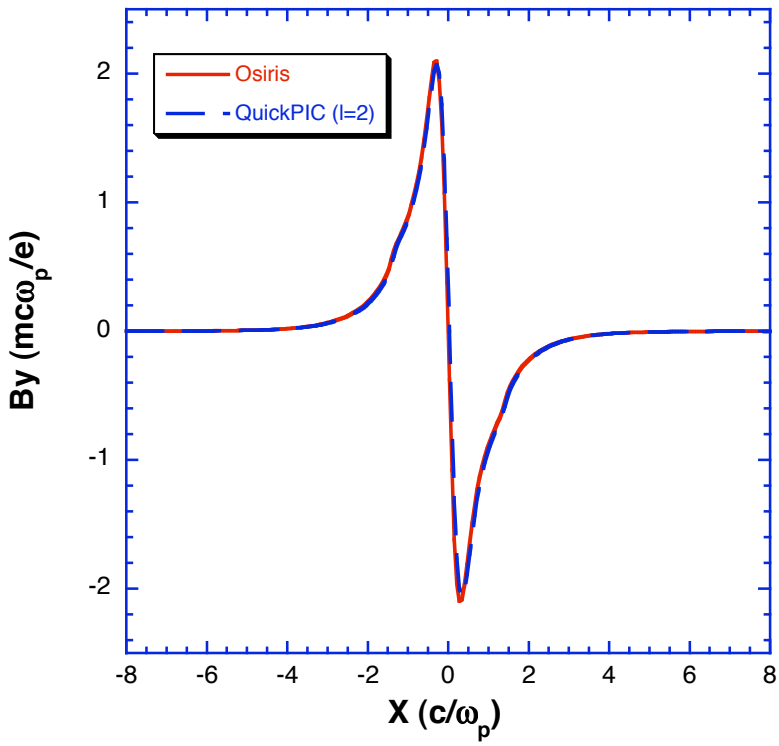

Figure 4.3: Azimuthal magnetic field comparison for electron drive beam.

Figs. 4.2 and 4.3 show the radial electric fields and the azimuthal magnetic fields along the x direction at the center of box ($\xi = 0$). Excellent agreement is observed for both comparisons. There is a plasma sheath at radius $r \approx 1.5c/\omega_p$ which carries high charge and current densities. The fields from the plasma sheath almost cancel the fields from the beam. Therefore, both E_x and B_y are small outside the sheath.

4.2 Benchmark for a positron beam driver

For the second benchmark we use a positron beam driver. A positron beam attracts plasma electrons to the axis and creates a density compression region near the axis. This process is non-linear in that electrons move towards the axis with trajectories that cross. The resulting wake structure is small in scale, which requires fine spatial resolution, thus increasing the problem size. The lack of strong shielding from a sheath layer also makes a wide simulation box necessary. Therefore, the positron benchmark is a more stringent test for the algorithm in QuickPIC.

In the positron benchmark, we once again use a beam containing $N = 1.8 \times 10^{10}$ positrons and set $\gamma = 55800$. The beam spot sizes are $\sigma_r = 25\mu m$ and $\sigma_z = 600\mu m$ respectively, and the emittances are $\epsilon_x = \epsilon_y = 15mm \cdot mrad$. The plasma density is $n_0 = 2.0 \times 10^{14} cm^{-3}$, the peak density ratio is $n_b/n_0 = 15.2$ and $k_p\sigma_r = 0.067 << 1$. The OSIRIS simulation uses a $4c/\omega_p \times 4c/\omega_p \times 16c/\omega_p$ box with $512 \times 512 \times 256$ cells. The QuickPIC simulation uses a $8c/\omega_p \times 8c/\omega_p \times 16c/\omega_p$ box with $1024 \times 1024 \times 256$ cells. Here a larger box in the QuickPIC simulation is needed due to the fact that a particle reflecting boundary is used in QuickPIC. To show the fine wake structure, we plot the plasma density in both simulations in Fig. 4.4. The plots show a small region of the simulation domain to give a

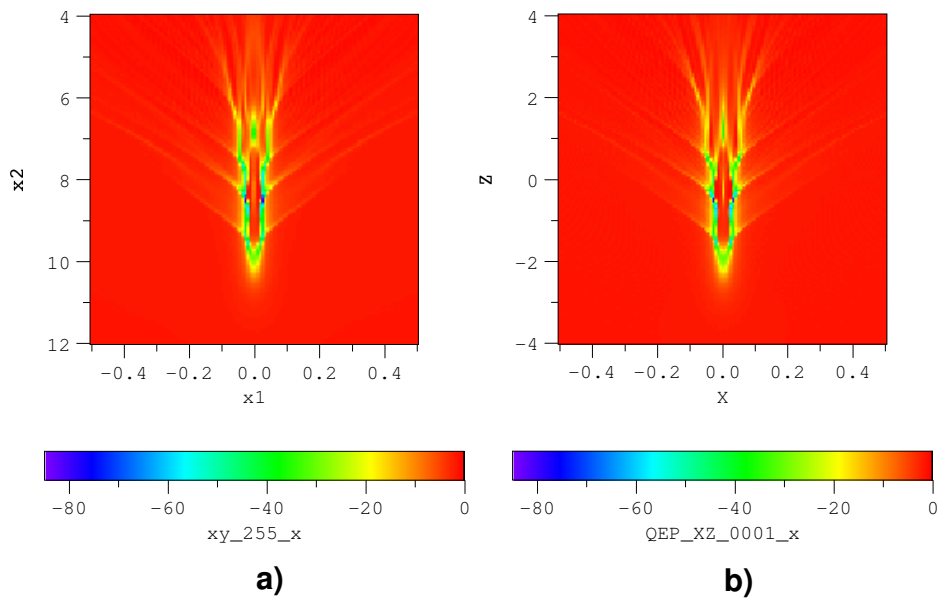

Figure 4.4: The plasma electron charge density (ρ_p/ρ_{ion}) in the $x-z$ plane at the center of the beam is shown for a) an OSIRIS simulation and b) a QuickPIC simulation. In both cases, the driver moves from top to bottom.

better view of the positron wake. The plots show a low density area near the axis and wing-like structures formed around it. The QuickPIC simulation once again reproduces very faithfully most of the detailed features in the OSIRIS results.

Figures 4.5-4.7 are comparisons of the wake fields for the positron driver. Both simulations show fine scale fluctuations in the longitudinal wakefield E_z and multiple spikes in E_x (for the center slice with $\xi = 0$). These are the results of the variations of local charge density near the beam core due to strong phase-mixing as the electrons are drawn to the axis by the positron beam. However, this process does not generate strong plasma currents to cancel the beam current.

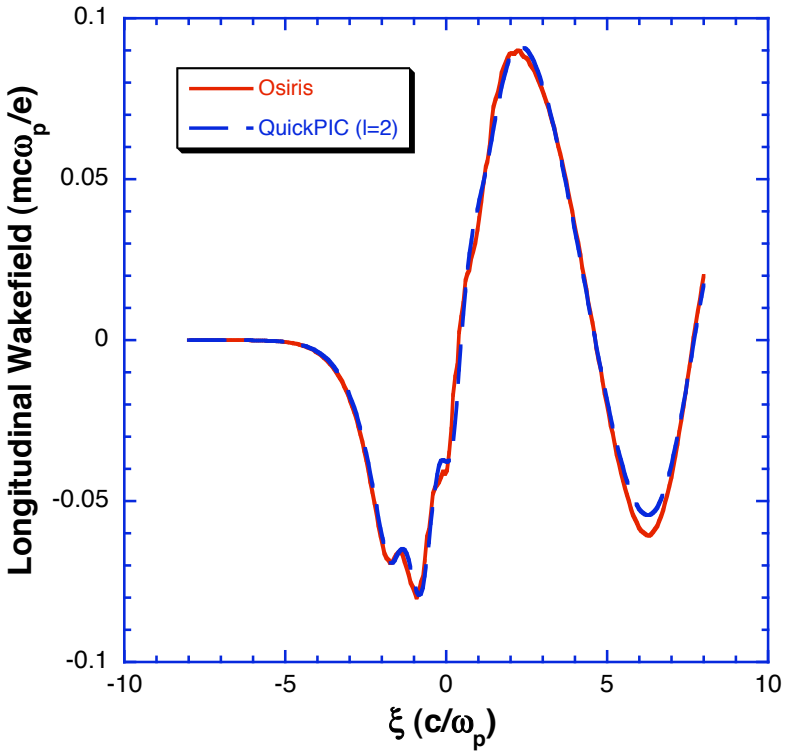

Figure 4.5: Comparison of the longitudinal wakefield for a positron driver.

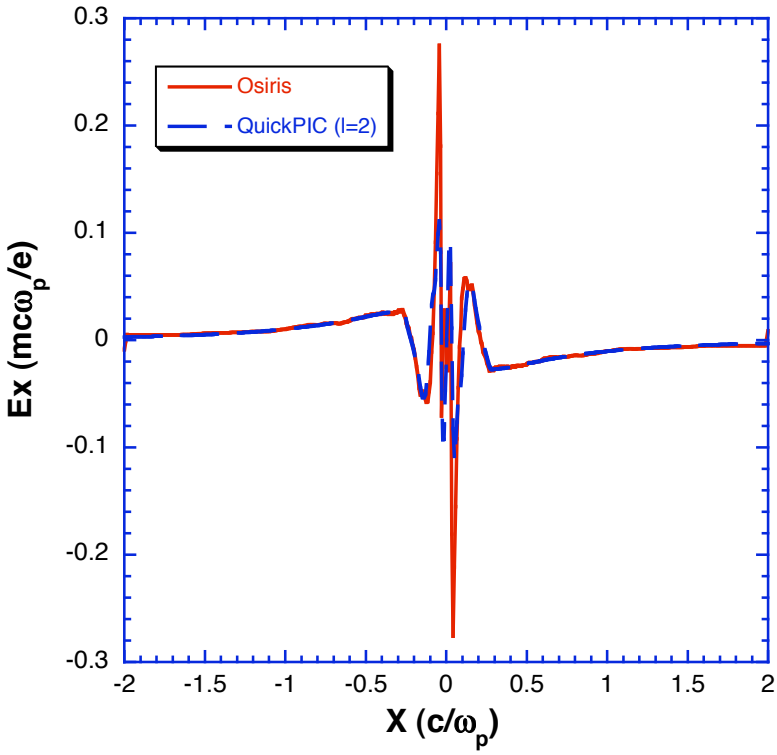

Figure 4.6: Radial electric field in the positron benchmark simulation.

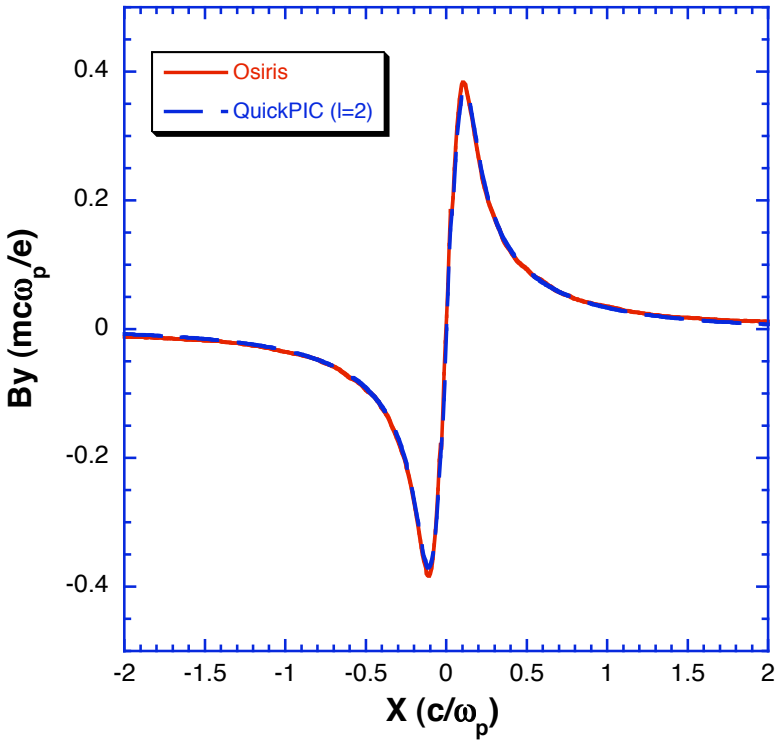

Figure 4.7: Azimuthal magnetic field in the positron benchmark simulation.

Therefore, the azimuthal magnetic field is dominated by the beam current. As seen in this benchmark, QuickPIC achieves very good agreement in the non-linear regime. Finally, it should be noted that the positron wake fields are sensitive to the spatial resolution, simulation box size, beam evolution after propagation into the plasma and other boundary effects. A careful simulation setup is necessary for the benchmark. The subtle differences between the two simulations observed in Fig. 4.5, such as a small plateau region of the first decelerating field, the amplitudes of the second decelerating field and the peak radial electric field, are mostly due to these four factors.

4.3 Benchmark for a laser driver

The last benchmark is for a laser driver. The benchmark problem is adopted from the standard problem proposed in ref. [86] with some modifications to the laser parameters. The vector potential (not intensity) of the laser pulse has a longitudinal profile of the polynomial form $10t'^3 - 15t'^4 + 6t'^5$ where

$$t' = [1 - H(t - t_0)](t_0 - t)/t_{rise} + H(t - t_0)(t - t_0)/t_{fall} \tag{4.1}$$

and $H(t)$ is the Heaviside function. Here the laser has $t_{rise} = t_{fall} = 30fs$ and the wavelength is $800nm$. The profile is defined for the electric field, not the intensity. The laser propagates in a uniform plasma with matching density $n_0 = 1.38 \times 10^{19} cm^{-3}$. For this density, $\omega_0/\omega_p = 11.24$ and the non-relativistic plasma skin depth equals the FWHM of the laser pulse longitudinal profile. The transverse profile is Gaussian and the FWHM of the focused spot size is $w_0 = 13.66\mu m$ at the plasma entrance. The normalized vector potential of the laser is $|\hat{\mathbf{a}}| = 2$, thus the laser-plasma interaction is in the non-linear blow-out regime.

The size of the simulation box is $320c/\omega_0 \times 320c/\omega_0 \times 321.8c/\omega_0$ or $28.47c/\omega_p \times 28.47c/\omega_p \times 28.63c/\omega_p$ in the OSIRIS simulation. The number of the grids is $512 \times 512 \times 1024$. For the 3D OSIRIS simulation, $\Delta t = 0.235c/\omega_0$, which satisfies the Courant condition. And the laser pulse has traveled $312.55c/\omega_0$ into the plasma so that the laser pulse has not yet evolved. The QuickPIC simulation has a shorter box $320c/\omega_0 \times 320c/\omega_0 \times 157.2c/\omega_0$ to show the first wake bucket as the OSIRIS simulation shows trapped particles in the second bucket. $256 \times 256 \times 256$ grids are used in the QuickPIC simulation. For the relatively small frequency ratio used the two simulations use a similar number of grids. However, if the frequency ratio were increased by a factor R, the OSIRIS simulation would need R times as many cells in z while the QuickPIC simulation would not. Fig. 4.8 shows the longitudinal wakefield benchmark for the OSIRIS and QuickPIC simulations. The curve from the QuickPIC simulation closely resembles the OSIRIS result, and it is smooth while the OSIRIS curve is modulated by the second harmonic of the $\mathbf{V} \times \mathbf{B}$ force.

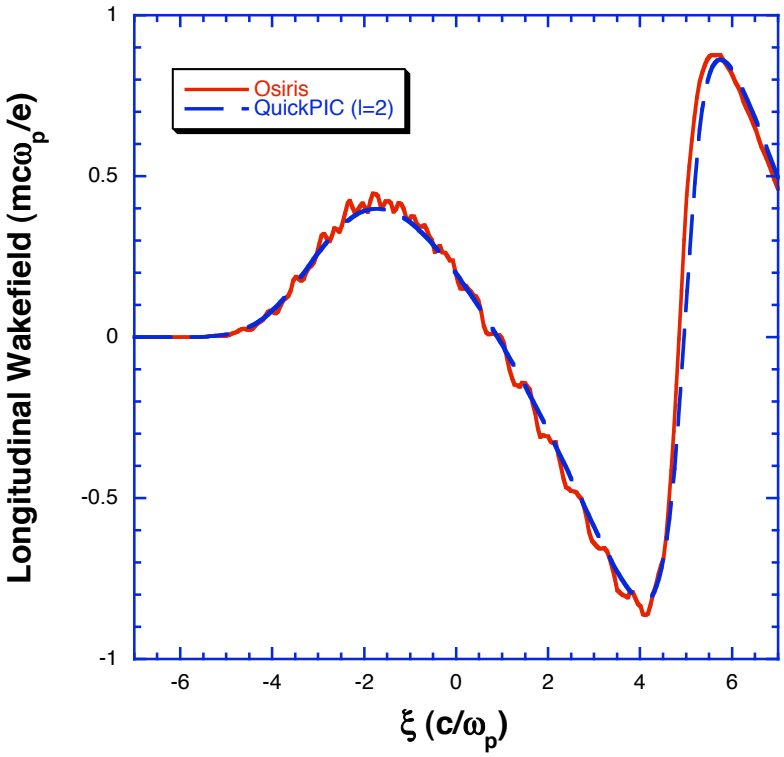

Figure 4.8: Longitudinal electric field comparison for a laser driver.

CHAPTER 5

Hosing instability

In this chapter, we will use QuickPIC to study the hosing instability of an intense drive beam in the "afterburner" scenario. Earlier work on the hosing instability in a simple equilibrium geometry indicates that the hosing instability will be very severe and break up the drive beam in a short distance. We use QuickPIC to verify the result in this simplified situation. The possible "afterburner" design is in a regime not suitable for this simplified theory. The ion channel is self-generated by the drive beam and the blow-out process is non-adiabatic and relativistic. We will derive a new linear hosing theory based on trajectory perturbation in the self-consistent fields and show that QuickPIC simulations agree very well with the new theory.

5.1 Hosing Instability

In the linear regime of PWFA where the beam density is lower than the background plasma density, an instability known as the Transverse Two Stream (TTS) instability arises from the strong coupling of the plasma [22, 64]. Similar instability could happen when the beam density is higher than the plasma density. In this case the plasma electrons are expelled from the beam's path and the interaction is in the blow-out regime. This instability is then known as the hosing instability, and it is one of the most important instabilities for intense

beam-plasma interactions. Hosing is a transverse instability of the beam which grows from an initial displacement of the beam centroid. There are basically two regimes of hosing, as characterized by Whittum [87]; one is the ion-hose instability which results from the interaction between ions and the beam electrons, the other one is the electron-hose instability in which the electron sheath in a blow-out channel couples with the beam. In the possible "afterburner" scenario, the ion motion is negligible during the time for the beam to pass by, therefore only the electron-hose is of importance.

The electron hosing instability is usually triggered by the head-tail offset of the beam. A tilted beam perturbs the plasma electron blow-out trajectory, creating a slightly displaced ion channel. A shifted ion channel will exert a force on the beam electrons which pulls them toward the direction of the perturbation. Thus a positive feedback between the electron sheath and the beam electrons is established along the beam. Due to the relativistic mass of the beam electron, this kind of hosing occurs on the betatron timescale. But the wavelength and frequency of the transverse beam centroid oscillation have non-linear dependencies on the propagation distance and the longitudinal position relative to the beam.

Fig. 5.1 shows a typical real space plot of the beam for the nominal parameters in [24] (see also Table 5.1) when hosing occurs and saturates over time.

The initial beam in Fig. 5.1 has a bi-Gaussian profile, i.e.,

$$n_b = \frac{N}{(2\pi)^{3/2}\sigma_r^2\sigma_z} e^{-((x-x_b)^2+y^2)/2\sigma_r^2} e^{-\xi^2/2\sigma_z^2}. \tag{5.1}$$

The beam centroid x_b is defined as the average position of the beam particles for each longitudinal position in the beam. A linear tilt with slope $x_b/\xi = 0.011$ is imposed on the centroid and the center of the beam is placed in the middle of the simulation box. From Fig. 5.1, it can be seen that there are three main

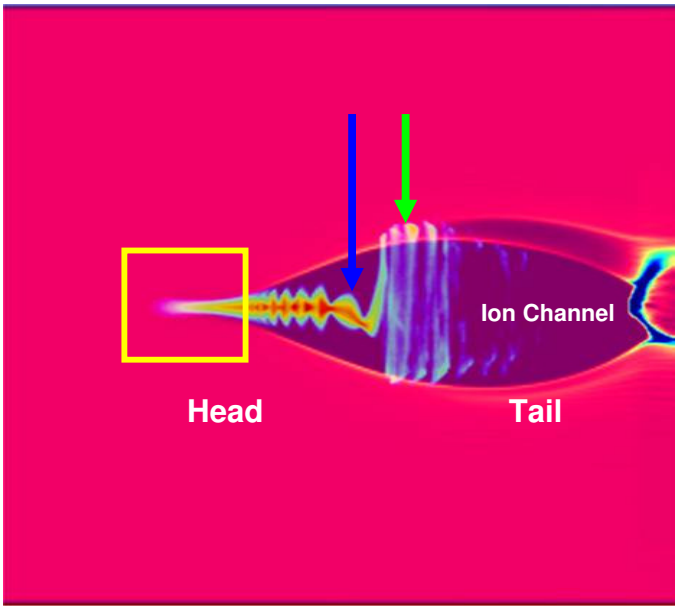

Figure 5.1: A plot of the shape of the beam and the ion channel in the nominal "afterburner" simulation.

Parameters	Value
Initial energy (GeV)	30
Beam charges (10^{10})	1.8
Emittance ϵ_N ($mm \cdot mrad$)	15
Spot size σ_r (μm)	7
Bunch length σ_z (μm)	45
Plasma density (cm^{-3})	2.0×10^{16}
Plasma length (cm)	255
Density ratio (n_b/n_0)	25.9
Slope of linear tilt	0.011

Table 5.1: Nominal parameters for the hosing simulation.

regions along the beam which exhibit different behaviors. The first one is the region near the head of the beam, i.e., the yellow box in Fig. 5.1. This is the place where the ion channel begins to form and the beam in this region displays little hosing. Even for a strong beam, this underdense region is too short for any hosing instability to grow. Indeed, the lack of hosing in this region is observed in many simulations. Simulation results always show a self-aligning effect at the front of the beam, in which the latter part of the head aligns with the former part gradually. It is difficult to quantify the exact reasons for this behavior. Here we provide some qualitative explanations. At the very front of beam where the beam density is lower than the plasma density, the analysis of transverse two stream instability applies and the growth rate is generally orders of magnitude smaller than the one for the hosing instability. Further back in the beam where the density is sufficiently large, the electrons begin to blow out, yet there are substantial trajectory crossing and phase mixing. And the ion channel is not completely formed under this situation, thus reducing the focusing force on the

beam. The combined effect of these three factors will certainly lead to a much smaller growth rate for hosing, if there is any. Therefore, for practical reasons we may assume there is no hosing in this region.

The second region is around the area indicated by the blue arrow. In this region, the ion channel is completely formed. It has a clear edge and the electron motion in the plasma sheath at the ion channel boundary is very laminar. Therefore the shape of the ion channel can be represented by a single particle's trajectory. Clear evidences of the hosing growth are observed in many numerical simulations. Hosing causes the beam centroid to oscillate with an increasing amplitude, Fig. 5.2 shows the centroid oscillation for the point indicated by the blue arrow in Fig. 5.1.

We have discussed two regions of interaction in beam hosing instability. Further back in the beam, where the beam centroid oscillation amplitude becomes large and comparable to the channel radius, the beam hits the boundary of the ion channel and particles are lost when they get out of the channel. Therefore the maximum centroid oscillation amplitude is limited by the width of the ion channel. This is the third region of the hosing behavior which is indicated by the green arrow in Fig. 5.1.

When the amplitude of the hosing oscillation is small, the electron beam can still be considered rigid and can be described by the centroid position x_b. Also the perturbed trajectory of an plasma electron only slightly deviates from an unperturbed one. Therefore the electron density at the ion channel boundary is changed slightly. To the lowest order, the effect of the density perturbation can be approximated by a dipole moment created by shifting the ion channel by a small amount. The shifted ion channel centroid x_c, which is defined as the equilibrium position (force is zero) in the channel(Fig. 5.3), is determined by the plasma

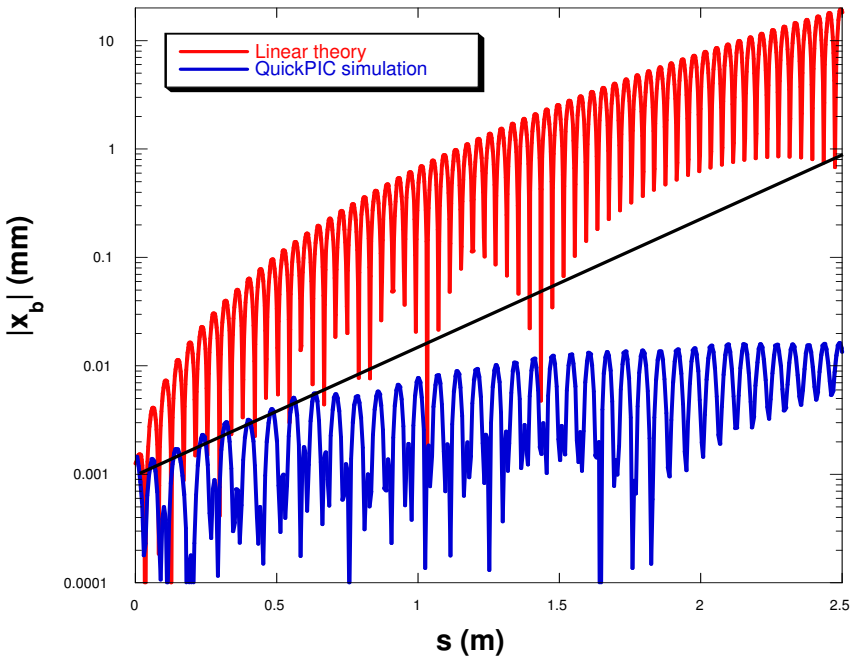

Figure 5.2: The absolute value of the centroid position $|x_b|$ in a self-generated channel (blue curve) and the prediction from a linear theory for a equilibrium channel (red curve). The black line is a linear fit for the initial growth in the simulation before the nonlinearity occurs. This initial growth is orders of magnitude smaller than the result for a equilibrium channel. The hosing amplitude begins to saturate for $s > 0.6m$.

response to the electron beam. On the other hand, the beam feels an asymmetric focusing force from the ion channel. The coupling of the beam centroid and the channel centroid will eventually cause the beam to hose. A diagram of the linear hosing analysis is shown in Fig. 5.3.

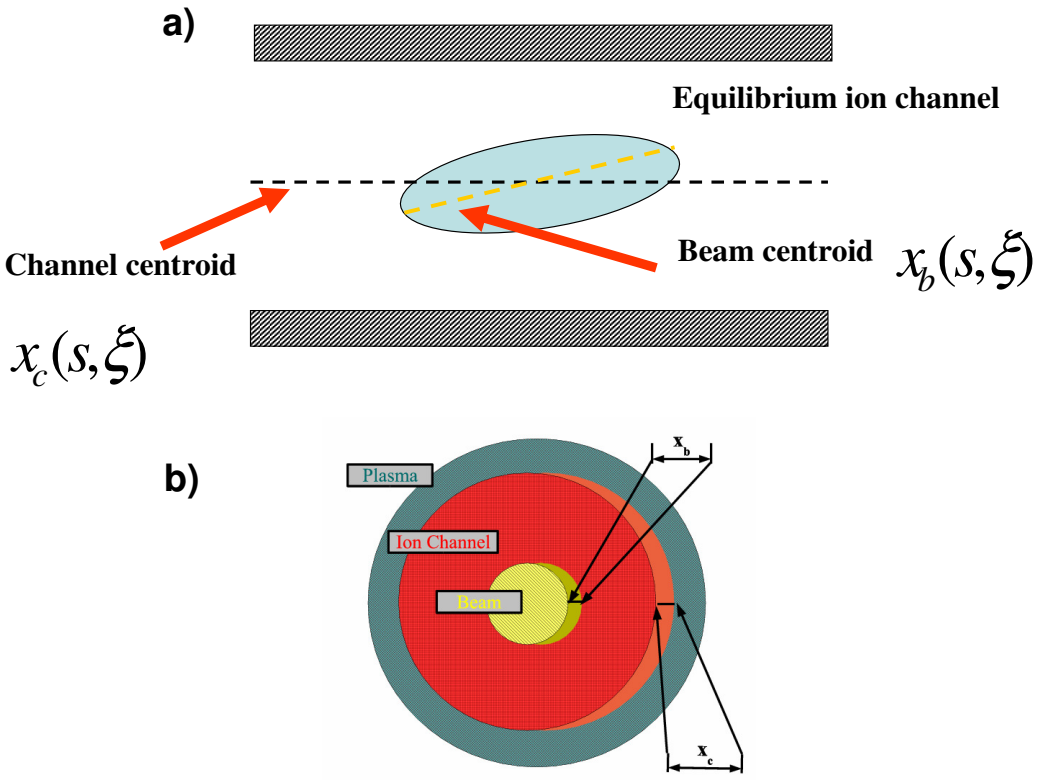

Figure 5.3: A diagram of the linear fluid analysis for hosing instability. a) the tilted beam in a equilibrium channel. b) the cross-sections of the beam and the ion channel which are shifted by an amount of x_b and x_c respectively.

A linear fluid model for the hosing instability in a equilibrium channel was developed by Whittum in [43]. Here we will introduce this model which serves as a starting point for a new theory suitable for a non-equilibrium channel. By

equilibrium, we mean that the channel radius is defined by the charge neutralization radius $r_{equ} = r_{neu} = \sqrt{n_b r_b^2/n_p}$, where r_b is the radius of a flat top beam, and for a beam with Gaussian profile, $r_b = \sqrt{2}\sigma_r$. In an equilibrium channel, the plasma electrons have no radial velocity. Furthermore the longitudinal velocity is assumed to be small, therefore the plasma electrons only feel the space charge force. The longitudinal velocity is not negligible for very intense beam for which $r_{equ} >> c/\omega_p$. The equilibrium channel is not a typical situation for most beam plasma interactions and it is not appropriate for PWFA studies. However, when the beam is long, i.e., $\tau >> 1/\omega_p$, where τ is the bunch duration, the plasma does respond adiabatically to the beam and if the normalized charge per unit length $n_b/n_0(k_p\sigma_r)^2$ is not too large, the longitudinal velocities of electrons in the sheath are non-relativistic. Under these conditions, one can assume a equilibrium channel.

By adopting the above assumptions, one can derive the coupled equations for the beam centroid and the channel centroid based on a fluid description. The potentials ψ and ϕ can be written as $\psi = \psi_0 + \psi_1$ and $\phi = \phi_0 + \phi_1$, where subscript 0 denotes the unperturbed quantities and subscript 1 are for the perturbations. ψ_1 and ϕ_1 can be calculated from the Maxwell's equations,

$$\nabla_\perp^2 \psi_1 = -4\pi\rho_{e1}, \tag{5.2}$$

$$\nabla_\perp^2 \phi_1 = -4\pi(\rho_{b1} + \rho_{e1}). \tag{5.3}$$

Since the longitudinal velocities of the electrons are assumed to be small, we can drop the longitudinal current in the continuity equation of the plasma electrons. The linearized continuity equation can be written as,

$$\frac{\partial \rho_{e1}}{\partial \xi} + \nabla_\perp \cdot (\rho_{e0} \mathbf{v}_{e1}) = 0. \tag{5.4}$$

The plasma electron's motion is assumed to be non-relativistic under the space charge perturbation from the beam and the electron sheath itself.

$$\frac{\partial \mathbf{v}_{e1}}{\partial \xi} = \frac{e}{m} \nabla_\perp \phi_1. \tag{5.5}$$

There are no electrons in the ion channel, i.e., $\rho_{b0} = 0$ for $r < r_{equ}$, so it can be seen from Eq. (5.4) that the perturbation on the plasma electron density ρ_{e1} only exists at the channel boundary. To the lowest order, the ion channel is still round with radius r_{equ} and only shifts to a new centroid position x_c. Thus the density perturbation takes the form $\rho_{e1} = e n_p x_c cos\theta \delta(r - r_{equ})$, where $\delta(r)$ is the Dirac delta function and θ is the azimuthal angle in the transverse plane.

Note that for 2D slab geometry, the electric field at the channel from the density perturbation of the beam will be independent of x_b. Therefore, hosing can only occur in full 3D geometry.

For small perturbations, the distortion of the beam is considered negligible. Therefore, the density perturbation can be determined in the same way as the perturbation to the plasma electrons, giving $\rho_{b1} = e n_b x_b cos\theta \delta(r - r_b)$. Substituting the expressions for ρ_{e1} and ρ_{b1} into 5.3, then combining Eqs. (5.4) and (5.5), one can obtain the equation of x_c for a given x_b. In normalized units, it can be written as

$$\partial_\xi^2 x_c + \omega_0^2 x_c = \frac{n_b r_b^2}{n_p r_{equ}^2} \omega_0^2 x_b, \tag{5.6}$$

where $\omega_0 \equiv k_p/\sqrt{2} = \omega_p/\sqrt{2}c$ and $\frac{n_b r_b^2}{n_p r_{equ}^2} = 1$ for the equilibrium channel.

The particle beam moves at a speed close to the speed of light, so an individual beam electron does betatron oscillation around the equilibrium position under the focusing force from the ion channel. When the beam and the channel are disturbed, the restoring force on the beam is determined by the relative position $(x_c - x_b)$. The equation of motion for the beam centroid can be written as,

$$\partial_s^2 x_b + k_\beta^2 x_b = k_\beta^2 x_c, \tag{5.7}$$

where $k_\beta = k_p/\sqrt{2\gamma}$ is the betatron wavenumber.

Eqs. (5.6) and (5.7) describe the couping of the beam centroid and the ion channel centroid for the small amplitude hosing instability. The asymptotic solution for a short bunch $\omega_0 \xi << k_\beta s$ is given in [44]. We provide it here as a reference,

$$x_b(s,\xi) \approx \frac{3^{7/4}}{2^{7/2}\pi^{1/2}} \frac{x_b(0,\xi)}{A^{3/2}} e^A \cos(k_\beta s - \frac{A}{\sqrt{3}} + \frac{\pi}{4}) \tag{5.8}$$

In Eq. 5.8, $A(s,\xi) = \frac{3^{3/2}}{4}\left[(k_\beta s)(\omega_0 \xi)^2\right]^{1/3}$.

The asymptotic solution, Eq. (5.8), is plotted in the red curve in Fig. 5.2 for the parameters shown in Table (5.1) and it is compared with a simulation result in the blue curve. In the simulation, the bunch length was $k_p\sigma_z = 1.2$. The centroid oscillation in the simulation follows a linear exponential growth which is measured by the black curve and then saturates after a certain distance. If the growth was linear for the entire simulation, the final oscillation amplitude would still be one order of magnitude smaller than the prediction from Eq. (5.8). This comparison clearly shows that the above fluid analysis of the hosing instability does not give correct predictions for the non-linear blow-out regime of an intense short beam. In the next section, we will reanalyze the hosing instability in terms

of the motion of an electron at the edge of the ion channel.

5.2 Hosing theory and verification

5.2.1 Hosing theory based on particle model

In this section we will introduce a particle model for the hosing instability analysis. The model is based on the perturbation to a plasma electron's trajectory in the blow-out regime. The main assumptions are,

1. The perturbation is on the 0th order trajectory and is assumed to be small; therefore this is still a linear perturbation theory. In the fluid model, there is no 0th order trajectory, since the electrons are at rest.

2. The beam centroid is treated the same way as in the previous analysis. This means that the beam is round and it must be narrow compared with the blow-out radius, so the additional effects caused by the deformation of the beam can be neglected.

3. The deformation of the channel shape under small amplitude perturbation is omitted, therefore the channel is only shifted to a new position.

4. The center of the channel can be defined as $x_c(\xi) = (r_+(\xi) - r_-(\xi))/2$, where $r_+(\xi)$ and $-r_-(\xi)$ are defined as the trajectories of the innermost electrons at the upper and lower boundaries of the ion channel in the plane of the perturbation. This is illustrated in Fig. 5.4. We define $(r_+ + r_-)$ as the diameter of the channel. The change of this quantity is assumed to be a higher order effect and is consequently dropped in our analysis.

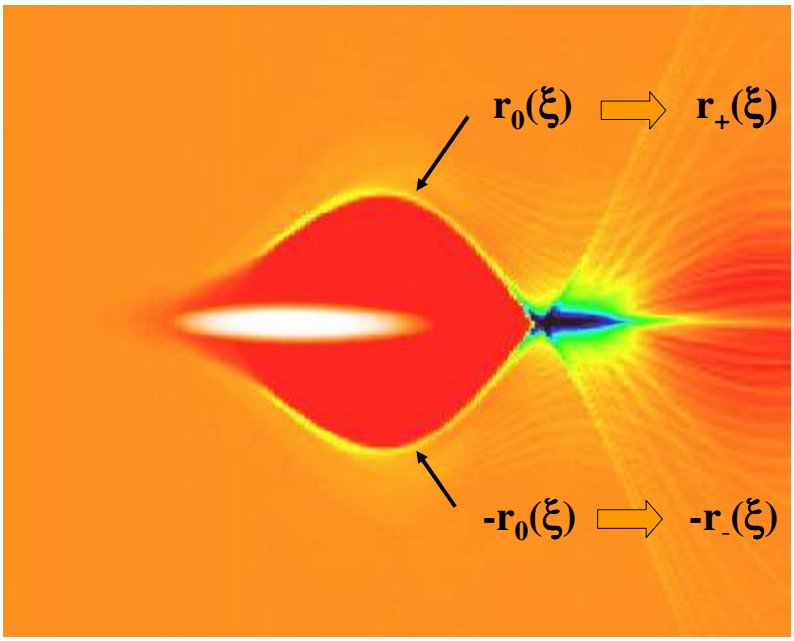

Figure 5.4: A cartoon for the trajectory perturbation model used in the hosing analysis. $\pm r_0$ are the unperturbed trajectories of the innermost electrons and r_+, $-r_-$ are their perturbed trajectories respectively.

Based on these assumptions, we will derive new coupled equations for the channel centroid. The derivation starts from the relativistic equation of motion for a plasma electron,

$$\frac{d\mathbf{P}_\perp}{dt} = \frac{d}{dt}(\gamma\frac{dr}{dt}) = -(E_r - V_z B_\theta), \tag{5.9}$$

where we adopt the same notations and definitions as used in Chapter 2 but the normalized units $c = 1$, $e = 1$ and $m = 1$ are used for simplicity.

The derivative with respect to time can be written in terms of the fast time scale variable ξ. Using $\gamma(1 - V_z) = 1 + \psi$, it becomes,

$$\frac{d}{dt} = (1 - V_z)\frac{d}{d\xi} = \frac{1+\psi}{\gamma}\frac{d}{d\xi}. \tag{5.10}$$

Substituting Eq. (5.10) and $\gamma = \frac{1+P_\perp^2+(1+\psi)^2}{2(1+\psi)}$ into Eq. (5.9), one can obtain,

$$\frac{2(1+\psi)^2}{1+(1+\psi)^2(\frac{dr}{d\xi})^2+(1+\psi)^2}\frac{d}{d\xi}\left[(1+\psi)\frac{dr}{d\xi}\right] = -(E_r - V_z B_\theta), \tag{5.11}$$

where ψ is the solution to $-\nabla_\perp^2\psi = 4\pi(\rho - J_z)$. Eq. (5.11) can be rewritten as,

$$\begin{aligned} & 2(1+\psi)^2\frac{d}{d\xi}\left[(1+\psi)\frac{dr}{d\xi}\right] \\ = \; & -(E_r - V_z B_\theta)\left[1+(1+\psi)^2(\frac{dr}{d\xi})^2+(1+\psi)^2\right]. \end{aligned} \tag{5.12}$$

Eq. (5.11) or Eq. (5.12) describes the trajectory of an electron in the self-consistent radial electric and azimuthal magnetic fields. When the beam is straight, i.e., there is no perturbation, the solution for $r(\xi)$ is $r_0(\xi)$, and the

fields and potential are E_{r0}, $B_{\theta 0}$ and ψ_0. The longitudinal velocity is denoted as V_{z0}.

Next we perturb this equilibrium solution by small perturbations which are designated by subscript "1" in the following equations.

$$r = r_0 + r_1, \tag{5.13}$$

$$E_r(r_0 + r_1) = E_{r0} + E_{r1}, \tag{5.14}$$

$$B_\theta(r_0 + r_1) = B_{\theta 0} + B_{\theta 1}, \tag{5.15}$$

$$V_z(r_0 + r_1) = V_{z0} + V_{z1}, \tag{5.16}$$

and

$$\psi(r_0 + r_1) = \psi_0(r_0). \tag{5.17}$$

Relationship (5.17) follows from the assumption that the channel shape does not change and the channel is simply displaced by r_1.

We now substitute the above expansions into Eq. (5.12) and order the resulting terms.

The $0th$ order equation is,

$$\begin{aligned} & 2(1+\psi_0)^2\dot{\psi}_0\dot{r_0} + 2(1+\psi_0)^3\ddot{r_0} \\ = \; & -(E_0 - V_{z0}B_0)\left[1 + (1+\psi_0)^2\dot{r_0}^2 + (1+\psi_0)^2\right]. \end{aligned} \tag{5.18}$$

here we adopt the convention $\frac{d\psi}{d\xi} \equiv \dot{\psi}$.

The $1st$ order equation is,

$$
\begin{aligned}
& 2(1+\psi_0)^2\dot{\psi}_0\dot{r_1} + 2(1+\psi_0)^3\ddot{r_1} \\
= \; & -2(E_0 - V_{z0}B_0)(1+\psi_0)^2\dot{r_0}\dot{r_1} \\
& -(E_1 - V_{z0}B_1 - V_{z1}B_0)\left[1 + (1+\psi_0)^2\dot{r_0}^2 + (1+\psi_0)^2\right] \qquad (5.19)
\end{aligned}
$$

We next use the 0th order solution to reduce Eq. (5.19) further. From the $0th$ order equation, the Lorentz force can be expressed as,

$$
-(E_0 - V_{z0}B_0) = \frac{1+\psi_0}{\gamma_0}\left[(1+\psi_0)\ddot{r_0} + \dot{\psi}_0\dot{r_0}\right]. \qquad (5.20)
$$

Dividing the $1st$ order equation by $2(1+\psi_0)^3$ and substituting Eq. (5.20) into the new equation, Eq. (5.19) becomes,

$$
\ddot{r_1} + \left\{\frac{\dot{\psi}_0}{1+\psi_0} - \frac{1}{\gamma_0}\left[(1+\psi_0)\ddot{r_0} + \dot{\psi}_0\dot{r_0}\right]\dot{r_0}\right\}\dot{r_1} = -\frac{\gamma_0}{(1+\psi_0)^2}(E_1 - V_{z0}B_1 - V_{z1}B_0). \qquad (5.21)
$$

Eq. (5.21) is a second order ODE for the perturbation r_1 with the known $0th$ order blow-out trajectory r_0 in the coefficients. This equation also involves the derivatives of the $0th$ order trajectory, the potential ψ_0 and its derivative and the $0th$ order longitudinal velocity and Lorentz factor along the trajectory. These are $0th$ order quantities depending on the profile of the drive beam. They can be extracted from a simulation or approximated using an analytical model described in Appendix B. The perturbation to the Lorentz force is the source term in Eq. (5.21). The self-consistent force $-(E_1 - V_{z0}B_1 - V_{z1}B_0)$ is the sum of the perturbation from the beam and the response from the charge and current at the edge of the channel. However, it is difficult to calculate the charge and current profile at the edge of the channel. We therefore express the self-consistent

force in terms of the perturbation from the beam and a numerical factor $c_1(\xi)$ which quantifies the importance of the forces from the plasma response to those from the beam tilt, i.e.,

$$-(E_1 - V_{z0}B_1 - V_{z1}B_0) = F_{b1} + F_{p1} = F_{b1}c_1(\xi), \tag{5.22}$$

where $F_{b1} = (E_{b1} - V_{z0}B_{b1})$ is the perturbation to the Lorentz force from the beam, and $F_{p1} = F_{b1}(c_1(\xi) - 1)$ is the change of the force from the plasma response. We obtain c_1 from simulations and for many situations $c_1(\xi) \sim 1$.

On the other hand, it is rather simple to derive E_{b1} and B_{b1} as they are just the change of the electric and magnetic fields from the beam when the centroid is shifted by x_b.

$$E_{b1} = B_{b1} = -2\pi n_b r_b^2 \left[\frac{1}{r_0 + r_1 - x_b} - \frac{1}{r_0}\right]. \tag{5.23}$$

Note that in 2D slab geometry, $E_{b1} = B_{b1} = 0$.

When $|r_1 - x_b| << r_0$, we can expand the total force from the beam as

$$F_{b1} = -(E_{b1} - V_{z0}B_{b1}) \approx \frac{2\pi n_b r_b^2(1 - V_{z0})}{r_0^2}(x_b - r_1). \tag{5.24}$$

Finally, Eq. (5.21) is written as,

$$\ddot{r_1} + \left\{\frac{\dot{\psi_0}}{1+\psi_0} - \frac{1}{\gamma_0}\left[(1+\psi_0)\ddot{r_0} + \dot{\psi_0}\dot{r_0}\right]\dot{r_0}\right\}\dot{r_1} = c_1c_2c_3\omega_0^2(x_b - r_1), \tag{5.25}$$

where two new factors are defined as $c_2(\xi) = \frac{1}{1+\psi_0}$ and $c_3(\xi) = \frac{n_b r_b^2}{n_e r_0^2}$. The physics which produces c_2 and c_3 will be discussed shortly.

Eq. (5.25) is for the upper trajectory $r_+ = r_0 + r_1$. The lower trajectory $-r_- = -r_0 - r_2$ can be solved using a similar equation for r_2,

$$\ddot{r_2} + \left\{ \frac{\dot{\psi_0}}{1+\psi_0} - \frac{1}{\gamma_0} \left[(1+\psi_0)\ddot{r_0} + \dot{\psi_0}\dot{r_0} \right] \dot{r_0} \right\} \dot{r_2} = -c_1 c_2 c_3 \omega_0^2 (x_b + r_2). \quad (5.26)$$

So the channel centroid, which is defined as $x_c = (r_+ - r_-)/2 = (r_1 - r_2)/2$, satisfies,

$$\ddot{x_c} + \left\{ \frac{\dot{\psi_0}}{1+\psi_0} - \frac{1}{\gamma_0} \left[(1+\psi_0)\ddot{r_0} + \dot{\psi_0}\dot{r_0} \right] \dot{r_0} \right\} \dot{x_c} = c_1 c_2 c_3 \omega_0^2 (x_b - x_c). \quad (5.27)$$

We find that for most situations of interest the effect of the terms in bracket is small. This is partly because these terms are proportional to $\dot{\psi_0}$ and $\dot{r_0}$, for weak beams each term is small while for intense beams the terms tend to cancel each other. Therefore, we drop the terms in bracket. Then the result can be cast into a form comparable to the channel centroid equation Eq. (5.6) from the fluid theory.

$$\partial_\xi^2 x_c + c_1 c_2 c_3 \omega_0^2 x_c = c_1 c_2 c_3 \omega_0^2 x_b. \quad (5.28)$$

In Eq. (5.28), c_1, c_2 and c_3 are all functions of $r_0(\xi)$. Therefore the strength of the coupling from the beam centroid to the channel centroid varies along the blow-out trajectory. In general, these coefficients can be obtained from a simulation without perturbations. In Appendix B, an analytical model to determine $r_0(\xi)$ and $\psi_0(\xi)$ is introduced. In principle, c_2 and c_3 which depend on $r_0(\xi)$ and $\psi_0(\xi)$ can be analytically calculated for an arbitrary beam profile.

For adiabatically formed channels with small blow-out radius, plasma electrons are pushed to the charge neutralization radius slowly, $V_r \approx 0$ and $V_{z0} \approx 0$.

The fields from the plasma sheath is weak, and so are the perturbations to the fields. In this case, $\psi_0 << 1$, $r_0 = r_b$, and $F_{p1} \approx 0$. Therefore, $c_1 \approx c_2 \approx c_3 \approx 1$, the result of the fluid model is recovered. If the beam-plasma interaction becomes more intense, the plasma electrons will be relativistic and the plasma sheath carries large charge and current densities. These lead to three important physical effects: 1) The plasma sheath generates strong electric and magnetic fields which tend to reduce the perturbation (the c_1 coefficient); 2) The relativistic mass will change the resonant frequency, and the plasma electrons may also gain substantial longitudinal momentum so the 0th order Lorentz force becomes important (the c_2 coefficient). 3) The blow-out radius does not always equal the charge neutralization radius, so c_3 varies along the blow-out trajectory. These effects which are contained in coefficients c_1, c_2, c_3, change the hosing growth. The fluid analysis of Whittum could in principle take into account of effects 1) and 3), however they would be included in an inconsistent manner, e.g., the effect of c_3 only appears in the RHS of Eq. (5.6) not the LHS. Generally, for a relativistic non-adiabatic blow-out ion channel, $c_1 c_2 c_3 < 1$, therefore the hosing growth is reduced by the combination of all these effects.

We have derived the new channel centroid equation based on a quasi-static particle model. The analysis is simplified by dropping the $\dot{\psi}_0$ and $\dot{r_0}$ terms in Eq. (5.27). In the next section we will show that this is justified as we find excellent agreement between the new hosing theory and QuickPIC simulations.

5.2.2 Verification of the model

In this section, we present the simulation results which directly verify the correctness of our new theoretical analysis for hosing. The 3D nature of the hosing instability requires full scale 3D PIC simulations. These simulations are time-

consuming using conventional PIC codes, as the beam has to propagate several betatron wavelengths before a noticeable hosing oscillation can be detected. The vast scale difference between the betatron wavelength and plasma wavelength determines that full PIC codes are inefficient to model such an interaction. Our 3D simulations are conducted using QuickPIC, and each simulation only takes several hours on 16 CPUs on DAWSON cluster.

5.2.2.1 Hosing for the adiabatic non-relativistic blow-out regime

The first simulation is in the adiabatic non-relativistic blow-out regime. Fig. 5.5 shows the initial beam density and plasma response. Here we use two beams in the simulation to create an adiabatic channel. The first one is short and narrow, it blows out electrons creating a channel with a radius small compared with the plasma skin depth. The second beam is also narrow and it immediately follows the first beam. The density of the second beam is chosen to keep the channel flat. A linear tilt is imposed on the second beam along the moving direction, with the head of the beam on the axis and the tail off axis.

The simulation parameters are: plasma density $n_0 = 5.66 \times 10^{16} cm^{-3}$, beam spot size $\sigma_r = 9.09 \times 10^{-3} c/\omega_p$, energy of the beam $\gamma_b = 55800$, charge of the first beam $Q_1 = -2 \times 10^8 e$, charge of the second beam $Q_2 = -1.2 \times 10^9 e$. The simulation box size is $3.6c/\omega_p \times 3.6c/\omega_p \times 17.1c/\omega_p$. $256 \times 256 \times 256$ grids and 5,242,880 particles for each beam and 4 particles/cell for the plasma are used in the simulation. The density of the first beam rises linearly from zero to its maximum in $L_1 = 4.91c/\omega_p$ while the second beam has a uniform density along the axis with a length $L_2 = 11.4c/\omega_p$. The small separation of the two beams is adjusted to make the transition in the shape of the channel smooth. The maximum blow-out radius is $r_{blow-out} = 0.23c/\omega_p$ which is small compared

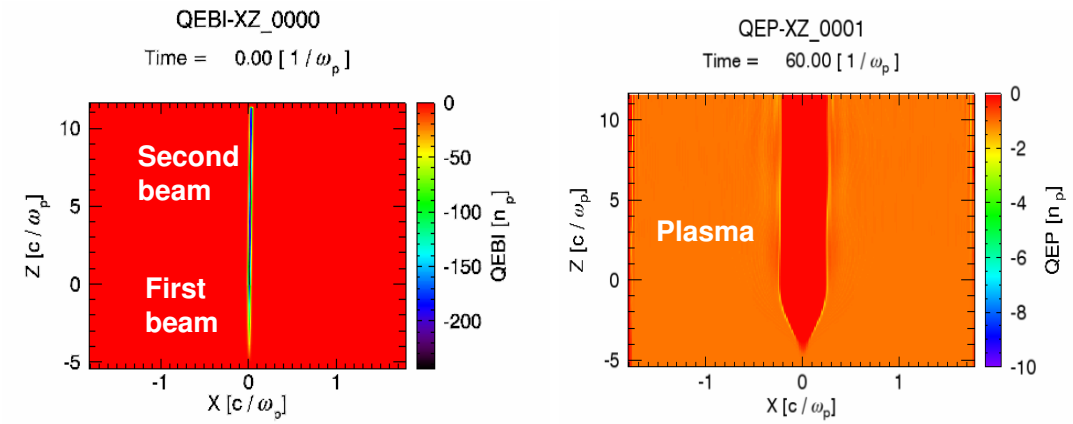

Figure 5.5: Density plot of the beams (left) and plasma (right) in the simulation for the hosing instability in the adiabatic non-relativistic blow-out regime. The beams move downward in this plot.

with the plasma skin depth. The slope of the linear tilt of the second beam is 1.96×10^{-3}.

The position of the centroid at $\xi = 3c/\omega_p$ in the second beam is plotted as a red curve in Fig. 5.6. We notice that $c_1 \approx c_2 \approx c_3 \approx 1$ in this regime, so Eq. (5.28) has the same form as Eq. (5.6). We numerically integrate the coupled equations Eq. (5.6) and Eq. (5.7) and the result is plotted as a blue curve in Fig. 5.6 which is in good agreement with the simulation result. This indicates that both our new theory and Whittum's theory can describe the hosing instability accurately in this regime.

5.2.2.2 Hosing for the adiabatic relativistic blow-out regime

The second simulation is in the adiabatic relativistic blow-out regime. Fig. 5.7 shows the initial beam density and plasma response. Similar to the first simulation, two beams are used to blow out a channel which is relatively uniform

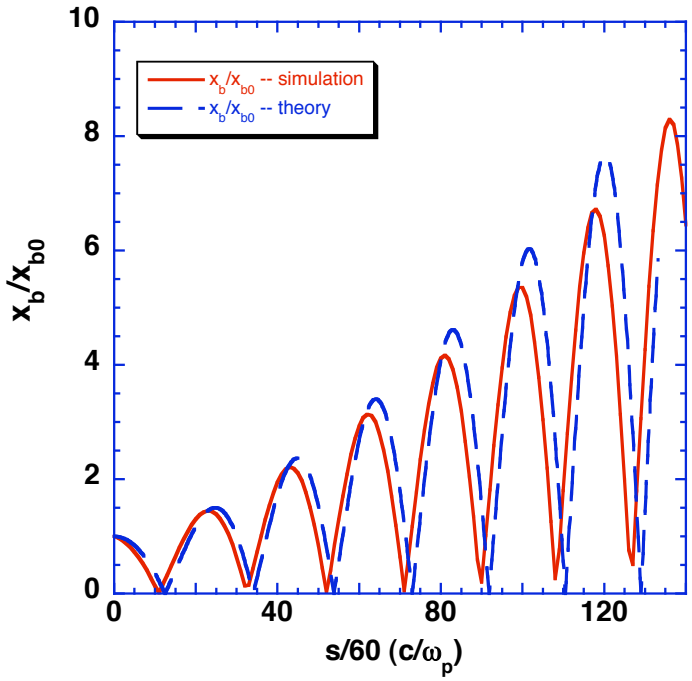

Figure 5.6: Hosing growth of the centroid oscillation as a function of propagation distance s from the simulation and the theory prediction for the adiabatic non-relativistic blow-out regime.

near the second beam. This is done by placing the second beam at a location where the blow-out radius is maximum and adjusting the total charge of the second beam such that the blow-out radius remains constant thereafter.

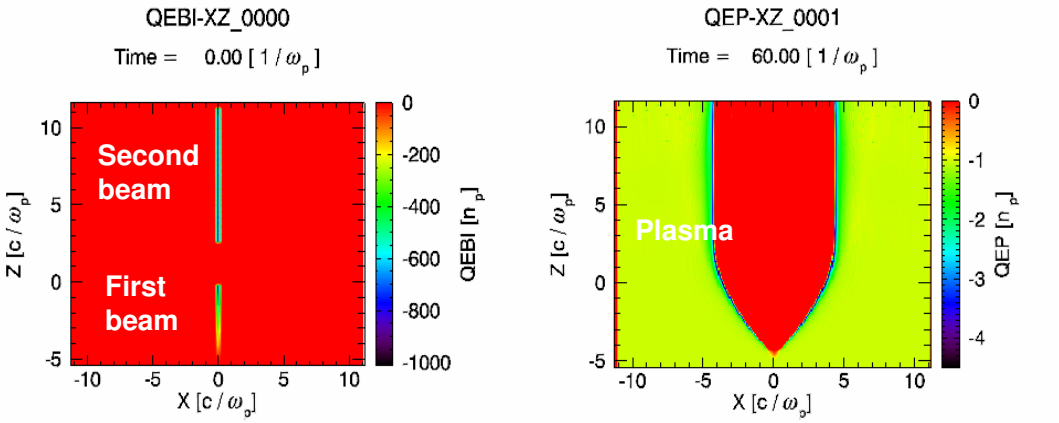

Figure 5.7: Density plot of the beams (left) and plasma (right) in the simulation for the hosing instability in the adiabatic relativistic blow-out regime.

To study hosing in this regime, we simulate a plasma density of $n_0 = 5.66 \times 10^{16} cm^{-3}$, beam spot sizes of $\sigma_r = 8.98 \times 10^{-2} c/\omega_p$, and beam energies of $\gamma_b = 55800$, charges of $Q_1 = -6 \times 10^{10} e$ and of $Q_2 = -2.4 \times 10^{11} e$ for the first and second beams respectively. The simulation box size is $22.4c/\omega_p \times 22.4c/\omega_p \times 17.1c/\omega_p$. $256 \times 256 \times 256$ grids and 524,288 particles for each beam and 4 particles/cell for the plasma are used in the simulation. The density of the first beam rises linearly from zero to its maximum in $L_1 = 4.91c/\omega_p$ while the second beam has a uniform density along the axis with a length of $L_2 = 8.72c/\omega_p$. The separation of the two beams is $D = 2.68c/\omega_p$. In this case, the maximum blow-out radius is $r_{blow-out} = 4.3c/\omega_p$. The slope of the linear tilt is 7.69×10^{-3}.

The centroid oscillation is measured for a slice at $5c/\omega_p$ in the second beam. The simulation result and the theory prediction based on the new theory are

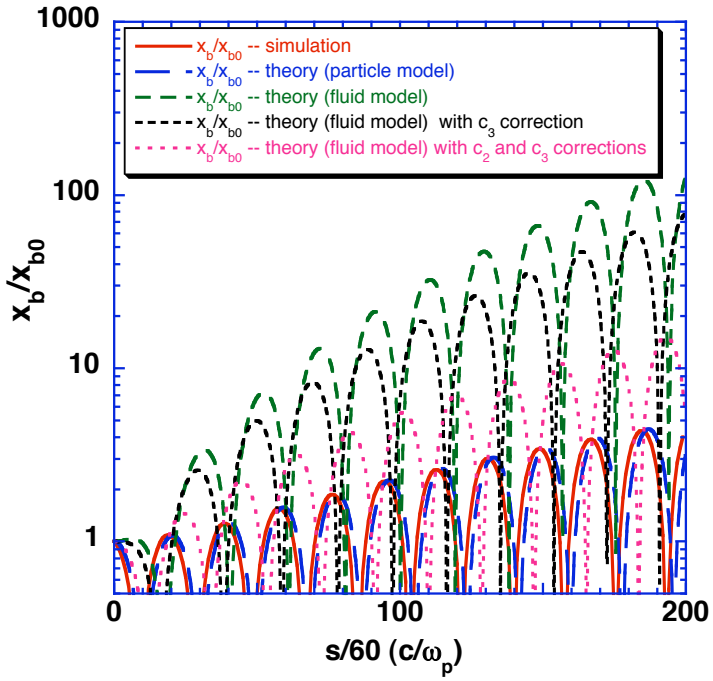

Figure 5.8: Hosing growth of the centroid oscillation as a function of propagation distance s from the simulation and the theory prediction for the adiabatic relativistic blow-out regime.

plotted at the bottom of Fig. 5.8 in red and blue curves. The three factors c_1, c_2 and c_3 are taken from simulations. The ψ_0 at the ion channel boundary is not negligible in this case (i.e., ψ_0 becomes comparable to 1), therefore the relativistic and longitudinal velocity effects represented by the c_2 factor are important as can be seen in Fig. 5.8. Because the blown-out electrons have a substantial longitudinal velocity, the Lorentz force also makes the equilibrium radius larger, this reduces hosing by reducing the factor c_3. Fig. 5.8 makes clear that the new hosing theory is in excellent agreement with the simulations, while the theory of Whittum greatly overestimates hosing growth by two orders of magnitude in only 6 betatron oscillations! Furthermore, Fig. 5.8 also shows that each coefficient is important for this situation.

5.2.2.3 Hosing for the non-adiabatic non-relativistic blow-out regime

The third case is what we refer to as the non-adiabatic non-relativistic blow-out regime. Fig. 5.9 shows the initial beam density and plasma response. Only one beam is used in the simulation. To make the blow-out more abrupt, the beam density peaks at the head and linearly decreases to zero towards the tail.

For this case, we simulate a plasma density of $n_0 = 2 \times 10^{16} cm^{-3}$, a beam spot size of $\sigma_r = 5.3 \times 10^{-3} c/\omega_p$, a beam energy of $\gamma_b = 55800$, and a beam charge of $Q = -1.8 \times 10^8 e$. The length of the beam is $L = 3.72 c/\omega_p$. The maximum blow-out radius is $r_{blow-out} = 0.24 c/\omega_p$, and the slope of the linear tilt is 4.17×10^{-3}. The simulation box size is $4c/\omega_p \times 4c/\omega_p \times 4.3c/\omega_p$. $512 \times 512 \times 256$ grids and 4,194,304 particles for the beam and 4 particles/cell for the plasma are used in the simulation.

The beam centroid oscillation at $3c/\omega_p$ in the beam is plotted vs. s in Fig. 5.10 as a red curve. The green dashed curve is the result from the fluid theory. The

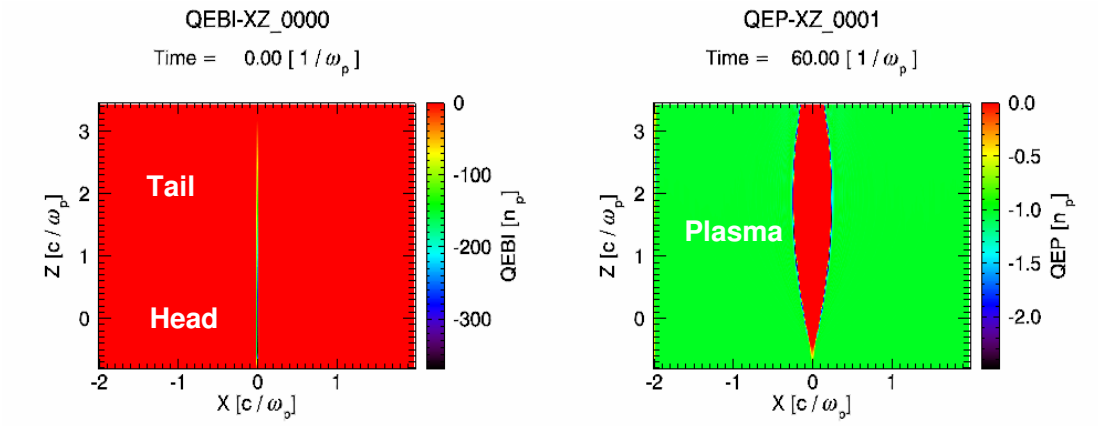

Figure 5.9: Density plot of the beams (left) and plasma (right) in the simulation for the hosing instability in the non-adiabatic non-relativistic blow-out regime.

other two curves at the bottom of the plot are the results from our theory with only c_3 correction, and with both c_2 and c_3 corrections. For this non-relativistic blow-out situation, the deviations of c_1 and c_2 from unity are small and only the position dependent correction to $c_3(\xi)$ is needed. Since the plasma response is weak in this regime, the main reason for reduced hosing growth is from the non-adiabatic nature of the blow-out process, i.e., the ξ dependence of $r_b(\xi)$.

5.2.2.4 Hosing for the non-adiabatic relativistic blow-out regime

The fourth case is what we refer to as the non-adiabatic relativistic blow-out regime. Fig. 5.11 shows the initial beam density and plasma response. This simulation is similar to the non-adiabatic non-relativistic blow-out simulation, except that the beam has more charge to make the blow-out process relativistic.

For this case, we simulated a plasma density of $n_0 = 2 \times 10^{16} cm^{-3}$, a beam spot size of $\sigma_r = 1.3 \times 10^{-2} c/\omega_p$, a beam gamma of $\gamma_b = 55800$, and a beam with charge $Q = -9 \times 10^9 e$. The length of the beam is still $L = 3.72 c/\omega_p$. The

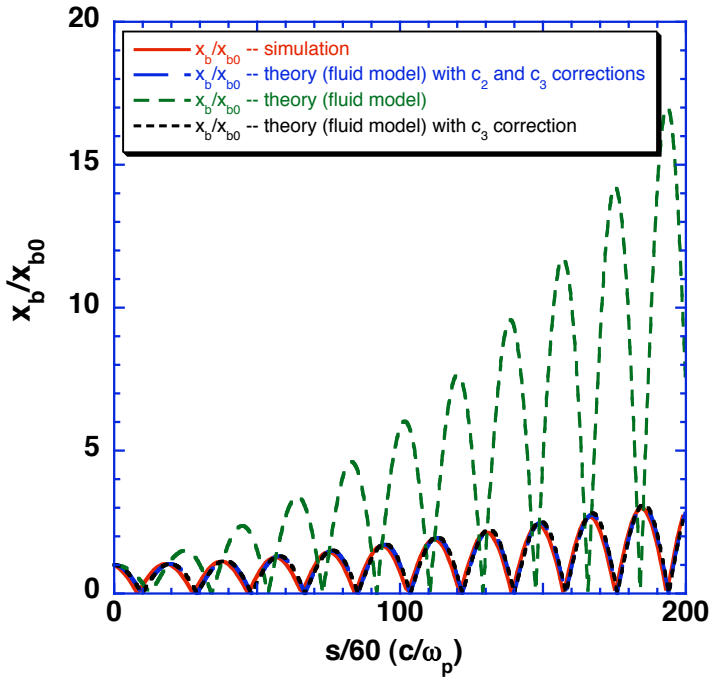

Figure 5.10: Hosing growth of the centroid oscillation as a function of propagation distance s from the simulation and the theory prediction for the non-adiabatic non-relativistic blow-out regime.

maximum blow-out radius is now $r_{blow-out} = 1.5c/\omega_p$ and the slope of the linear tilt is still 4.17×10^{-3}. The simulation box size is $12c/\omega_p \times 12c/\omega_p \times 4.3c/\omega_p$. $512 \times 512 \times 256$ grids and 4,194,304 particles for the beam and 4 particles/cell for the plasma are used in the simulation.

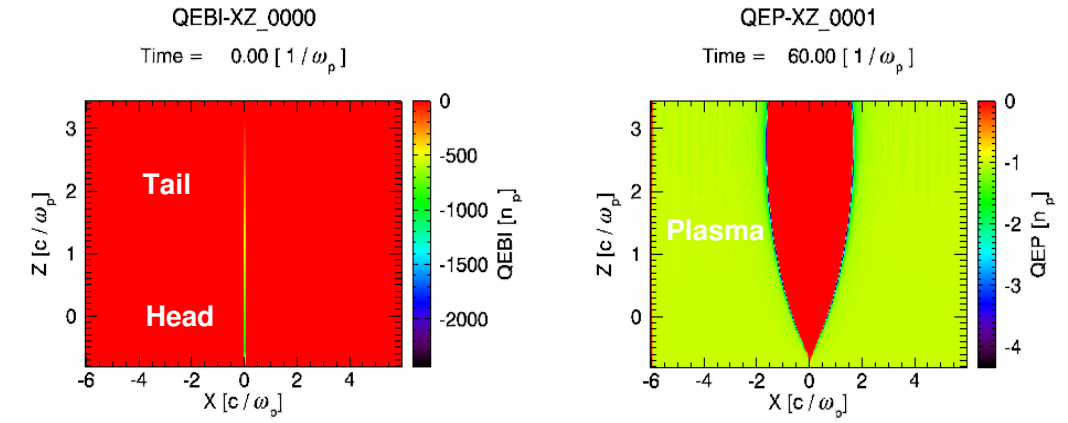

Figure 5.11: Density plot of the beams (left) and plasma (right) in the simulation for the hosing instability in the non-adiabatic relativistic blow-out regime.

The beam centroid oscillation at $3c/\omega_p$ in the beam is plotted in Fig. 5.12 as a red curve. The green dashed curve is the result from Whittum's theory and the blue dashed curve is from our new model. The new model also gives a reduced hosing growth for this case and the agreement with the simulation is satisfactory. The other two curves at the bottom of the plot are the results from the new model with only the c_3 correction, and with both the c_2 and c_3 corrections. The correction from c_3, i.e., the radius of the blow-out trajectory, has the largest contribution to the reduced hosing growth while the other two corrections also have smaller but still important contributions. The simulation result has a slightly lower hosing growth than the prediction from the new model. It might be due to the dropping of the terms proportional to $\dot{x}_c$ in the channel

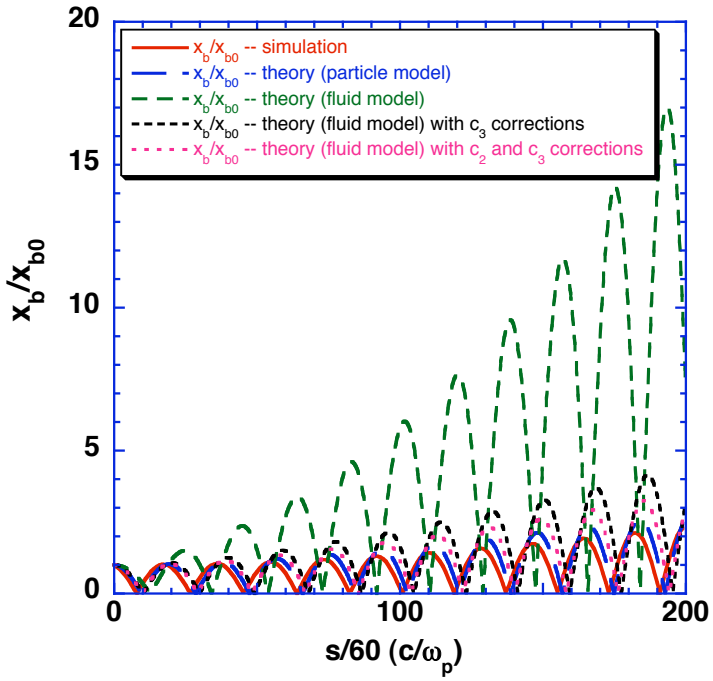

Figure 5.12: Hosing growth of the centroid oscillation as a function of propagation distance s from the simulation and the theory prediction for the non-adiabatic relativistic blow-out regime.

centroid equation, i.e., Eq. (5.27). We will investigate this discrepancy in the future.

5.3 Summary

The hosing instability is perhaps the biggest obstacle to making a high energy plasma wakefield acceleration stage. In this chapter, we studied the electron hosing instability using a particle model. An equation of motion describing the trajectory of a plasma electron in the moving window was derived. A linear perturbation theory is developed based on this equation. The new coupled centroid equation for the ion channel was cast into a form which can be easily compared to the result from previous fluid theory. The theory includes three numeric factors which reduce the coupling of centroid oscillation between the beam and the ion channel. These three factors represent the effects from the plasma self fields, the relativistic mass and the axial motion of plasma electrons, and the ξ-dependence of the channel radius respectively. Verification of the new particle model was carried out in four different blow-out regimes and the agreements between the model and the simulation results are found to be excellent.

CHAPTER 6

Simulation of Afterburner

The plasma afterburner has been proposed as a possible advanced accelerator scheme for a future linear collider. The concept which was introduced in section 1.5 uses a high energy electron(or positron) drive beam from an existing linac such as the SLC to drive a plasma wake. The wakefield which has a phase velocity equal to the velocity of the beam can be used to accelerate part of the drive beam or a trailing beam. Several issues such as the efficient transfer of energy and the stable propagation of the drive and trailing beams in the plasma are critical to the afterburner concept. In this chapter, we investigate the nonlinear beam-plasma interactions in such a scenario using QuickPIC.

6.1 Choosing parameters

In the non-linear blow-out regime of PWFA, the accelerating electric field can be roughly estimated by the 1D wave-breaking limit $E_{wave-breaking} \approx mc\omega_p/e \approx 96\sqrt{n_0}$ eV/m, where n_0 is in unit of cm^{-3}. Therefore larger accelerating fields can be achieved by using higher plasma density. However, due to technological limitations, the total number of beam particles generated in SLC or ILC is about 2×10^{10} and the longitudinal size is on the order of $10 \sim 100$ microns. These parameters put a limit on the maximum plasma density if one still wants to operate in the blow-out regime and one wants efficient beam-loading to be possible.

We use $n_0 \sim 10^{16} cm^{-3}$, which gives $c/\omega_p \sim 53\mu m$ and $E_{max} \sim 10$ GeV/m as a starting point.

In general, to efficiently transfer the energy from the drive beam to the wake and then to the trailing beam, the density profile of both beams are of importance. This is because the blow-out process is determined by the ratio Λ_b/Λ_0, where $\Lambda_b = n_b\sigma_r^2$ is the charge per unit length of the beam and $\Lambda_0 = n_p k_p^{-2}$ is the charges per unit length of the plasma in a cross section of $(c/\omega_p)^2$. When the beam radius is comparable to the blow-out radius, the blow-out trajectory also depends on the transverse profile of the beam. However, in the large blow-out radius situation, i.e., $r_{bm} >> r_0$, where r_{bm} is the maximum blow-out radius and r_0 is the transverse size of the beam, the dependence on the transverse profile is small, thus the longitudinal profile of the drive beam alone determines the rate of energy loss to the wake. The linear theory of beam loading [13] gives the ideal longitudinal "door-step" profile of the drive beam to achieve constant energy transfer rate to the wake inside the beam. In a future publication [37] we will show that even in the non-linear blow-out regime, a wedge shaped beam is best. In our simulations, the beam density rises linearly from the head to the tail. This profile gives a roughly constant deceleration wake field inside the beam except for the region near the head. The trailing beam is shorter and has less charge than the drive beam. It is placed near the end of the blow-out channel where it witnesses an acceleration field larger than the deceleration field acting on the drive beam. A trailing beam with a properly chosen profile can flatten the longitudinal field in the region where the beam resides, reducing the final energy spread of the trailing beam. We define the ratio between the beam-loaded acceleration field and the maximum deceleration field as the transformer ratio. It is desirable that this parameter is large so the energy transfer is most efficient.

The above discussion only serves as a general guideline, there is freedom in choosing the parameters for the final design. In reality, it is more difficult to manipulate the total charge, profile and separation of the beams than to fine-tune the plasma density to obtain a good wake field structure inside the ion channel.

Due to the development of QuickPIC, we are able to model both 100 GeV and 1 TeV afterburner stages. To put things in perspective, such simulations would have taken 500,000 and 5,000,000 node hours on the fastest supercomputers using full PIC codes such as OSIRIS. The parameters of our simulations are summarized in Table 6.1, and Table 6.2 lists the numerical parameters for the simulations. These simulations are not intended to be the final ones, but rather represent the first attempt to study the relevant physics of beam propagation in an "afterburner" stage.

Parameter	**100 GeV stage**	**1 TeV stage**
Initial energy (GeV)	50/50	500/500
Beam charges (10^{10})	3.0/1.0	3.0/1.0
Emittance ϵ_N ($mm \cdot mrad$)	2230/2230	2230/2230
Spot size σ_r (μm)	15/15	15/15
Driver length (μm)	145	145
Trailer σ_z (μm)	10	10
Beam separation (μm)	100	100
Plasma density (cm^{-3})	5.66×10^{16}	5.66×10^{16}
Plasma length (cm)	300	2819

Table 6.1: Simulation parameters

Parameter	**100 GeV stage**	**1 TeV stage**
Simulation box size (μm)	$280 \times 280 \times 380$	$760 \times 760 \times 380$
Number of grids	$256 \times 256 \times 256$	$512 \times 512 \times 256$
Number of beam particles	8,388,608/655,360	8,388,608/655,360
Number of plasma particles	4/cell	4/cell
3D time step ($1/\omega_p$)	90	300
Number of time steps	1520	4200

Table 6.2: Numerical simulation parameters

The 100 GeV stage starts with $\gamma_b = 97,847$ and a matched emittance, while the 1 TeV stage uses a beam of $\gamma_b = 978,473$ and ϵ_N about 1/3 of the matched emittance. So in the first simulation the beam envelope does not change, but the large emittance causes the beam head to erode rather quickly. In the second simulation, the erosion is minimal for the propagation distance which is on the order of $10^6 c/\omega_p$ or 28 meters.

6.2 Simulation results

Fig. 6.1 shows the evolution of the drive beam, the trailing beam and the plasma channel in the simulation for a 100 GeV afterburner stage. The wedge shape drive beam blows out an ion channel with a maximum radius of about $3c/\omega_p$. After the beam passes by and the electrons reach the maximum blow-out radius, they rush back towards the axis. The trailing beam is located about $4.5c/\omega_p$ behind the driver. In the blow-out regime, beam loading arises because the space charge of the trailing beam slows down the plasma electrons, as they return to the axis. The ion channel is elongated due to the existence of the second

beam. This also changes the position of the accelerating field spike and the E_z is flatten near the region where the second beam is located.

Since the drive beam's spot size and emittance are matched to the plasma density, the beam envelope remains about the same size in the simulation. However, because the matched beam propagation requires a fully formed ion channel, which is not the case for the head of the drive beam, the head erosion is clearly seen in Fig. 6.1. As the head of the beam diffracts, the ion channel shifts backwards, and hence does the wakefield structure. The decelerating field becomes larger and spikier compared with the initial wakefield, this is shown in Fig. 6.2,while the accelerating field becomes smaller. Both effects cause the transformer ratio to drop. Once the head of the beam is lost due to diffraction, the core of the beam which is overdense starts to interact with the plasma directly. The core of the beam has more charge to blow out a sufficiently deep channel for itself to keep focused. Therefore, the erosion of the beam and the wakefield evolution slow down leading to a relatively stable accelerating structure for the rest of the simulation. At the end of the simulation, the part of the drive beam located at where the decelerating field is largest is depleted, this effect causes the decelerating field to decrease and the ion channel to be formed behind the driver.

To see the effects of hosing, the drive beam also had an initial tilt in its centroid. The hosing instability was triggered by this initial tilt but it was stabilized in this matched beam simulation. The trailing beam was also seen to shift vertically in ion channel, but no significant hosing was found.

Fig. 6.3 shows the phase space of the drive beam and trailing beam during the simulation. The head of the drive beam expands and remains at the initial energy while the tail almost stops. The final energy of the trailing beam is centered around 100 GeV with 1.12 nC charge. About 0.48 nC of charge is lost

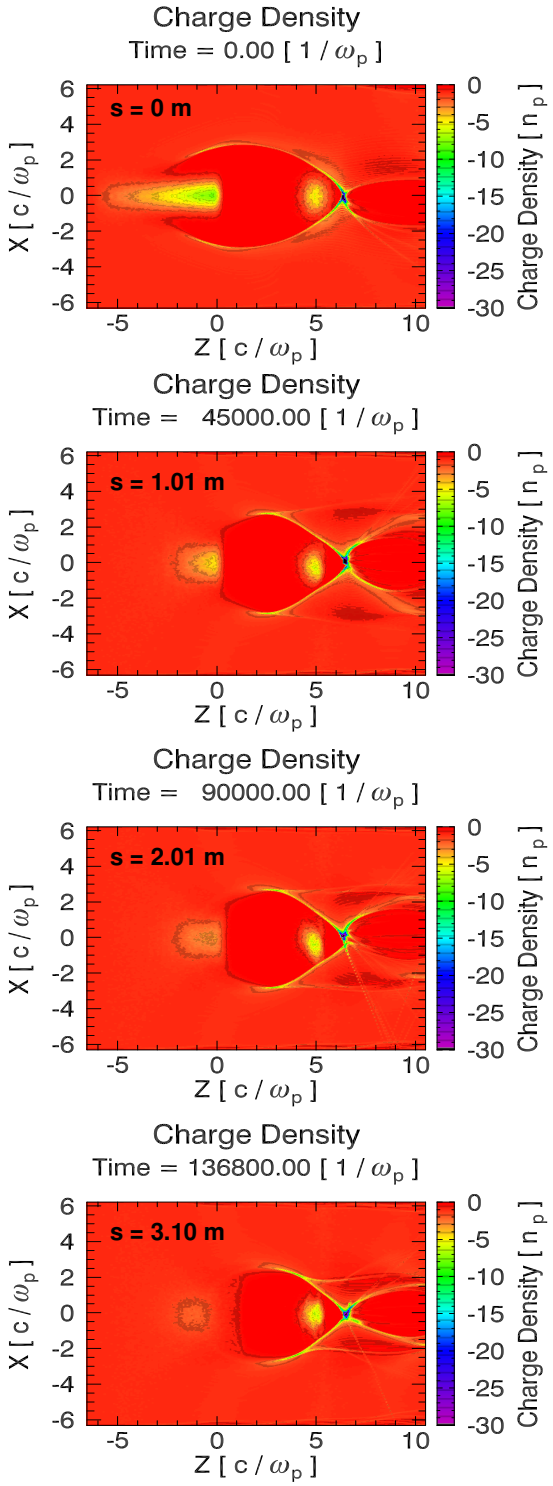

Figure 6.1: The beam and plasma evolution at different propagation distances from the 100GeV stage simulation. The beams move from right to left.

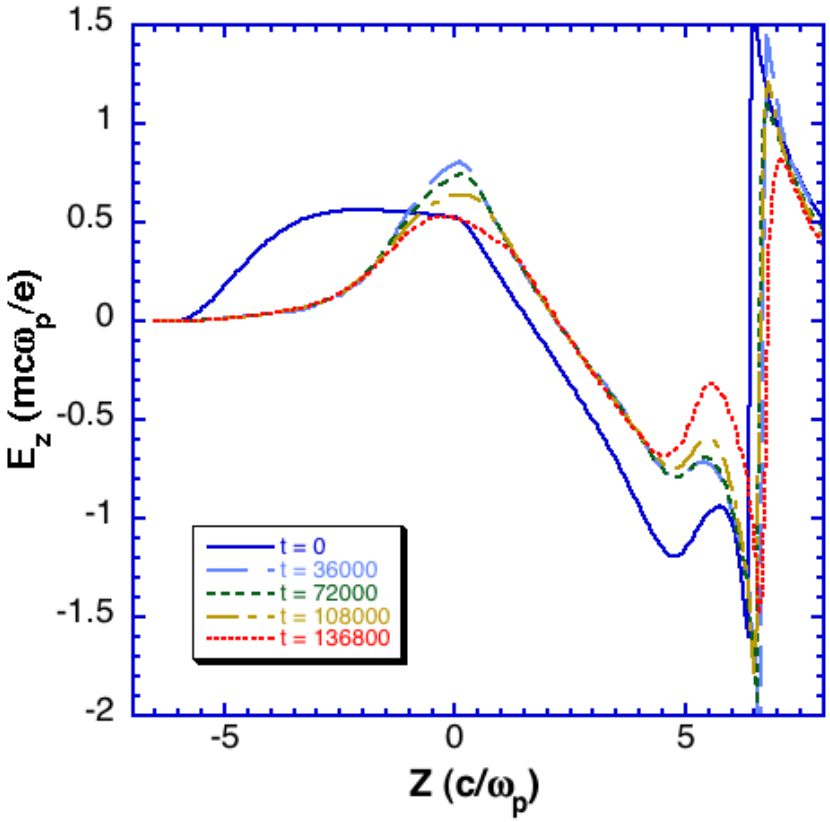

Figure 6.2: Longitudinal wakefield evolution in the 100 GeV simulation.

due to hosing, and the energy of these particle remains near 50 GeV. The energy distribution of the trailing beam is plotted in Fig. 6.4. The distribution of the accelerated particles has two peaks, one is near 92 GeV and the other one is near 102 GeV. The energy difference between these two peaks is about 10% of the mean energy, while each peak actually has an energy spread considerably less than 10%. The two peaks of the energy distribution can be explained by the non-uniform wakefield inside the trailing beam. As the drive beam and the wakefield evolve, the difference of the wakefield felt by the beam particles at differect ξ position first decreases then increases again as seen in Fig. 6.2. This causes the energy spread of the trailing beam. To improve the energy spread, it is desirable

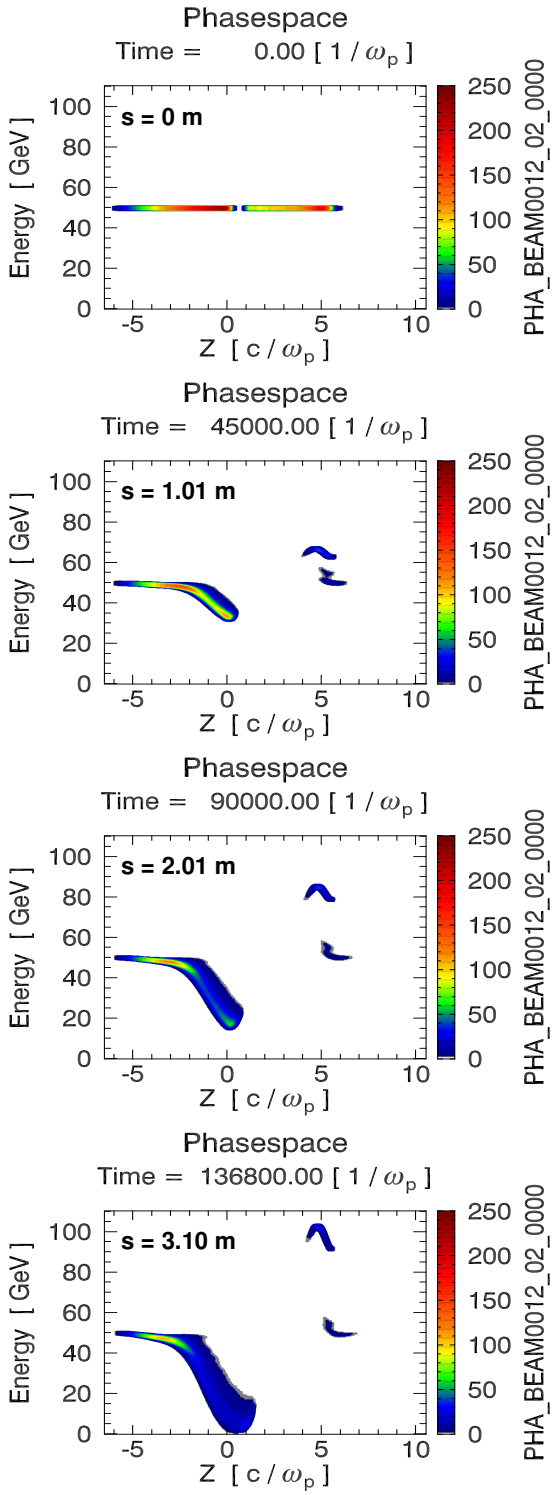

Figure 6.3: Phase space plot at the end of the 100 GeV stage simulation.

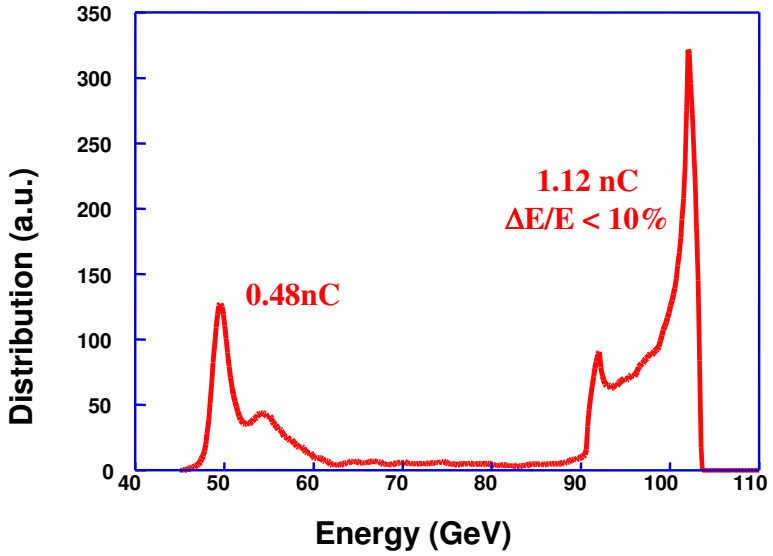

Figure 6.4: Energy distribution of the drive beam and the trailing beam in a 100 GeV afterburner simulation.

to have less head erosion. One way to achieve this is to use a smaller emittance as shown in the 1 TeV simulaiton below.

Results from the 1 TeV simulation are shown in Figs. 6.5-6.7. Fig. 6.6 is a sequence of the longitudinal wakefield plotted at different times of the simulation. In Fig. 6.7, the beams' energy versus longitudinal position is shown for this simulation. In this simulation, no initial tilt was used and little or no hosing growth was observed for either the driver or trailing beams. Therefore we focus on the characteristic of wakefield evolution and energy gain/lost during the propagation.

The TeV simulation had the same beam and plasma parameters as the 100 GeV simulation, except for the initial energy, emittance and propagation distance.

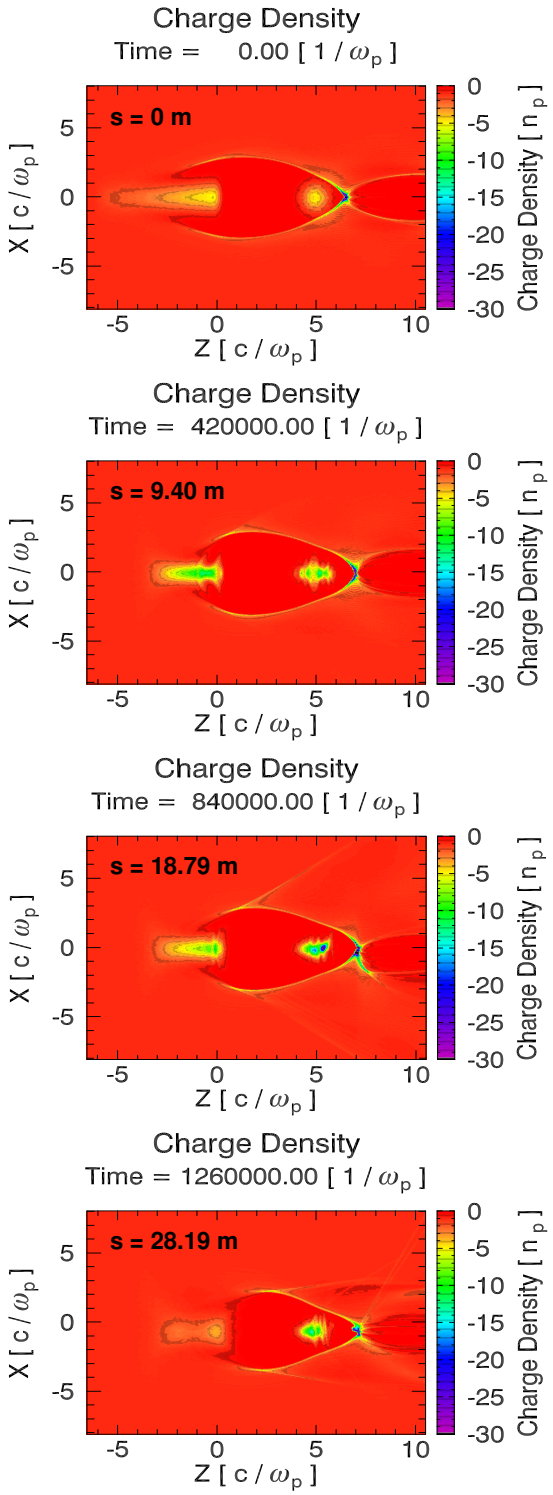

Figure 6.5: The beam and the plasma channel at different propagation distances in the 1 TeV simulation.

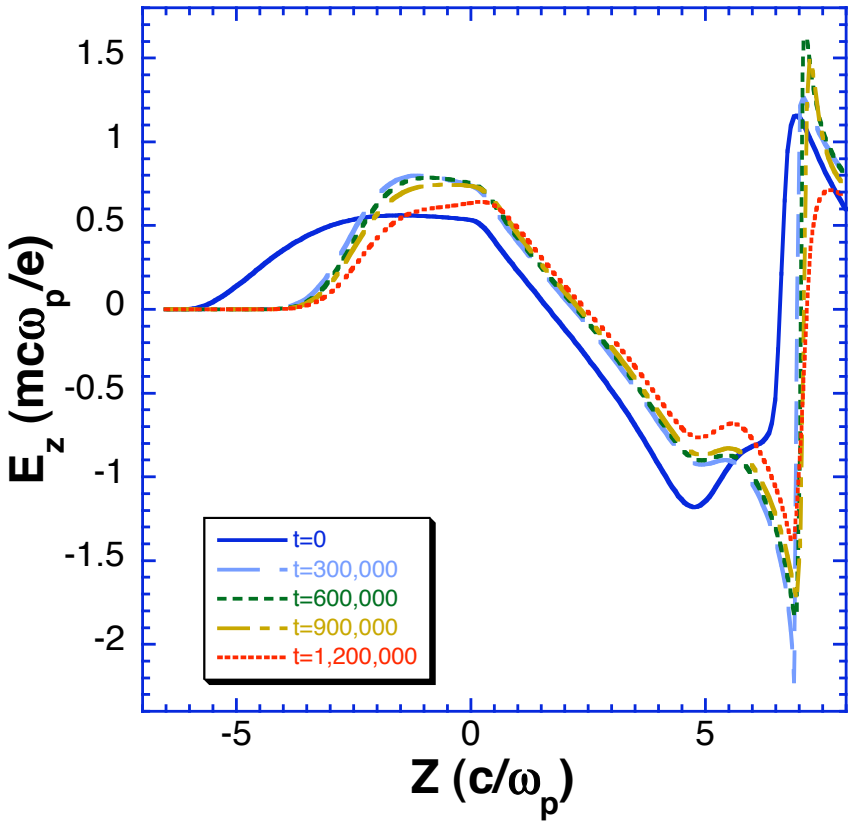

Figure 6.6: Longitudinal wakefield evolution in the 1 TeV stage simulation.

The beams have an emittance three times smaller than the matched emittance for this plasma density, therefore oscillations of the beam envelope are observed in the simulation, as seen in the second frame in Fig. 6.5. Because the beam particles have 10 times the energy than in the 100 GeV simulation, the head of the drive beam expands at a rate slower by 10 although the normalized emittance is the same. In this case only a small portion of the head of the beam erodes away at the beginning and the wake slips backwards as the beam head diverges. The decelerating field becomes larger while the acceleration field remains relatively unchanged. As before, the beam density at the new head position becomes high

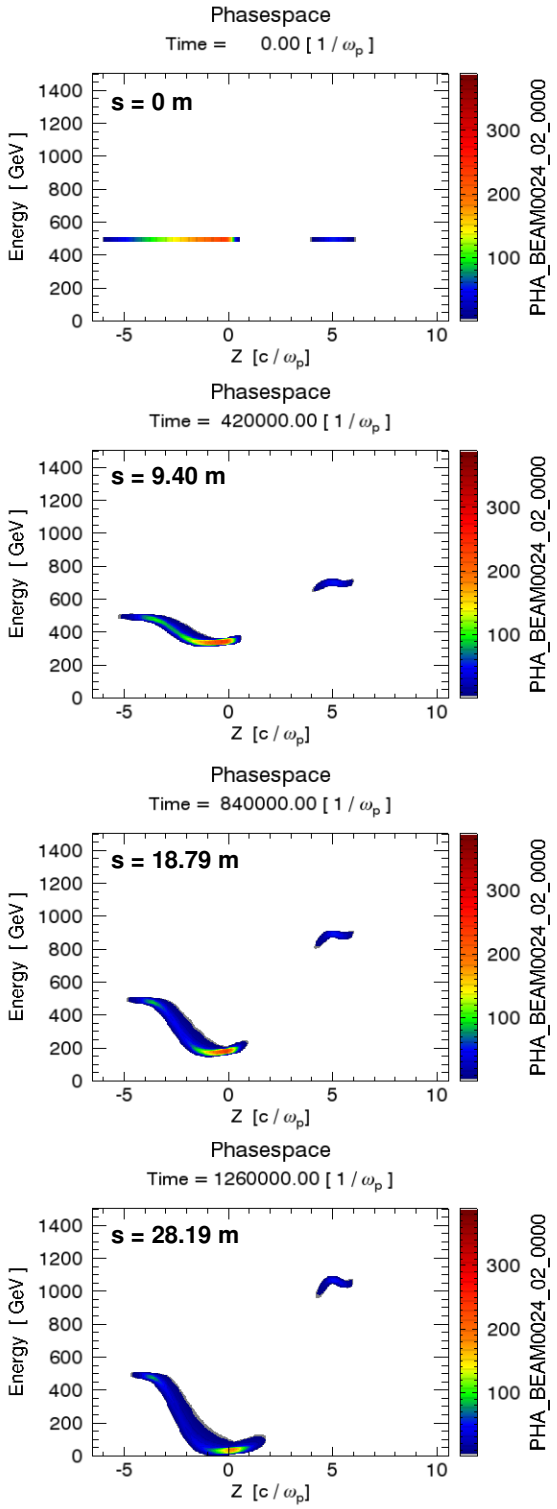

Figure 6.7: Phase space of the beams at different distances in the 1 TeV stage afterburner simulation.

enough to form the ion channel, and the erosion rate slows down. The wake is very stable for $\omega_p t > 90000$ and the transformer ratio remains close to 1.1. The drive beam evolution is also stable, and it drives a wake which has a more uniform decelerating field. The trailing beam sees an initial accelerating field which is not constant in the beam, but as the head erosion and wake slippage occurs, the accelerating field in the trailing beam becomes flat and an ideal beam-loading situation appears later in the simulation. This contributes to the smaller energy spread of the trailing beam compared with the 100 GeV simulation. The final energy of the trailing beam is about 1.08 TeV and the final FWHM energy spread is estimated to be about 5%.

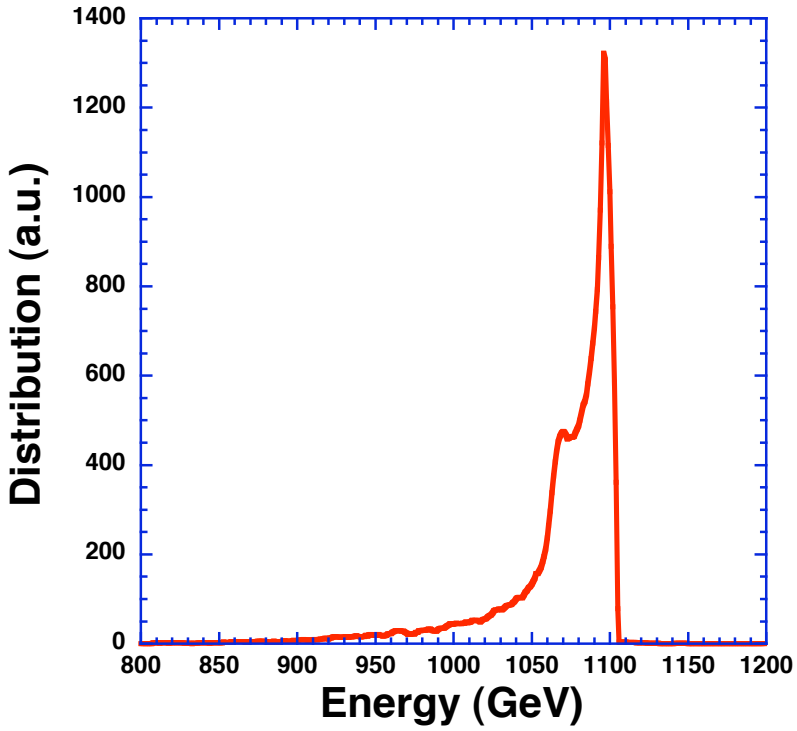

Figure 6.8: Energy distribution of the trailing beam in the 1TeV simulation.

6.3 Summary

In this chapter, two QuickPIC afterburner simulations were carried out. The first one is for a 100 GeV afterburner stage and the other one is for a 1 TeV stage. In both simulations, a drive beam with a linear ramp longitudinal density profile and a trailing beam with Gaussian profile are used. The emittances of the beams are chosen to be matched or nearly matched to the plasma density. The simulation for the 100 GeV stage was run with a initial tilt in the drive beam. The centroid oscillation triggered by the tilt was stabilized in the simulation. The evolutions of the beams and the wake were found to be stable except for the head erosion. The trailing beams in both simulations doubled their energy as desired.

These simulations are the first simulations for plasma afterburners. Currently, the simulations do not account for the radiation loss due to the particle betatron oscillations. The energy loss rate can be estimated by $W_{loss} = r_e mc^2 \gamma_b^2 k_p^4 \sigma_r^2/(12e)$ (eV/m). For the 100 GeV simulation parameters, the formula yields $W_{loss} = 1.06$ GeV/m. This is much smaller than $E_{wave-breaking} \approx 24$ GeV/m, therefore one can ignore the radiation loss. However, for a 1 TeV stage with the beam parameters in Table 6.1, $W_{loss} = 106.25$ GeV/m $>> E_{wave-breaking}$. One can reduce the loss to a few percent of $E_{wave-breaking}$ by compressing the transverse spot size by a factor of 10. A simulation for such a narrow beam is currently not feasible because it requires an enormous number of grid points. However, as long as the spot size is much smaller than the blow-out radius, the blow-out process should depend weakly on the spot size.

Another issue not being completely addressed in the 1 TeV simulation is the tolerance for the hosing instability. As we have discussed in Chapter 5, three effects on hosing need to be included for the non-adiabatic relativistic blow-out case in an afterburner stage. These effects arise from the charge neutralization

radius, the magnetic fields in the wake and plasma electrons' relativistic masses, and the plasma self force respectively. These three factors can be determined in the simulation and they generally reduce the growth rate from the linear fluid theory prediction. Further detail on the hosing instability in an afterburner stage, including the tolerance in the tilt and the mechanism to stabilize hosing will be conducted in the future.

Furthermore, these simulations are conducted using a pre-ionized plasma. It is advantageous to use a self-ionized plasma in a real experiment. In addition, ion motion could deteriorate the quality of the trailing beam and positron acceleration remains a problem to solve. As we continue to improve QuickPIC, all these problems can be addressed soon.

CHAPTER 7

Summary

Plasma-based acceleration can provide ultra-high acceleration gradients for future high energy physics research. The interaction between the driver and the plasma wakefield in this scenario is extremely nonlinear and complex. Therefore, to explore the underlying physics in this plasma accelerator concept, one often uses PIC computer simulation as a valuable tool. In this dissertation, we have described a novel PIC code, QuickPIC, for modeling the plasma wakefield accelerator. QuickPIC, which implements the quasi-static approximation, allows one to obtain accurate results with substantially less computation time than using full electromagnetic codes. Estimates indicate that it could lead to two orders of magnitude saving in computation time over existing simulation techniques without any loss in accuracy.

QuickPIC differs from previous quasi-static PIC models because it includes the full dynamic of the plasma response, and it is fully 3D and fully parallelized. This enables one to efficiently model the detailed physics in the current PWFA experiments and advanced concepts, such as afterburners. QuickPIC is constructed using two legacy simulation codes developed in UCLA, with modern programming interfaces in Fortran 90. This method of code development allows a rapid construction of a new code. An object-oriented framework structure has also greatly simplified the code development. QuickPIC is fully parallelized and scales well up to 32 processors for the typical problem sizes.

In this dissertation, we also used QuickPIC to conduct full scale 3D simulations of key physics for plasma wakefield accelerators. QuickPIC provides the opportunity to study 3D nonlinear and long time scale effects in PWFA which had been impossible or difficult to model using other codes. In particular, we investigated two physics phenomena.

The first one is the electron hosing instability. The existing fluid model for hosing analysis and its predictions were reviewed. QuickPIC simulations were conducted to study the hosing instability. It was found that the existing theory significantly overestimated the amount of hosing growth. For example, in the strongly non-linear blow-out regime, the simulation and theoretical growth rates differ by factors of 100 within only a small number of betatron oscillations. A kinetic model based on electrons' equations of motion was developed and three new terms were found. These terms arise from the perturbed fields from the plasma, the relativistic mass and axial motion of plasma electron and the ξ-dependent channel radius respectively. The new theory was validated with QuickPIC simulations.

The second phenomenon was the afterburner energy doubler concept for PWFA. A 100 GeV stage and a 1 TeV stage were simulated using QuickPIC. It was found that beam loaded transformer ratios larger than 1 are possible for 3 to 1 ratio between the number of electrons in the drive beam and the trailing beam. In these full scale simulations, the drive beam and the trailing beam were found to be stable during the propagation and the final energy of the trailing beam was indeed doubled as desired. The energy spreads of the trailing beam was about 5% for the 1 TeV stage.

In this dissertation we only touched the tip of the ice berg in regard to both the development of QuickPIC and its use. We have been constantly improv-

ing QuickPIC for both versatility and performance. There are many interesting problems related to the afterburner concept that need to be explored, such as the betatron radiation from the beam in a TeV class afterburner, the ion response to an intense beam, the use of a hollow plasma channel to guide and accelerate a positron beam and the use of a thin plasma lens for the final focusing of the beam. To model these problems with QuickPIC, new capabilities in the code are required. These will be done in a modular approach. These additions have been planned as the next step to integrate more physics into our quasi-static model. There is also a demand to couple the result from other simulation codes, such as the initial beam data from the particle tracking code Litrack, or a self injected beam generated at the end of a full electromagnetic LWFA simulation. Such works will enable an end-to-end simulation for plasma-based accelerators.

Another aspect of the future work is to improve the performance of QuickPIC. Load-balancing is currently being added in QuickPIC to address the parallel efficiency. A software pipe-lining technique was also proposed to decompose a large simulation into several steps which can be pipe-lined and assigned to different groups of processors. This will increase the level of parallelization and allow QuickPIC to scale to thousands of processors easily.

APPENDIX A

Conserved Quantity of Particle Motion

In this appendix we will derive Eq. (2.58), i.e., a conserved quantity of plasma electron's motion,

$$\frac{d}{dt}\left[\gamma_e - \tilde{p}_z - (1-\tilde{q}_e\tilde{\psi})\right] = 0 \tag{A.1}$$

where $\tilde{p}_z = p_z/mc = \gamma\beta_z$, $\tilde{q}_e = q_e/e$ and $\tilde{\psi} = \psi e/(mc^2)$ are the normalized parallel momentum, normalized charge and normalized "pinch potential" respectively. The dimensionless velocity becomes $\beta = \mathbf{v}/c$.

We start from the momentum equation,

$$\frac{d\tilde{p}_z}{dt} = \frac{\tilde{q}_e e}{mc}\left[-\frac{\partial\phi}{\partial z} - \frac{\partial A_z}{c\partial t} + \beta_x \times (\frac{\partial A_x}{\partial z} - \frac{\partial A_z}{\partial x}) + \beta_y \times (\frac{\partial A_y}{\partial z} - \frac{\partial A_z}{\partial y})\right] \tag{A.2}$$

and energy equation,

$$\frac{d\gamma}{dt} = \frac{q_e}{mc^2}\mathbf{v}\cdot\mathbf{E} = \frac{\tilde{q}_e e}{mc}\left[-\beta\cdot\nabla\phi - \beta\cdot\frac{\partial\mathbf{A}}{c\partial t}\right] \tag{A.3}$$

Subtracting Eq. (A.2) from Eq. (A.3), we get,

$$\frac{d(\gamma-\tilde{p}_z)}{dt} = \frac{\tilde{q}_e e}{mc}\left[-(\frac{\partial}{c\partial t} + \beta\cdot\nabla)(\phi - A_z) + (\frac{\partial}{c\partial t} + \frac{\partial}{\partial z})(\phi - \beta\cdot\mathbf{A})\right] \tag{A.4}$$

The first term on the right hand side can be rewritten as

$$-\frac{\tilde{q}_e e}{mc}(\frac{\partial}{c\partial t}+\beta\cdot\nabla)(\phi-A_z)=-\frac{d}{dt}(\tilde{q}_e\tilde{\psi}) \tag{A.5}$$

The second term can be rewritten in terms of the $\xi = ct - z$ and $s = z$ coordinates as

$$\frac{\tilde{q}_e e}{mc}(\frac{\partial}{c\partial t}+\frac{\partial}{\partial z})(\phi-\beta\cdot\mathbf{A})=\frac{\tilde{q}_e e}{mc}\frac{\partial}{\partial s}(\phi-\beta\cdot\mathbf{A}) \tag{A.6}$$

Therefore,

$$\frac{d(\gamma-\tilde{p}_z+\tilde{q}_e\tilde{\psi})}{dt}=\frac{\tilde{q}_e e}{mc}\frac{\partial}{\partial s}(\phi-\beta\cdot\mathbf{A}) \tag{A.7}$$

and in the spirit of the quasi-static approximation $\partial/\partial s \approx 0$, this becomes,

$$\frac{d(\gamma-\tilde{p}_z+\tilde{q}_e\tilde{\psi})}{dt}=0 \tag{A.8}$$

If we assume that the plasma is at rest in front of the beam then,

$$\gamma-\tilde{p}_z+\tilde{q}_e\tilde{\psi}=(\gamma-\tilde{p}_z+\tilde{q}_e\tilde{\psi})|_{t=-\infty}=1. \tag{A.9}$$

From Eq. (A.9) one can obtain a relationship between $\tilde{p}_z$ and $\tilde{p}_\perp$. In particular, squaring both sides of the relationship

$$\gamma=1+\tilde{p}_z-\tilde{q}_e\tilde{\psi}. \tag{A.10}$$

leads to

$$\tilde{p}_z=\frac{1+\tilde{p}_\perp^2-(1-\tilde{q}_e\tilde{\psi})^2}{2(1-\tilde{q}_e\tilde{\psi})}. \tag{A.11}$$

Therefore, $\tilde{p}_z$ can be calculated without using the $\hat{z}$ component of the equation of motion. Eq. (A.11) is used in our full quasi-static QuickPIC algorithm.

APPENDIX B

An Analytical Model For ψ

In Chapter 5, we derived the new coupled centroid equation Eq. (5.28) for the hosing instability. Eq. (5.28) contains a numeric factor $c_2 = \frac{1}{1+\psi_0}$, where $\psi_0 \equiv \psi(r_0(\xi))$. The value of ψ_0 was taken from the simulation for the four simulations described in Chapter 5. Here, we introduce an analytical model from Ref. [37] for ψ_0.

Since $-\nabla_\perp^2 \psi = 4\pi(\rho - J_z/c)$ (Eq. (2.63)), one needs to determined the source term $(\rho - J_z/c)$ in order to calculate ψ. It is found that ψ depends weakly on the exact radial profile of $(\rho - J_z/c)$. A simplified profile is used in [37] which is also shown in Fig. 1.4. The $(\rho - J_z/c)$ profile in the plasma sheath and the linear response region is assumed to be constant. The value of the constant is $(\rho - J_z/c) = n_\Delta = \frac{r_0^2}{(r_0+\Delta)^2 - r_0^2}$ with Δ being the width of the constant profile. And $(\rho - J_z/c) = -1$ for $r < r_0$. Therefore, the solution for ψ is

$$\psi(r) = \frac{r_0^2(\xi)}{4}(1 + \beta(\xi)) - \frac{r^2}{4} for r < r_0, \tag{B.1}$$

where $\beta(\xi) = \frac{(1+\alpha)^2 ln(1+\alpha)^2}{(1+\alpha)^2 - 1} - 1$ and $\alpha \equiv \frac{\Delta}{r_0}$.

One can also derive an equation of motion for $r_0(\xi)$ by assuming $\frac{\partial \Delta}{\partial \xi} \approx 0$. It is written as,

$$A(r_0)\frac{d^2 r_0}{d\xi^2} + B(r_0) r_0 (\frac{dr_0}{d\xi})^2 + C(r_0) r_0 = \frac{\lambda(\xi)}{r_0}, \tag{B.2}$$

where $A(r_0) = 1 + [\frac{1}{4} + \frac{\beta}{2} + \frac{1}{8} r_0 \frac{d\beta}{dr_0}] r_0^2$, $B(r_0) = \frac{1}{2} + \frac{3}{4}\beta + \frac{3}{4} r_0 \frac{d\beta}{dr_0} + \frac{1}{8} r_0^2 \frac{d^2\beta}{dr_0^2}$, $C(r_0) = \frac{1}{4}[1 + 1/(1 + \frac{\beta}{4} r_0^2)^2]$ and $\lambda(\xi) = \int_0^{r>>\sigma_r} r n_b dr$.

For given beam parameters, the unperturbed blow-out trajectory r_0 can be solved from Eq. (B.2), and ψ can be determined from Eq. (B.1) once r_0 is obtained.

References

[1] ILC official website. http://www.interactions.org/linearcollider/.

[2] R.-D. Heuer (Univ. Hamburg). The electron-positron linear collider - probing the secrets of the universe. Colloquium at Brookhaven National Lab., May 25 2003.

[3] Wikipedia. Higgs boson. http://en.wikipedia.org/wiki/Higgs_boson.

[4] International Technology Recommendation Panel. Final international technology recommendation panel report. Technical report, International Linear Collider Steering Committee, 2004.

[5] T. Tajima and J.M. Dawson. Laser electron accelerator. *Physical Review Letters*, 43(4):267–270, 1979.

[6] C. Joshi, W. B. Mori, T. Katsouleas, J. M. Dawson, J. M. Kindel, and D. W. Forslund. Ultra-high gradient particle acceleration by intense laser-driven plasma density waves. *Nature*, 311:525, 1984.

[7] C. Joshi, T. Tajima, J. M. Dawson, H. A. Baldis, and N. A. Ebrahim. Forward raman instability and electron acceleration. *Physical Review Letters*, 47:1285–1288, 1981.

[8] T. M. Antonsen and P. Mora. Self-focusing and raman scattering of laser pulses in tenuous plasmas. *Physical Review Letters*, 69:2204–2207, 1992.

[9] J. Krall, A. Ting, E. Esarey, and P. Sprangle. Enhanced acceleration in a self-modulated-laser wake-field accelerator. *Physical Review E*, 48:2157–2161, 1993.

[10] N. E. Andreev, L. M. Gorbunov, V. I. Kirsanov, A. Pogosova, and R. R. Ramazashvili. The theory of laser self-resonant wake field accelerator. *Physica Scripta*, 49:101–109, 1994.

[11] P. Chen, J. M. Dawson, R. W. Hu, and T. Katsouleas. Acceleration on electrons by the interaction of a bunched electron beam with a plasma. *Physical Review Letters*, 54:693, 1985.

[12] T. Katsouleas. Physical mechanisms in the plasma wake-field accelerator. *Physical Review A*, 33:2056, 1986.

[13] T. Katsouleas, S. Wilks, P. Chen, J. M. Dawson, and J. J. Su. Beam loading in plasma accelerators. *Part. Accel.*, 22:81, 1987.

[14] W. Lu, C. Huang, M.M. Zhou, W.B. Mori, and T. Katsouleas. Limits of linear plasma wakefield theory for electron or positron wake. *Physics of Plasma*, 12:063101, 2005.

[15] C. Joshi. Review of beam driven plasma wakefield accelerators. In *ADVANCED ACCELERATOR CONCEPTS: Eleventh Advanced Accelerator Concepts Workshop*, volume 737, pages 3–10. AIP, 2004.

[16] M.J. Hogan, C.D. Barnes, C. E. Clayton, F.J. Decker, S. Deng, P. Emma, C. Huang, R. H. Iverson, D. K. Johnson, C. Joshi, T. Katsouleas, P. Krejcik, W. Lu, K. A. Marsh, W. B. Mori, P. Muggli, C. O'Connell, E. Oz, R.H. Siemann, and D. Walz. Multi-GeV energy gain in a plasma wakefield accelerator. *Physical Review Letters*, 95:054802, 2005.

[17] J. B. Rosenzweig. Nonlinear plasma dynamics in the plasma wakefield accelerator. *Phys. Rev. Lett.*, 58:555–558, 1987.

[18] J. B. Rosenzweig, B. Breizman, T. Katsouleas, and J. J.Su. Acceleration and focusing of electrons in two-dimensional nonlinear plasma wakefields. *Physical Review A*, 44:6189–6192, 1991.

[19] W. K. H. Panofsky and W. A. Wenzel. Some considerations concerning the transverse deflection of charged particles in radio-frequency fields. *Review of Scientific Instruments*, 27:967, 1956.

[20] J.Krall, G.Joyce, and E.Esarey. Vlasov simulations of very large amplitude wave generation in the plasma wakefield accelerator. *Phys. Rev. A*, 44:6854–6861, 1991.

[21] N. Barov and J. B. Rosenzweig. Propagation of short electron pulses in underdense plasmas. *Phys. Rev. E*, 49:4407–4416, 1994.

[22] J. Krall and G. Joyce. Transverse equilibrium and stability of the primary beam in the plasma wake-field accelerator. *Physics of Plasmas*, 2(4):1326–1331, 1995.

[23] S. Lee, T. Katsouleas, R. Hemker, and W. B. Mori. Simulations of a meter-long plasma wakefield accelerator. *Phys. Rev. E*, 61:7014–7021, 2000.

[24] E. S. Dodd, R. G. Hemker, C.-K. Huang, S. Wang, C. Ren, W. B. Mori, S. Lee, and T. Katsouleas. Hosing and sloshing of short-pulse GeV-class wakefield drivers. *Physical Review Letters*, 88(12):125001, 2002.

[25] R. G. Hemker, W. B. Mori, S. Lee, and T. Katsouleas. Dynamic effects in plasma wakefield excitation. *Phys. Rev. ST Accel. Beams*, 3:061301, 2000.

[26] David L. Bruhwiler, Rodolfo E. Giacone, John R. Cary, John P. Verboncoeur, Peter Mardahl, Eric Esarey, W. P. Leemans, and B. A. Shadwick. Particle-In-Cell simulations of plasma accelerators and electron-neutral collisions. *Phys. Rev. ST Accel. Beams*, 4:101302, 2001.

[27] K. V. Lotov. Fine wakefield structure in the blowout regime of plasma wakefield accelerators. *Physical Review Special Topics-Accelerators and Beams*, 6(6):061301, 2003.

[28] C. Joshi, B. Blue, C. E. Clayton, E. Dodd, C. Huang, K. A. Marsh, W. B. Mori, S. Wang, M. J. Hogan, C. O'Connell, R. Siemann, D. Watz, P. Muggli, T. Katsouleas, and S. Lee. High energy density plasma science with an ultrarelativistic electron beam. *Physics of Plasmas*, 9(5):1845–1855, 2002.

[29] David H. Whittum, Andrew M. Sessler, and John M. Dawson. Ion-channel laser. *Phys. Rev. Lett.*, 64:2511, 1990.

[30] K. V. Lotov. Plasma response to ultrarelativistic beam propagation. *Physics of Plasmas*, 3(7):2753–2759, 1996.

[31] David H. Whittum. Nonlinear, relativistic return current sheath for an ion-focused beam. *Physics of Fluids B: Plasma Physics*, 4(2):476–478, 1992.

[32] K. V. Lotov. Blowout regimes of plasma wakefield acceleration. *Phys. Rev. E*, 69:046405, 2004.

[33] A. Pukhov and J. Meyer ter Vehn. Laser wake field acceleration: the highly non-linear broken-wave regime. *Applied Physics B: Lasers and Optics*, 74(4-5):355–361, 2002.

[34] I. Kostyukov, A. Pukhov, and S. Kiselev. Phenomenological theory of laser-plasma interaction in "bubble" regime. *Physics of Plasmas*, 11(11):5256–5264, 2004.

[35] N. Barov, J. B. Rosenzweig, M. C. Thompson, and R. B. Yoder. Energy loss of a high-charge bunched electron beam in plasma: Analysis. *Phys. Rev. ST Accel. Beams*, 7:061301, 2004.

[36] J. B. Rosenzweig, N. Barov, M. C. Thompson, and R. B. Yoder. Energy loss of a high charge bunched electron beam in plasma: Simulations, scaling, and accelerating wakefields. *Phys. Rev. ST Accel. Beams*, 7:061302, 2004.

[37] W. Lu, C. Huang, M.M. Zhou, W.B. Mori, and T. Katsouleas. A nonlinear kinetic theory for multi-dimensional plasma wave wakefields. submitted to Phys. Rev. Lett.

[38] M. J. Hogan, R. Assmann, F.-J. Decker, R. Iverson, P. Raimondi, S. Rokni, R. H. Siemann, D. Walz, D. Whittum, B. Blue, C. E. Clayton, E. Dodd, R. Hemker, C. Joshi, K. A. Marsh, W. B. Mori, S. Wang, T. Katsouleas, S. Lee, P. Muggli, P. Catravas, S. Chattopadhyay, E. Esarey, and W. P. Leemans. E-157: A 1.4-m-long plasma wake field acceleration experiment using a 30 GeV electron beam from the Stanford Linear Accelerator Center Linac. *Physics of Plasmas*, 7(5):2241–2248, 2000.

[39] M. J. Hogan, C. E. Clayton, C. Huang, P. Muggli, S. Wang, B. E. Blue, D. Walz, K. A. Marsh, C. L. O'Connell, S. Lee, R. Iverson, F.-J. Decker, P. Raimondi, W. B. Mori, T. C. Katsouleas, C. Joshi, and R. H. Siemann. Ultrarelativistic-positron-beam transport through meter-scale plasmas. *Physical Review Letters*, 90(20):205002, 2003.

[40] S. Lee, T. Katsouleas, P. Muggli, W. B. Mori, C. Joshi, R. Hemker, E. S. Dodd, C. E. Clayton, K. A. Marsh, B. Blue, S. Wang, R. Assmann, F. J. Decker, M. Hogan, R. Iverson, and D. Walz. Energy doubler for a linear collider. *Physical Review Special Topics - Accelerators and Beams*, 5:011001, 2002.

[41] S. Lee, T. Katsouleas, R. G. Hemker, E. S. Dodd, and W. B. Mori. Plasma-wakefield acceleration of a positron beam. *Physical Review E (Statistical, Nonlinear, and Soft Matter Physics)*, 64(4):045501, 2001.

[42] H. Lee Buchanan. Electron beam propagation in the ion-focused regime. *Physics of Fluids*, 30(1):221–231, 1987.

[43] David H. Whittum, William M. Sharp, Simon S. Yu, Martin Lampe, and Glenn Joyce. Electron-hose instability in the ion-focused regime. *Physical Review Letters*, 67(8):991–994, 1991.

[44] Andrew A. Geraci and David H. Whittum. Transverse dynamics of a relativistic electron beam in an underdense plasma channel. *Physics of Plasmas*, 7(8):3431–3440, 2000.

[45] J. B. Rosenzweig, D. B. Cline, B. Cole, H. Figueroa, W. Gai, R. Konecny, J. Norem, P. Schoessow, and J. Simpson. Experimental observation of plasma wake-field acceleration. *Physical Review Letters*, 61(1):98–101, 1988.

[46] J. B. Rosenzweig, P. Schoessow, B. Cole, W. Gai, R. Konecny, J. Norem, and J. Simpson. Experimental measurement of nonlinear plasma wake fields. *Physical Review A (General Physics)*, 39(3):1586–1589, 1989.

[47] J. B. Rosenzweig, P. Schoessow, B. Cole, C. Ho, W. Gai, R. Konecny, S. Mtingwa, J. Norem, M. Rosing, and J. Simpson. Demonstration of electron beam self-focusing in plasma wake fields. *Physics of Fluids B: Plasma Physics*, 2(6):1376–1383, 1990.

[48] K. Nakajima, A. Enomoto, H. Kobayashi, H. Nakanishi, Y. Nishida, A. Ogata, S. Ohasawa, T. Oogoe, T. Shoji, and T. Urano. Plasma wake-field accelerator experiments at KEK. *Nucl. Instrum. Methods A*, 292:12, 1990.

[49] Atsushi Ogata. Plasma lens and wake experiments in japan. In *Advanced accelerator concepts*, volume 279, pages 420–449. AIP, 1992.

[50] A. K.Berezin, Ya. B.Fainberg, V. A.Kiselev, A. F.Linnik, V. V.Uskov, V. A.Balakirev, I. N.Onishchendo, G. L.Sidelnikov, and G. V.Sotnikov. Wake field excitation in plasma by a relativistic electron pulse with a controlled number of short bunches. *Fizika Plazmy*, 20:663–670, 1994.

[51] N. Barov, J. B. Rosenzweig, M. E. Conde, W. Gai, and J. G. Power. Observation of plasma wakefield acceleration in the underdense regime. *Physical Review Special Topics-Accelerators and Beams*, 3(1):011301, 2000.

[52] B. E. Blue, C. E. Clayton, C. L. O'Connell, F.-J. Decker, M. J. Hogan, C. Huang, R. Iverson, C. Joshi, T. C. Katsouleas, W. Lu, K. A. Marsh, W. B. Mori, P. Muggli, R. Siemann, and D. Walz. Plasma-wakefield acceleration of an intense positron beam. *Physical Review Letters*, 90(21):214801, 2003.

[53] J. D. Lawson. *The Physics of Charged Particle Beams*. Oxford University Press, London, 2nd edition, 1988.

[54] J. D. Jackson. *Classical Electrodynamics*. Wiley, New York, 1975.

[55] C. Joshi, T. Katsouleas, J. Dawson, Y. Yan, and J. Slater. Plasma wave wigglers for free-electron lasers. *IEEE Journal of Quantum Electronics*, 23:1571–1577, 1987.

[56] Shuoqin Wang, C. E. Clayton, B. E. Blue, E. S. Dodd, K. A. Marsh, W. B. Mori, C. Joshi, S. Lee, P. Muggli, T. Katsouleas, F. J. Decker, M. J. Hogan, R. H. Iverson, P. Raimondi, D. Walz, R. Siemann, and R. Assmann. X-Ray emission from betatron motion in a plasma wiggler. *Physical Review Letters*, 88(13):135004, 2002.

[57] C. K. Birdsall and A. B. Langdon. *Plasma Physics via Computer Simulation*. McGraw-Hill, New York, 1985.

[58] J. P. Verboncoeur, A. B. Langdon, and N. T. Gladd. An object-oriented electromagnetic PIC code. *Computer Physics Communications*, 87:199–211, 1995.

[59] R. Hemker. *Particle-In-Cell Modeling of Plasma-Based Accelerators in Two and Three Dimensionss*. PhD thesis, University of California, Los Angeles, 2000.

[60] A. Pukhov. Three-dimensional electromagnetic relativistic particle-in-cell code VLPL (virtual laser plasma lab). *J. Plasma Physics*, 61:425–433, 1999.

[61] C. Nieter and J. R. Cary. VORPAL: a versatile plasma simulation code. *J. Comp. Phys.*, 196:448–472, 2004.

[62] D.E. Gordon, W.B. Mori, and T.M. Antonsen Jr. A ponderomotive guiding center particle-in-cell code for efficient modeling of laser-plasma interactions. *IEEE Transactions on Plasma Science*, 28:1224–1232, 2000.

[63] Patrick Mora, Thomas M. Antonsen, and Jr. Kinetic modeling of intense, short laser pulses propagating in tenuous plasmas. *Physics of Plasmas*, 4(1):217–229, 1997.

[64] David H. Whittum. Transverse two-stream instability of a beam with a Bennett profile. *Physics of Plasmas*, 4(4):1154–1159, 1997.

[65] John M. Dawson. Particle simulation of plasmas. *Reviews of Modern Physics*, 55(2):403–447, 1983.

[66] W. B. Mori. Recent advances and some results in plasma-based accelerator modeling. In *ADVANCED ACCELERATOR CONCEPTS: Tenth Workshop*, volume 647, pages 11–28. AIP, 2002.

[67] C.G. Darwin. *Phil. Mag.*, 39:537, 1920.

[68] C. W. Nielson and H. R. Lewis. Particle-code methods in the nonradiative limit. *Methods in Comput. Phys.*, 16:367, 1976.

[69] D. W. Hewett. Low-frequency electromagnetic (Darwin) applications in plasma simulation. *Computer Physics Communications*, 84:243–277, 1994.

[70] Eric Sonnendrucker, John J. Ambrosiano, and Scott T. Brandon. A finite element formulation of the Darwin PIC model for use on unstructured grids. *Journal of Computational Physics*, 121:281–297, 1995.

[71] J. Busnardo-Neto, P. L. Pritchett, A. T. Lin, and J. M. Dawson. A self-consistent magnetostatic particle code for numerical simulation of plasmas. *Journal of Computational Physics*, 23:300–312, 1977.

[72] A. Z. Ghalam, T. Katsouleas, S. Lee, W. B. Mori, C. Huang, V. Decyk, and C. Ren. Simulation of electron-cloud instability in circular accelerators using plasma models. In *Proceedings of Advanced Accelerator Concepts: Tenth Workshop*, volume 647, pages 224–231. AIP, 2002.

[73] C. Huang, V. Decyk, S. Wang, E. Dodd, C. Ren, W. Mori, T. Katsouleas, J. Cooley, and T. M. Antonsen Jr. A parallel Particle-In-Cell code for efficiently modeling plasma wakefield acceleration: QuickPIC. In *Proceedings, 18th Annual Review of Progress in Computational Electromagnetics*, page 557, 2002.

[74] D. W. Hewett and C. W. Nielson. A multidimensional quasineutral plasma simulation model. *Journal of Computational Physics*, 29:219–236, 1978.

[75] W.W.L. Lee, E. Startsev, Hong Qin, and R.C. Davidson. Electromagnetic (Darwin) model for three-dimensional perturbative particle simulation of high intensity beams. In *Proceedings of the 2001 Particle Accelerator Conference, 2001.*, volume 3, pages 1906–1908, 2001.

[76] R.A. Fonseca, L.O. Silva, F.S. Tsung, V.K. Decyk, W. Lu, C. Ren, W.B. Mori, S. Deng, S. Lee, T. Katsouleas, and J.C. Adam. OSIRIS: A three-dimensional, fully relativistic particle in cell code for modeling plasma based accelerators. *Lecture Notes in Computer Science*, 2331:342, 2002.

[77] J. P. Boris. Relativistic plasma simulation-optimization of a hybrid code. In *Proc. 4th Conf. Numer. Simul. Plasmas*, 1970.

[78] John von Neumann. Various techniques used in connection with random digits. In *John von Neumann, Collected Works*, volume V. Oxford, 1963.

[79] W.B. Mori. The physics of the nonlinear optics of plasmas at relativistic intensities for short-pulse lasers. *IEEE Journal of Quantum Electronics*, 33:1942–1953, Nov 1997.

[80] R. W. Boyd. *Nonlinear Optics*. Academic Press, Boston, 1992.

[81] R. D. Richtmeyer and K. W. Morton. Difference methods for initial-value problems. In L. Bers, R. Courant, and J. J. Stoker, editors, *Interscience Tracts in Pure and Applied Mathematics*, volume 4. Wiley, New York, 1967.

[82] V. K. Decyk and C. D. Norton. UCLA parallel PIC framework. *Computer Physics Communications*, 164:80–85, December 2004.

[83] Paulett C. Liewer and Viktor K. Decyk. A general concurrent algorithm for plasma particle-in-cell simulation codes. *Journal of Computational Physics*, 85:302–322, December 1989.

[84] Suzhi Deng, Tom Katsouleas, Xiaodong Wang, and Warren Mori. Developing a multi-timescale PIC code for plasma accelerators. In *Proceedings of the 2005 Particle Accelerator Conference*, 2005. in press.

[85] M.M. Zhou. Development and applications of the ionization package in QuickPIC - a novel Quasi-Static PIC code for PWFA study. Master's thesis, University of California, Los Angeles, 2005. in preparation.

[86] John R. Cary and Courtlandt L. Bohn. Computational accelerator physics working group summary. In *ADVANCED ACCELERATOR CONCEPTS: Eleventh Advanced Accelerator Concepts Workshop*, volume 737, pages 231–242. AIP, 2004.

[87] D. H. Whittum. *Theory of the Ion-Channel Laser*. PhD thesis, University of California, Berkeley, 1990.